FEDERAL UNIVERSITY OF MINAS GERAIS
School of Engineering
Graduate Program in Structural Engineering

Pâmela Daniela Nogueira Reges

MICROMORPHIC CONTINUUM AND ENRICHED-FEM FOR PRESSURIZED FRACTURES

Belo Horizonte
2025

Pâmela Daniela Nogueira Reges

MICROMORPHIC CONTINUUM AND ENRICHED-FEM FOR PRESSURIZED FRACTURES

Thesis submitted to the Graduate Program in Structural Engineering of the School of Engineering at the Federal University of Minas Gerais, in partial fulfillment of the requirements for the degree of "Doctor in Structural Engineering".

Supervisor: Prof. Dr. Roque Luiz da Silva Pitangueira

Co-Supervisor: Prof. Dr. Leandro Lopes da Silva

Belo Horizonte
2025

Reges, Pâmela Daniela Nogueira.
R333m
Micromorphic continuum and enriched-fem for pressurized fractures [recurso eletrônico] / Pâmela Daniela Nogueira Reges. - 2025.
1 recurso online (127 f. : il., color.) : pdf.

Orientador: Roque Luiz da Silva Pitangueira.
Coorientador: Leandro Lopes da Silva.

Tese (doutorado) Universidade Federal de Minas Gerais, Escola de Engenharia.

Apêndices: f. 123-127.

Bibliografia: f.108-122.

1. Engenharia de estruturas - Teses. 2. Mecânica da fratura - Teses. 3. Mecânica computacional - Teses. 4. Mecânica de dano contínuo - Teses. 5. Método dos elementos finitos - Teses. 6. Deformações (Mecânica) - Teses. I. Pitangueira, Roque Luiz da Silva. II. Silva, Leandro Lopes da. III. Universidade Federal de Minas Gerais. Escola de Engenharia. IV. Título.

CDU: 624(043)

Ficha catalográfica elaborada pelo bibliotecário Reginaldo César Vital dos Santos CRB/6 2165
Biblioteca Prof. Mário Werneck, Escola de Engenharia da UFMG

UNIVERSIDADE FEDERAL DE MINAS GERAIS

PROPEEs PROGRAMA DE PÓS-GRADUAÇÃO EM ENGENHARIA DE ESTRUTURAS UFMG

ATA DA DEFESA DE TESE DE DOUTORADO EM ENGENHARIA DE ESTRUTURAS Nº 109 DA ALUNA PAMELA DANIELA NOGUEIRA REGES

Às **15:00** horas do dia **28** de **março** de 2025, reuniu-se em ambiente virtual, na Escola de Engenharia da Universidade Federal de Minas Gerais - UFMG, a Comissão Examinadora indicada pelo Colegiado do Programa em 27 de fevereiro de 2025 para julgar a defesa da Tese de Doutorado intitulada: **"Micromorphic Continuum and Enriched-FEM for Pressurized Fractures"**, cuja aprovação é um dos requisitos para a obtenção do Grau de DOUTOR EM ENGENHARIA DE ESTRUTURAS na área de ESTRUTURAS.

Abrindo a Sessão, o Presidente da Comissão, Prof. Dr. Roque Luiz da Silva Pitangueira, após dar conhecimento aos presentes do teor das Normas Regulamentares, passou a palavra a aluna para apresentação de seu trabalho. Finalizada a apresentação, seguiu-se para a fase de arguição pelos examinadores, com as respectivas respostas da aluna. Logo após a fase de arguição, a Comissão se reuniu, sem a presença da aluna e do público, para julgamento e expedição do resultado final, a saber:

(X) Aprovado

(   ) Reprovado

O resultado final foi comunicado publicamente à aluna pelo Presidente da Comissão.

Nada mais havendo a tratar, a Presidente encerrou a reunião e lavrou a presente ata, que será assinada por todos os membros participantes da Comissão Examinadora e pela aluna.

Comissão Examinadora:

Prof. Dr. Roque Luiz da Silva Pitangueira - UFMG (Orientador)

Prof. Dr. Leandro Lopes da Silva - UFMG (Coorientador)

Prof. Dr. Lapo Gori - UFMG

Prof. Dr. Felício Bruzzi Barros - UFMG

Prof. Dr. Rodrigo Peluci de Figueiredo - UFOP

Prof. Dr. Eduardo Nobre Lages - UFAL

Profa. Dra. Flavia de Souza Bastos - UFJF

A aprovação da aluna na Defesa de Tese de Doutorado não significa que a mesma tenha cumprido todos os requisitos necessários para obtenção do DIPLOMA de Doutor em Engenharia de Estruturas.

Para ciência da aluna:

1. Atesto que as alterações solicitadas pela Comissão Examinadora serão cumpridas no prazo de ATÉ 60 dias corridos.
2. Atesto estar ciente que a versão corrigida da Tese deverá ser entregue ao Repositório Institucional da UFMG, conforme orientações disponíveis em: https://repositorio.ufmg.br/custom/instructions.jsp

Ciente: Pamela Daniela Nogueira Reges

Aluna

Belo Horizonte, 28 de março de 2025.

Após a Homologação da Defesa pelo Colegiado do Programa, este documento será assinado pela Coordenação e disponibilizado ao aluno.

Documento assinado eletronicamente por **Roque Luiz da Silva Pitangueira**, **Professor do Magistério Superior**, em 28/03/2025, às 20:20, conforme horário oficial de Brasília, com fundamento no art. 5º do Decreto nº 10.543, de 13 de novembro de 2020.

Documento assinado eletronicamente por **Leandro Lopes da Silva**, **Professor do Magistério Superior**, em 28/03/2025, às 20:21, conforme horário oficial de Brasília, com fundamento no art. 5º do Decreto nº 10.543, de 13 de novembro de 2020.

Documento assinado eletronicamente por **Eduardo Nobre Lages**, **Usuário Externo**, em 28/03/2025, às 20:21, conforme horário oficial de Brasília, com fundamento no art. 5º do Decreto nº 10.543, de 13 de novembro de 2020.

Documento assinado eletronicamente por **Felicio Bruzzi Barros**, **Professor do Magistério Superior**, em 28/03/2025, às 20:21, conforme horário oficial de Brasília, com fundamento no art. 5º do Decreto nº 10.543, de 13 de novembro de 2020.

Documento assinado eletronicamente por **Rodrigo Peluci de Figueiredo**, **Usuário Externo**, em 28/03/2025, às 20:22, conforme horário oficial de Brasília, com fundamento no art. 5º do Decreto nº 10.543, de 13 de novembro de 2020.

Documento assinado eletronicamente por **Flávia de Souza Bastos**, **Usuário Externo**, em 28/03/2025, às 21:28, conforme horário oficial de Brasília, com fundamento no art. 5º do Decreto nº 10.543, de 13 de novembro de 2020.

Documento assinado eletronicamente por **Lapo Gori**, **Professor do Magistério Superior**, em 28/03/2025, às 22:26, conforme horário oficial de Brasília, com fundamento no art. 5º do Decreto nº 10.543, de 13 de novembro de 2020.

Documento assinado eletronicamente por **Pâmela Daniela Nogueira**, **Usuário Externo**, em 31/03/2025, às 08:10, conforme horário oficial de Brasília, com fundamento no art. 5º do Decreto nº 10.543, de 13 de novembro de 2020.

A autenticidade deste documento pode ser conferida no site https://sei.ufmg.br/sei/controlador_externo.php?acao=documento_conferir&id_orgao_acesso_externo=0, informando o código verificador **4068471** e o código CRC **9977A598**.

To my husband and friend, Jônatas.

Acknowledgments

A realização desta tese não teria sido possível sem o apoio e o incetivo de diversas pessoas, de forma direta ou indireta, às quais expresso minha gratidão.

Antes, agradeço a Deus, criador dos céus e da terra. Nele encontro a razão única e final da minha existência.

Em seguida, agradeço ao meu querido esposo Jônatas. Seu amor, paciência e alegria me levaram mais longe do que eu iria se estivesse sozinha e tornaram meu dias mais leves.

Ao meu orientador, professor Roque, agradeço pela sua orientação e incentivo ao longo de todo o desenvolvimento do trabalho. Sua dedicação e sua humanidade são louváveis e me ensinaram muito mais do que aquilo que consta nestas páginas.

Agradeço também ao meu coorientador, professor Leandro. Sua disposição e seu conhecimento se refletem neste trabalho, o aperfeiçoando de forma primoroza.

À minha família, que, com carinho incondicional e completa compreensão, me deu um fundamento sólido a partir do qual pude enfrentar os desafios da jornada.

Aos colegas, amigos e professores da UFMG e do grupo INSANE, agradeço pelas discussões, trocas de experiência e todas as contribuições no desenvolvimento deste trabalho. A jornada com amigos é mais fácil e o espírito colaborativo do nosso grupo de pesquisa contribuiu imensamente para a minha formação. Agradeço de forma especial à amiga Eduarda que, sempre com muita prontidão, me ajudou nas simulações aqui apresentadas.

Também agradeço às agências de fomento CAPES, CNPq e FAPEMIG pelo suporte financeiro que possibilitou a realização deste estudo.

Muito obrigada!

Although to penetrate into the intimate mysteries of nature and thence to learn the true causes of phenomena is not allowed to us, nevertheless it can happen that a certain fictive hypothesis may suffice for explaining many phenomena.
Leonhard Euler

I believe in Christianity as I believe that the sun has risen: not only because I see it, but because by it I see everything else.
C.S. Lewis

Resumo

O estudo de materiais complexos tem evoluído com o desenvolvimento das teorias de contínuos generalizados, que oferecem vantagens em relação à teoria clássica ao incorporar parâmetros adicionais em sua formulação, permitindo assim uma melhor descrição dos efeitos na microescala. Dentre essas abordagens, o contínuo micromórfico tem se mostrado uma teoria promissora, considerando seu alto nível de generalização, no qual cada partícula do meio é dotada de um campo de deformação completo. Esta pesquisa investiga o uso da teoria micromórfica para a modelagem de dano e fratura dentro de um framework contínuo-discreto, com foco especial na aplicação a fraturas pressurizadas. Um aspecto-chave deste estudo é a avaliação de um critério de localização dentro do meio micromórfico, que é conhecido por suas propriedades de regularização quando ocorre a localização de deformações. Esse critério é então aplicado para determinar a transição entre dano contínuo e descontínuo. Além disso, o estudo explora a descrição da propagação de trincas utilizando o método dos elementos finitos estendido (XFEM), adaptado ao contínuo generalizado utilizado, incorporando a capacidade de modelar descontinuidades sem necessidade de mudanças na malha. A pesquisa também expande essa abordagem XFEM micromórfica para a modelagem de fraturas pressurizadas, permitindo uma representação satisfatória do crescimento de trincas induzidas por fluido. Os resultados deste estudo contribuem para o desenvolvimento dos modelos de contínuos generalizados, reforçando a relevância dessas abordagens na mecânica computacional. Os resultados aqui apresentados demonstram a eficácia da metodologia proposta, fornecendo uma base para avanços futuros na modelagem de fraturas e na mecânica do dano.
Palavras-chave: contínuo micromórfico; localização de deformações; tensor acústico; método dos elementos finitos estendido; trinca pressurizada.

Abstract

The study of complex materials has evolved with the development of generalized continuum theories, which offer advantages over the classical theory by incorporating additional parameters in their formulation being thus able to better capture microscale effects. Among these approaches, the micromorphic continuum has proven to be a promising framework considering its high level of generalization in which each material particle is endowed with a full deformation field. This research investigates the use of a micromorphic theory for modeling damage and fracture within a continuous-discontinuous framework, with a special focus on pressurized fractures applications. A key aspect of this study is the evaluation of a localization criterion within a micromorphic media, which is know for its regularization properties when strain localization occurs. This criterion is then applied for determining the transition from continuous to discontinuous damage. Furthermore, the study explores the description of crack propagation using an extended finite element method (XFEM) adapted to the generalized continuum used, incorporating the ability to model discontinuities without remeshing. The research also extends this micromorphic enriched-FEM approach to the modeling of pressurized fractures enabling a satisfactory representation of fluid-driven crack growth. The finding of this study contribute to the ongoing development of generalized continuum models, reinforcing the relevance of these approaches in computational mechanics. The results here presented demonstrate the effectiveness of the proposed methodology, providing a foundation for further advancements in fracture modeling and damage mechanics.

Key-words: micromorphic media; strain localization; acoustic tensor; extended finite element method; pressurized fracture.

List of figures

List of tables

List of abbreviations and acronyms

BEM	boundary element method
BVP	boundary value problem
CMD	crack mouth displacement
COD	crack opening displacement
DEM	discrete element method
E-FEM	embedded finite element method
FDEM	finite-discrete element method
FDM	finite difference method
FE^2	finite element squared method
FEM	finite element method
FPZ	fracture process zone
G-FEM	generalized finite element method
INSANE	INteractive Structural ANalysis Environment
LEFM	linear elastic fracture mechanics
PFM	phase-field model
RVE	representative volume element
RBSN	Rigid-Body-Spring Network
XFEM	extended finite element method

List of symbols

Chapter 2: Modeling of damage and fracture

$\mathcal{G}$	energy release rate
K	stress intensity factor
l_{LPZ}	fracture process zone length
P	material point
$u(x)$	displacement field (classical continuum)
ε_{ij}	strain tensor (classical continuum)

Chapter 3: Micromorphic Media

A_{klmn}	constitutive tensor (micromorphic theory)
B_{klmn}	constitutive tensor (micromorphic theory)
B_0	continuous body in the material configuration
B_t	continuous body in the spatial configuration
C_{ijkl}	compliance tensor (classical continuum)
C_{klmnpq}	constitutive tensor (micromorphic theory)
$\mathscr{D}$	damage variable
E	Young's modulus (classical continuum)
E_{ijkl}	stiffness tensor (classical continuum)
E^t_{ijkl}	tangential stiffness tensor (classical continuum)
E_{klmn}	constitutive tensor (micromorphic theory)
F	loading function
F_{klmnp}	constitutive tensor (micromorphic theory)
G_{klmnp}	constitutive tensor (micromorphic theory)
Γ_{eq}	generalized equivalent strain
Γ_{KLM}	wryness tensor
$\Gamma_{\delta\psi}$	generalized strain operator
δS_D	area of the defects
$\dot{\lambda}$	inelastic multiplier
$K(D)$	history variable
$\mathcal{C}_{KL}$	microdeformation tensor

$\mathfrak{C}_{KL}$	deformation tensor
$\boldsymbol{H}$	Hardening-Softening modulus (stress-based formulation)
l_{LPZ}	fracture process zone length
M^A_{lmknpq}	directions of degradation (C^S_{lmknpq})
M^a_{klmn}	directions of degradation (A^S_{klmn})
M^b_{klmn}	directions of degradation (B^S_{klmn})
M^c_{klmn}	directions of degradation (E^S_{klmn})
n	unit vector normal to a plane
P	material particle
p^a_q, p^b_q, p^A_q	internal variables
$\mathcal{G}$	energy release rate
ψ^0	internal energy
$\Sigma_{\beta\nu}$	generalized stress operator
t_{kl}	stress tensor
s_{kl}	micro-stress average
m_{klm}	stress moments tensor
$\mathfrak{m}^a_{kl}$	directions of degradation (stress tensor)
$\mathfrak{m}^b_{kl}$	directions of degradation (micro-stress average tensor)
$\mathfrak{m}^A_{klm}$	directions of degradation (stress moments tensor)
ε_{ij}	strain tensor (classical continuum)
ϵ_{kl}	linear strain tensor (micromorphic theory)
e_{kl}	linear strain tensor (micromorphic theory)
γ_{klm}	linear strain tensor (micromorphic theory)
σ_{ij}	stress tensor (classical continuum)
ϕ_{kl}	micromotion gradient tensor
K	stress intensity factor
$\boldsymbol{\chi}$	microdeformation tensor
$\boldsymbol{R}$	microrotation tensor
$\boldsymbol{U}$	right stretch tensor
$\boldsymbol{V}$	left stretch tensor
$\boldsymbol{\Xi}$	position vector for the microcontinuum in the material configuration
$\boldsymbol{\xi}$	position vector for the microcontinuum in the spatial configuration
$\mathfrak{X}$	inverse microdeformation gradient tensor
$\mathcal{E}_{\beta\nu\delta\psi}$	generalized constitutive relation
u_l	displacement vector
$u(x)$	displacement field (classical continuum)

Chapter 4: Discontinuous failure in micromorphic elastic-degrading media

a_i, b_i	vectorial amplitude of the jump
A_{ij}	second-order tensorial amplitude of the jump
α	maximum damage (exponential damage law)
β	damage evolution intensity (exponential damage law)
E	Young's modulus
j	scalar measure of microinertia
K_0	threshold for the equivalent strain
$\mathcal{Q}$	generalized acoustic tensor
Q_{kl}	acoustic tensor (classical continuum)
Q^{a}_{lm}	macroscale initial acoustic tensors ($\boldsymbol{A}^0$)
Q^{A}_{lmnp}	macroscale initial acoustic tensors ($\boldsymbol{C}^0$)
Q^{b}_{lm}	initial microscale acoustic tensor
$Q^{t,aa}_{lp}, Q^{t,aA}_{pql}, Q^{t,AA}_{lmpq}, Q^{t_A a}_{plm}$	tangent acoustic tensors
$Q^{t,b}_{lp}$	microscale tangent acoustic tensor
$Q^{S,aa}_{lp}, Q^{S,AA}$	secant acoustic tensors
$Q^{S,b}_{lp}$	microscale secant acoustic tensor
ρ	mass density in the reference configuration
$S(t)$	singular surface
ν	Poisson's ratio
$\boldsymbol{n}$	unit vector normal
$\boldsymbol{v}$	speed of propagation

Chapter 5: Micromorphic enriched-FEM model

H	Heaviside function
K_0, K_f	threshold values for the equivalent strain (linear damage law)
Π	total potential energy of the body
U	strain energy
V	potential energy of the applied loads
$\mathcal{V}$	considered domain
$\partial\mathcal{V}_d$	discontinuity
$\boldsymbol{B}_{\boldsymbol{u}}$	strain approximation matrices (macromotion)
$\boldsymbol{B}_{\phi}$	strain approximation matrices (micromotion)
$\boldsymbol{d}_{\boldsymbol{u}}$	regular micromorphic nodal degrees of freedom (macroscale)
$\boldsymbol{d}'_{\boldsymbol{u}}$	enhanced nodal degrees of freedom (macroscale)
$\boldsymbol{d}_{\phi}$	regular micromorphic nodal degrees of freedom (microscale)
$\boldsymbol{d}'_{\phi}$	enhanced nodal degrees of freedom (microscale)
$\boldsymbol{f}_{eq,\boldsymbol{u}}$	equivalent nodal force vector (macromotion)
$\boldsymbol{f}_{eq,\boldsymbol{u}'}$	equivalent nodal force vector (enhanced macromotion)
$\boldsymbol{f}_{eq,\phi}$	equivalent nodal force vector (micromotion)

$\boldsymbol{f}_{eq,\phi'}$	equivalent nodal force vector (enhanced micromotion)
$\boldsymbol{K_{uu}}$	stiffness submatrix
$\boldsymbol{K_{u\phi}}$	stiffness submatrix
$\boldsymbol{K_{uu'}}$	stiffness submatrix
$\boldsymbol{K_{u\phi'}}$	stiffness submatrix
$\boldsymbol{K_{\phi\phi}}$	stiffness submatrix
$\boldsymbol{K_{\phi u'}}$	stiffness submatrix
$\boldsymbol{K_{\phi\phi'}}$	stiffness submatrix
$\boldsymbol{K_{u'u'}}$	stiffness submatrix
$\boldsymbol{K_{u'\phi'}}$	stiffness submatrix
$\boldsymbol{K_{\phi'\phi'}}$	stiffness submatrix
$\boldsymbol{L_u}$	differential operators (macromotion)
$\boldsymbol{L_\phi}$	differential operators (micromotion)
$\boldsymbol{M}$	rearrangement matrix
$\boldsymbol{N}$	standard finite element shape function (macromotion)
$\bar{\boldsymbol{N}}$	standard finite element shape function (micromotion)
$\bar{\boldsymbol{N}}_{\boldsymbol{S}}$	matrix of the interpolation functions of the micromotion ”symmetric”
$\bar{\boldsymbol{N}}_{\boldsymbol{T}}$	matrix of the interpolation functions of the micromotion ”transposed”

Chapter 6: Pressurized fracture

$\mathcal{V}$	considered domain
$\partial\mathcal{V}_d$	discontinuity
$\boldsymbol{f}_{eq,\boldsymbol{u}'}$	external forces term related to the macro additional displacements
$\boldsymbol{p}$	fluid pressure
$\boldsymbol{w}$	crack opening

Table of contents

Chapter 1

Introduction

1.1 Motivations

The study of damage and fracture mechanics in structures has long been a critical topic in computational mechanics. As a result, there is a growing demand for reliable models capable of accurately representing the complex phenomena involved in material failure. In general, deformation and failure occur across multiple scales. At the macroscopic level, structural rupture is initiated by localized failure, which corresponds to the loss of material continuity in a specific region. However, this localized failure is preceded by microcrack coalescence at smaller scales, significantly influencing the overall fracture process. Understanding and accurately modeling these multiscale failure mechanisms is essential for predicting structural behavior.

Two important modeling approaches emerge from these considerations. The first is the continuous-discontinuous approach to damage and fracture. In this framework, initial microcracking is represented using a continuous model, while the transition to full crack formation is modeled by introducing a strong discontinuity once a critical threshold is reached. This approach requires a well-defined criterion to determine the transition from smeared cracking to a discrete crack. In the literature, the concept of strain localization and instability is well explored to couple continuous-discontinuous strategies, particularly through the singularity of the acoustic tensor.

On the other hand, classical continuum theories, which treat each material point as a mathematical point, are not well-suited for capturing microscale effects that influence macroscopic failure behavior. In this context, generalized continuum theories provide a robust alternative for modeling damage and fracture. Among these, the micromorphic continuum extends classical mechanics by incorporating additional degrees of freedom associated with the deformation of the material microstructure. The micromorphic framework thus enables a more comprehensive description of material behavior, making it particularly useful for heterogeneous media and multiscale problems. Additionally, its nonlocal formulation mitigates numerical challenges related to strain localization and softening behavior—issues that often arise in classical continuum theories.

Therefore, a continuous-discontinuous model based on the micromorphic theory represents a promising approach for modeling damage and fracture in materials with microstructure. This model could also be valuable for simulating pressurized fractures when considering the hydraulic fracture process that large-scale structures undergo. Hydraulic fracturing is a widely applied technique in the field of geomechanics and reservoir engineering, playing an important role in the extraction of oil and gas from subsurface formations and also in the project of concrete dams and reservoirs subjected to water loads. It involves the creation and propagation of fractures due to fluid pressure.

Considering that elastic-degrading damage models for micromorphic media have already been proposed, two important questions emerge when proposing a continuous-discontinuous damage model for micromorphic media. First, the definition of a criteria for introducing a discontinuity needs to be studied in the context of a generalized theory considering that the analysis of the acoustic tensor relies on the strain localization phenomenon and the micromorphic continuum is already know for its regularization properties when dealing with strain localization. Second, the numerical approach used to introduce the discontinuity in the problem also require studies as, in a standard finite element approach, refined meshes and remeshing are necessary and it could be proven particularly computational costly when considering that the micromorphic media is already endowed with additional degrees of freedom. The extended finite element model (XFEM) presents a compelling alternative for modeling crack propagation without the need for remeshing. However, its application within a micromorphic framework remains unexplored. Investigating this integration could offer a novel approach to modeling fracture processes in micromorphic materials.

Despite its advantages, the micromorphic continuum remains an underexplored field, particularly within the Brazilian research community. Few research groups have developed models based on generalized continua and the continuity of this line of research is essential for further expanding knowledge in the field and strengthening its applications in engineering problems. Applications could also emerge from the perspective of multiscale models considering the naturally multiscale approach of the micromorphic theory. Such an approach would enable a more comprehensive investigation of fracture processes, bridging different length scales and capturing interactions between microstructural damage mechanisms and macroscopic material behavior.

1.2 Objectives

1.2.1 General objective

Taking into account the premises discussed in the previous Section 1.1, the main objective of this research was to develop and evaluate a micromorphic framework for modeling damage and fracture within a continuous-discontinuous approach, with a particular focus on pressurized fractures. This includes the formulation and implementation of a robust localization criterion, the description of crack propagation using the Extended Finite Element Method (XFEM), and the application of this framework to pressurized fracture simulations.

1.2.2 Specific objectives

To ensure the accomplishment of the general objective previously set, three broad specific objectives were defined:

1. Study a localization criterion for the micromorphic continuum based on the concepts of localization analysis and adopting a numerical approach based on a Cartesian parametrization (Fioresi et al., 2020), evaluating its effectiveness in detecting strain localization and guiding fracture evolution;
2. Develop an approach to describe a discontinuity in a micromorphic medium using XFEM and implementing it into the INSANE system, considering a elastic-degrading models (Reges et al., 2023) for continuous damage and adopting an appropriate localization criterion as a threshold for crack propagation, i.e., discontinuous damage;
3. Model pressurized fractures under constant load in a micromorphic medium building on the enriched-FEM approach and the localization criterion developed, further expanding the model in the INSANE system.

The three objectives of this work involved computational implementations and numerical simulations which were all developed within the open-source software INSANE (INteractive Structural ANalysis Environment, `http://www.insane.dees.ufmg.br`), which source code is freely available at the Git repository `https://git.insane.dees.ufmg.br/insane/insane.git`. This work builds upon previous implementations available in the system, being of particular importance the computational framework for micromorphic media (Silva et al., 2022, Reges et al., 2023, 2024) and the well established XFEM approach for classical continuum (Alves et al., 2013, Silva et al., 2016).

1.3 Outline

This thesis is organized in 7 chapters and one appendix. Following this introduction (Chapter 1), Chapter 2 presents a survey on the literature concerning aspects of the modeling of damage and fracture. It contain aspects of the different approaches to damage modeling, considering discontinuous, continuous and continuous-discontinuous models. Chapter 3 presents the theoretical foundation of micromorphic media. It gives an overview of generalized continua, the specific aspects of the micromorphic theory and the elastic-degrading framework adopted in modeling continuous damage. Chapter 4 deals with the study of discontinuous failure in micromorphic media. It presents the formulation of the micromorphic acoustic tensor following a macroscale approach and a microscale approach, and numerical investigations of the behavior of both strategies. Following, Chapter 5 presents the micromorphic enriched-FEM formulation as well as numerical examples adopting the formulated framework. Chapter 6 focus on the problem of pressurized fractures, presenting an overview of the literature in the field and, more specifically, its formulation in the micromorphic-XFEM framework.

It is worth mentioning that Chapters 4 to 6 cover more specifically the three specific objectives described in Section 1.2.2. They follow the same pattern in which the theoretical foundation is first detailed and the proposed examples are then presented. This structure was adopted to clearly state the main contributions of this work that build one upon another as the chapters progresses.

Finally, Chapter 7 conclude this thesis, summing up the its main contributions and discussing possible future developments in the research field. The text is followed by one appendix (A) which details the FEM approach quantities used in Chapter 5.

Chapter 2

Modeling of damage and fracture

This chapter provides a brief literature review on damage and fracture modeling. It explores different approaches, including discontinuous, continuous, and continuous-discontinuous models, discussing their advantages, limitations, and applications.

2.1 Constitutive modeling

The constitutive modeling of a material involves describing its response to different loading conditions, characterizing its physical properties and providing the stress-strain relations. In addition, identification of the onset and description of the evolution of material failure are also required.

Predicting material failure is an important field of study. The development of models that are both efficient and accurate has been the focus of a great number of authors in the past decades and major developments were achieved. In the literature, considering failure criteria, materials are classified in a range from ductile, at one end, to brittle at another. Ductile fracture is characterized by large deformation associated with yielding and plastic flow. On the other hand, brittle failure is usually sudden and preceded by small deformation without appreciable plastic deformation (Gdoutos, 2005).

As presented by Bažant and Planas (1998), the failure behavior of a material is strongly influenced by the relative size of the *fracture process zone* (FPZ) in comparison to the overall structural dimensions. The FPZ is a nonlinear region characterized by progressive softening, where stress decreases as deformation increases. When the length of this zone, l_{LPZ}, is relatively small, the material exhibits brittle failure, with the entire fracture process occurring at the crack tip.

A second type of failure behavior can be identified when the fracture zone remains small, but a significant portion of the nonlinear region consists of elastoplastic hardening or perfect yielding. This is classified as *ductile* failure, which is typical in many ductile metals and certain alloys.

The third failure mode occurs when the hardening or perfect yielding zone is minimal or negligible, leading to a *quasi-brittle* failure. This behavior is observed in materials such as concrete, rocks, cemented sands, ceramics, and fiber-reinforced composites (Bažant and Planas, 1998).

This macroscale behavior of a material is strongly influenced by its characteristics at the *atomic* and *microscales.* At the atomic scale, a solid is composed of atoms and molecules that are bonded together, and the properties of the material are determined by the interactions between these discrete particles. This level of observation allows for the detection of defects such as atomic vacancies and dislocations. On the microscale, the solid exhibits heterogeneity, and its microstructure, including grains and fibers, as well as defects like microcracks, pores, and slips, can be clearly identified. On the macroscale the solid is idealized as a continuous body, and only larger defects such as macrocracks and shear bands can be observed (Krajcinovic and Lemaitre, 1987, Van Mier, 1995, Krajcinovic, 1996). These three levels of observation and modeling are depicted in Fig. 2.1.

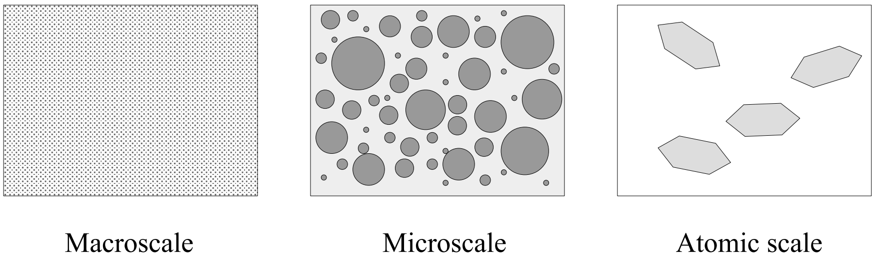

Figure 2.1: Material structure: macro, micro, and atomic scales (adapted from Van Mier, 1995)

The choice of scale for modeling is directly related to the selection of analytical models and their structure. The preference for continuum models that deal with homogeneous media is justified by their relatively simple mathematical structure and computational efficiency. However, these theories have limitations in their applicability, particularly in solids that contain a significant number of heterogeneities, such as defects and grains, which directly influence the macroscopic behavior.

As a material is subjected to certain loads, its structure may start to deteriorate, resulting in the formation of cracks that weaken the solid and diminish its load-carrying capacity. These defects, being discrete entities, introduce disturbances in the material continuum. To accurately analyze their influence, it would be necessary to consider the discrete nature of these defects.

Considering the heterogeneity of materials, models for damage and failure analysis may be divided into *macroscopic* and *microscopic*[1] models. Macroscopic models consider a homogeneous material, neglecting the heterogeneous composition of the microscale.

---

[1] In the literature, models that capture material heterogeneity are usually called *mesoscopic* models.

Depending on the crack representation, these models can be roughly classified as *discontinuous* or *continuous*. On the other hand, microscopic models explicitly represent the heterogeneity describing its multiple phases. Microscopic models will not be discussed, as the present study focus on homogeneous models. The reader is referred to Mukhtar and El-Tohfa (2023) and the references within for a review on microscopic heterogeneous models.

In the following sections, a brief review of discontinuous and continuous numerical approaches is presented, although completeness is not claimed. The focus will be the finite element method (FEM), considering its arguably large use and the scope of this study. Modeling of failure and damage can also be carried out applying the boundary element method (BEM) (Saleh and Aliabadi, 1995), the discrete element method (DEM) (Camborde et al., 2000), meshless methods (Belytschko et al., 1996, Nguyen et al., 2008), and hybrid approaches (Munjiza et al., 1999, Ooi and Yang, 2010).

2.1.1 Discontinuous approach

A *discontinuous approach* (also referred to as discrete approach) considers the insertion of a displacement discontinuity into the mesh as the crack extends between elements or within an element. This discontinuity will be called hereafter a *strong discontinuity*, which, in physical terms, corresponds to a sharp crack (Jirásek, 2001). The kinematic description for a strong discontinuity is schematically shown in Fig. 2.2(c) for the one-dimensional case in classical media. The classical strain field, $\varepsilon(x)$, consists of a regular part and a singular part that assumes the behavior of a Dirac delta distribution. The displacement field $u(x)$ presents a jump, which can be a discontinuity curve (for a two dimensions analysis) or a discontinuity surface (for a three dimensions analysis).

The discontinuous approach is based on the theory of fracture mechanics, which defines criteria for crack initiation and propagation. Considering the finite element method, the discrete approach was the first to be applied mainly due to its simplicity and physical meaning. In this approach cracks were modeled simply by separating elements as a failure condition was met (Ngo and Scordelis, 1967, Nilson, 1968). This approach is mainly used in situations where there is one crack or a finite number os cracks in the structure (Cendón et al., 2000). One major advantage of discrete approaches, as pointed out by de Borst (2022), is the fact that the crack width is directly available. This quantity is particularly important in analyses of fracture propagation in fluid-saturated porous media, in which the crack width is directly linked to the amount of fluid that is transported in the fracture.

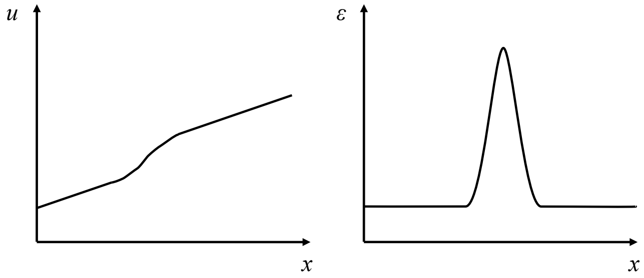

(a) no discontinuity

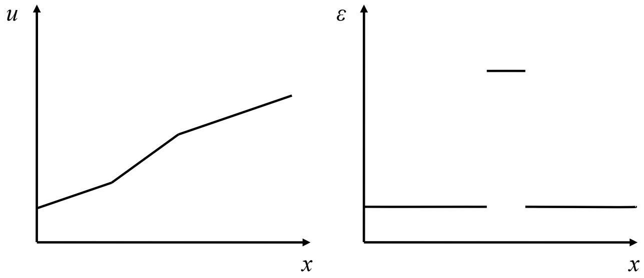

(b) weak discontinuity

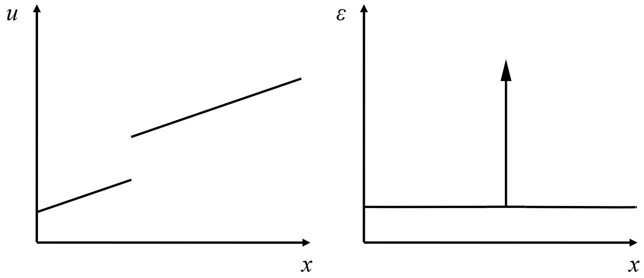

(c) strong discontinuity

Figure 2.2: Kinematic description (adapted from Jirásek, 2001)

One of the first studies in the field of the classical linear theory of fracture mechanics, as pointed out in the relevant literature, is Griffith (1921). Based on experimental tests with glass, a material classified as brittle, Griffith postulated an energy failure criterion of fracture that has been a cornerstone of linear elastic fracture mechanics (LEFM). Considering the rather specific application of Griffith's idea, numerous studies were developed between the 1940s and the 1970s in order to generalize his hypotheses for any geometry and loading, coining the term *energy release rate*. Usually called $\mathcal{G}$, the energy release rate is related to the energy available to advance the crack by a unit area (Bažant and Planas, 1998).

An important step in the development of the theoretical foundation of LEFM is introduced by Irwin (1957), which formulated the concept of stress intensity factor K as a parameter for the intensity of stresses close to the crack tip as a function of the energy release rate. One last theoretical step in the energetic approach to fracture was the

J-integral presented by Rice (1968*a*,*b*). It led to a more complete comprehension of the relation between the energy release rate and the stress and strain fields near the crack end for linear and non-linear elastic materials. This idea is the foundation for non-linear theories. As applications of the linear theory started to emerged, its validity only for very brittle fracture was highlighted and there was the need for a non-linear theory that could account for materials that did not remain elastic up until fracturing. Concrete is a material that cannot be completely described using LEFM because there is a relatively large non-linear zone near the crack tip that should not be neglected.

One possibility for describing the fracture process in full, although with some simplifications, is considering the process zone lumped into the crack line and described by a stress-displacement law with softening (Bažant and Planas, 1998). Such an approach can be found as a *cohesive crack model* in relevant literature and was introduced in the sixties by Barenblatt (1962) for brittle fracture and Dugdale (1960) for ductile one, having since been used by many researchers to describe the fracture of various materials such as metals, polymers, and ceramics. Having in mind quasi-brittle material, such as concrete, the extension of the model proposed by Hillerborg et al. (1976) and named *fictitious crack model* is more appropriate.

Considering the fracture modeling in a FEM framework, inter-element approaches, have an important limitation as cracks can only develop across element boundaries, conditioning the crack geometry to the mesh topology. The use of a mesh with predetermined element orientations that align with known crack paths (Lotfi and Shing, 1994, Lourenço and Rots, 1997, Cendón et al., 2000, Gálvez et al., 2002, Petracca et al., 2017) or the continuously adaptation of the mesh (i.e., remeshing) (Shephard et al., 1985, Martha et al., 1993) are approaches that can deal with the above limitation.

Adding new nodes to the model and remeshing is computationally expensive and has led to the development of the *Embedded Finite Element Method* (E-FEM), in which the effect of the crack is simulated within the element (see Jirásek (2000) for an early review), and the *eXtended Finite Element Method* (XFEM) that captures displacement discontinuities by enriching the kinematics of the nodes located at elements that are intersected by a crack. As the XFEM is of interest for the present study, it is further explored in Chapter 5.

2.1.2 Continuous approach

Alternatively, a crack can be simulated smeared over a certain region, the *localization band*, in the *continuous approach* (or *smeared crack approach*). In this method the crack can be considered from a *local* or *regularized* perspective. The first option, depicted in Fig. 2.2(b), the region of localized deformation is represented by a thin band of finite thickness. This band is separated from the rest of the body by a *weak discontinuity*, which can be curves or surfaces where certain strain components have a jump, but the displacement field remains continuous. Physically, the band between weak discontinuities can be interpreted as a damage process zone that has an almost constant density of microdefects. In Fig. 2.2(a) is shown the second and most regular option in which the displacement and strain fields remain *continuous*. The high strains are spread over the band and there is a smooth transition to lower strains in the surrounding areas. Physically, this process can be viewed as a damage process zone where defects concentrate around the center (Jirásek and Zimmermann, 2001*b*).

The continuous and discontinuous approaches are connected as the latter may be interpreted as the limit case of the former when the width of the localization band tends to zero (Manzoli et al., 1998, Saloustros et al., 2019).

Kachanov (1958) proposed *continuum damage theories*, which model the medium at the macroscale as a continuous body and represent the collective effect of damage through field variables known as *damage variables*. Consequently, a discrete process is represented by a continuous variable, simplifying the computational aspect while sacrificing some accuracy in modeling the deterioration.

The hypothesis of a continuum body is based on the definition of a *representative volume element* (RVE). The RVE is structurally entirely typical of the whole mixture on average and allows, in the transition from microscopic to macroscopic variables, the averaging of certain tensor fields over the system (Hill, 1963, 1967). In other words, as define by Nemat-Nasser and Hori (1993), the RVE for a material point of a continuum mass is a material volume which is statistically representative of the infinitesimal material neighborhood of that material point.

Figure 2.3 illustrates a continuum and identifies a material point P. When the material point is magnified it may have its own complex microstructure composed by grains, voids, cracks, and other heterogeneities. To be representative, the RVE must include a considerable number of these microheterogenities in order to represent the local properties by their mean values through continuous variables (Nemat-Nasser and Hori, 1993). According to Lemaitre (1987), roughly speaking:

- 0.1 × 0.1 × 0.1 mm for metals;
- 1 × 1 × 1 mm for polymers and composites;
- 10 × 10 × 10 mm for wood;
- 100 × 100 × 100 mm for concrete.

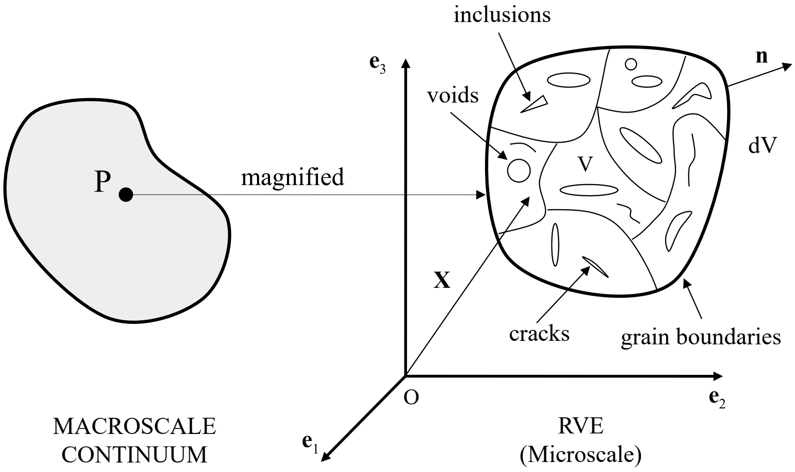

Figure 2.3: RVE as a material point with a possible microstructure (Nemat-Nasser and Hori, 1993)

Considering the diffused damage experienced by concrete structures, the smeared crack model was well accepted for the simulation of cracking in quasi-brittle material. Its initial application was for modeling prestressed concrete vessels, as proposed by Rashid (1968). This approach gained popularity due to its flexibility in crack orientation and simplified implementation in finite element codes. It only requires modifications to the stiffness matrix after reaching peak strength to model the effect of numerous parallel cracks with infinitesimally small openings continuously distributed throughout the finite element. However, as the mesh-dependency and numerical instability of the model was noted for material exhibiting *strain softening*, i.e., a post-peak gradual decline of stress at increasing strain, particular efforts had to be made in order to address the problem (Pietruszczak and Mróz, 1981) leading to regularization techniques.

The regularized smeared crack approaches include various models such as *generalized continua*, *non-local*, *gradient-enhanced*, and *phase-field* models. *Generalized continua*, such as the micropolar (de Borst, 1991, Steinmann and Willam, 1991) and micromorphic theories (Silva et al., 2022), enrich the continuum description by incorporating additional degrees of freedom. These will be discussed in more detail in Chapter 3. In *non-local* models the strain is not local, i.e., the state of deformation at a point is influenced by the deformation in its neighborhood as well (Bažant and Lin, 1988, Bažant and Jirásek, 2002). *Gradient-enhanced models*, on the other hand, consider non-locality by incorporating higher-order strain gradients in the constitutive equations (Vardoulakis and Aifantis, 1991, de Borst and Mühlhaus, 1992).

Lastly, in the last decade, *phase-field* models (PFM) have been proposed as a variational approach to fracture. PFM is categorized as a diffuse crack model in which a scalar field variable is introduced to differentiate between damaged and undamaged regions and to track crack propagation. The phase-field approach has gained significant attention in recent years due to its advantages, such as the automatic prediction of crack initiation, propagation, and the description of complex behaviors like branching and merging. For a comprehensive review, the reader can refer to Ambati et al. (2015) and Egger et al. (2019). However, despite these benefits, phase-field models are computationally expensive as they require highly refined meshes to accurately capture the diffused crack (Patil et al., 2018), and the commonly used staggered numerical schemes tend to converge slowly (Ambati et al., 2015). It is worth mentioning that applications that combine XFEM and phase-field models to simulate crack propagation are possible, as proposed by Giovanardi et al. (2017).

A related point to consider is the strong links between generalized continuum mechanics and phase field and gradient-enhanced models, as highlighted by Forest (2009) and Forest et al. (2011). These formulations can also be integrated into the (generalized) framework of micromorphic media, where the term “micromorphic” is used in a broader sense than in the original expression coined by Eringen and Şuhubi (1964) and Suhubi and Eringen (1964).

2.1.3 Continuous-discontinuous approach

Besides the crack representation with either a discrete (discontinuous) or smeared crack (continuous) approach, there is also the option to combine both methods. These hybrid *continuous-discontinuous* strategies simulate initial micro-cracking using a continuous model, and then, when material degradation reaches a specific threshold, crack formation is simulated through the introduction of a strong discontinuity. As pointed out by de Borst (2022), even though smeared and discrete crack approaches were originally developed based on different assumptions, it seems that their evolution has made them grow closer.

Numerous continuous-discontinuous models have been proposed in the literature, employing different strategies for crack representation. In the case of simulating with finite elements with embedded cracks as proposed by Jirásek and Zimmermann (2001*a*), it was noted by Jirásek and Zimmermann (2001*b*) that the discontinuity direction was inaccurately predicted due to the strong discontinuity being introduced right at the onset of damage. To address this issue, the authors proposed a combined model called the *delayed embedded crack model*, which combines a smeared crack model with a transition to an embedded crack. In this model, the strong discontinuity is only introduced when the crack opening reaches a critical value. Once the transition is made, the bulk material is considered as linear elastic with the stiffness defined by the secant (unloading) stiffness of the smeared model at the time of transition. To further enhance the model, the authors proposed the use of a non-local formulation for damage, reducing mesh sensitivity by replacing the local equivalent strain with its weighted average over a certain neighborhood of a given point. One important advantage of the embedded approach for the crack is that they are not limited to element edges, as inter-element models, being arbitrarily aligned within the element. However the discontinuity propagates in increments no smaller than the element size.

Also based on a non-local continuum damage model, Comi et al. (2007) proposes a strategy that detects the formation of a strong discontinuity based on a critical threshold damage estimated on the basis of a perturbation analysis. As the critical damage is exceeded, a discrete cohesive crack is introduced in the element adopting an XFEM approach. Similarly to Jirásek and Zimmermann (2001*b*), the cohesive law is defined through an energy balance, so the energy not yet dissipated is transferred to the cohesive interface while the bulk material unloads. A mode I loading condition was adopted by the authors. Simone et al. (2003) also applied the XFEM approach to model strong discontinuities but in a gradient-enhanced continuum, in which gradient terms are introduced into the constitutive equations. An elastic isotropic damage model is employed for the continuous damage and, as soon as damage is close to a critical situation in the element ahead of a discontinuity tip, the traction-free discontinuity is extended with orientation defined based on the direction of maximum accumulation of the non-local equivalent strain in a V-shaped window ahead of the crack tip.

Einsfeld (1997) proposed a continuous-discontinuous approach considering a plasticity model in which a discrete crack is inserted between elements adopting an energy criterion. The crack is introduced in a direction identified based on a principal stresses analysis and the mesh is reconstructed.

As noted, a criteria to define where and when to insert a crack increment is essential for continuous-discontinuous strategies. Besides the criteria already mentioned, instability or loss of ellipticity is a possible criteria for coupling the models. One such example is the strong discontinuity approach presented by Oliver et al. (2002). The authors propose a model in which the discrete crack is modeled as a weak discontinuity that collapses into a strong discontinuity at a certain time of the deformation process. The formation of a weak discontinuity is detected using a local bifurcation analysis based on the singularity of the acoustic tensor (more details in Section 4) and the strain fields localizes inside a localization band. The bandwidth decreases following a specified evolution law, and, when the band-width reaches a critical value, a strong discontinuity is introduced. The crack is modeled using embedded elements. This model is illustrated in Fig. 2.4: material points in front of the crack tip, initially characterized by a linear behavior, reach the non-linear behavior (zone **Y-B**) but the zone still remains continuous. These point, as they bifurcate, are described by a weak discontinuity kinematics with a non-zero bandwidth (zone **B-SD** in Fig. 2.4). Lastly, as the material points approach a null point, they reach the strong discontinuity regime (zone S in Fig. 2.4).

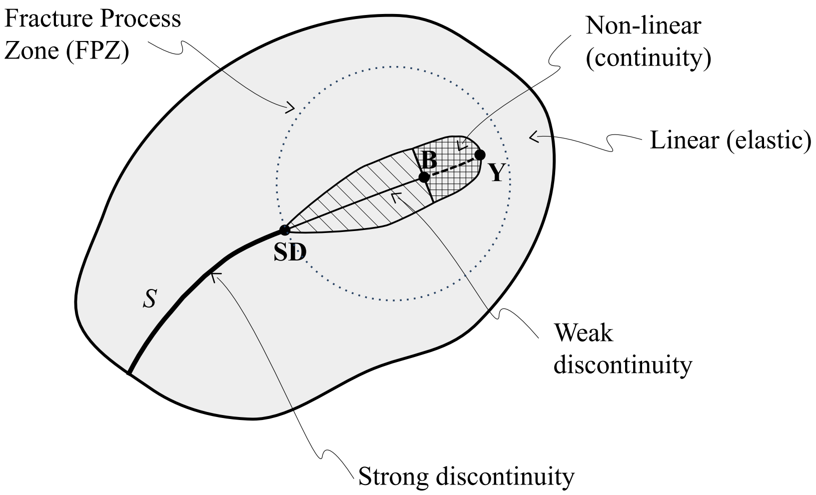

Figure 2.4: The fracture process zone modeled by the strong discontinuity approach (adapted from Oliver et al., 2002)

Considering the dynamic case, cracks can be inserted as loss of hyperbolicity, the equivalent to loss of ellipticity for dynamic loads, is detected by an indicator that also enables both the crack speed and crack direction to be determined for a given material point, as proposed by Belytschko et al. (2003). The authors considered a scalar-isotropic damage model transitioning to a dynamic discrete crack modeled with the extended finite element approach.

Chapter 3

Micromorphic Media

This chapter presents the theoretical basis of micromorphic continua. It provides an overview of generalized continuum theories, detailing the micromorphic formulation and its elastic-degrading framework used for modeling continuous damage.

3.1 Generalized continua

In the *classical continuum mechanics* approach, every point within a material is occupied by a small solid element called a *material particle*. While these particles can be thought of as mathematical points due to their small size relative to all characteristics lengths, they are still significantly larger than atomic dimensions (Mal and Singh, 1991). The translational degrees of freedom of these particles and the resulting measures of deformation describe the medium kinematics. This paradigm of classical continuum mechanics draws from the ideas of Leonard Euler (1707-1783), Joseph L. Lagrange (1736-1813), and Augustin L. Cauchy (1789-1857), and the divergence theory proposed by George Green (1793-1841) (Maugin, 2017).

Constitutive equations for inhomogeneous materials in the classical continuum theory are developed using the idea of a representative volume element (RVE) associated with the material particle (Hashin, 1983, Kröner, 1977, Willis, 1981). Furthermore, the kinematics and statics descriptions of the medium consider only average macroscopic characteristics, disregarding the microstructure constituents behavior. These hypotheses suffice in the analysis of usual structures in the engineering field, but theories that incorporate information on the material microstructure are necessary in situations where the RVE concept does not represent all related phenomena. This is the case for many materials that are characterized by a heterogeneous microstructure made of grains immersed in a solid matrix with micro-cracks and porosity, as illustrated in Fig. 3.1

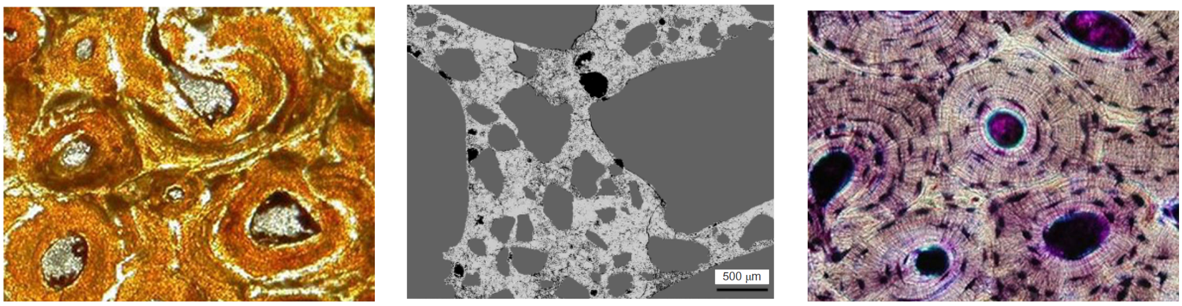

(a) sedimentary rock (b) concrete (c) compact bone

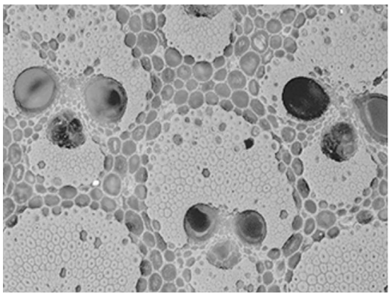

(d) bamboo

Figure 3.1: Materials with heterogeneous microstructure (Giorgio et al., 2020, Wong et al., 2009)

To deal with the above limitations, a *generalized continuum mechanics* approach was proposed based on the expansion of the basic working hypotheses of standard continuum mechanics of Cauchy. The first studies in this field are considered to be Voigt (1887) and Cosserat and Cosserat (1909). The generalized theories found in the relevant literature can be broadly categorized into two types: *higher-order continua*, which involves additional degrees of freedom; and *higher-grade continua*, which considers higher order gradients of the displacement field (Germain, 1973*a*,*b*, Forest, 1998, Hirschberger, 2008).

From the point of view of the classical continuum, only the linear term is considered in the deformation map and, hence, the vicinity of the material particle stays unconsidered (*local* continuum theory). If the quadratic term (second-order theory, see Mindlin (1965)) or even higher-grade terms are considered in the non-linear deformation mapping, a higher-grade continuum is obtained. This type of continuum is useful in cases where the linear term is insufficient to describe the behavior of the medium, and higher-order terms can account for size effects (Hirschberger, 2008).

Higher order continua, in contrast, are characterized by additional degrees of freedom per material point, rather than higher gradients of deformation. From a microscopic perspective, each material point in the macrocontinuum is a continuum of small extent, being its kinematics described by a linear deformation map. It is assumed that embedded in each point is a microcontinuum, whose kinematics defines the additional degrees of freedom (Germain, 1973*b*, Mindlin, 1964, Hirschberger, 2008). Considering a material carrying three deformable director, nine extra degrees of freedom are introduced besides the translational degrees of freedom of the classical theory (case of the micromorphic continuum with 12 degrees of freedom).

These generalized theories are able to capture size-effects and are particularly suited for materials with a significant microstructure due to the characteristics of their formulation. Since the introduction of these general continuum models, numerous derived theories have been proposed in the literature with different choices of kinematical variables and constitutive variables. The micromorphic theory is the most general higher-order theory and is better developed in the next section.

3.2 Micromorphic continuum theory

The micromorphic theory, developed by Eringen and Şuhubi (1964), Suhubi and Eringen (1964), Mindlin (1964), accounts for the so-called microdeformation and its gradient in addition to the macroscopic strain, being thus able to provide a more detailed description of the material state. This generalized theory is able to model more realistically a large class of engineering materials, as porous solids (Hütter et al., 2015), heterogeneous materials (Biswas and Poh, 2017, Zhi et al., 2022), as well as biological materials (Massing et al., 2023).

However, due to this more detailed description of the microscopic state, additional constitutive equations for higher-order stresses are required, resulting in a significant increase in the number of independent constitutive parameters. For an isotropic linear elastic material the number of parameters rises from 2 to 18 when going from the classical Cauchy continuum to a fully micromorphic one. Recently, some progress has been made in the interpretation of micromorphic constitutive relations (Hütter, 2023).

Hence, even with its praised potential, the full micromorphic theory is not widely adopted in the literature, being its sub-classes more employed, like the Cosserat theory (also know as micropolar) or strain gradient theory. For the Cosserat theory, there are four additional parameters that can be be identified experimentally or numerically (see, e.g., Lakes (1986)). However, the Cosserat theory is not able to represent all effects observed in real materials. In problems with localization of deformation, as explored by de Borst et al. (1993), the micropolar continuum is more effective as a regularization method for mode-II failures, being otherwise a weaker regularization technique.

In the last decades, particular effort has been devoted to homogenization methods to derive constitutive laws for generalized theories, as proposed by Forest and Sab (1998) (Cosserat continuum), Yang et al. (2022) (strain gradient continua) and Silva et al. (2022) (micromorphic continuum).

It is noteworthy that higher order continua are referred to as *micromorphic continua of order n* in the works of Germain (1973*b*) and Eringen (1966). However, the practicality of continua of order $n > 1$ is questionable, considering that the first-order theory is already complex enough for most physical applications. Additionally, if the continuum undergoes small deformation, higher-order terms may be neglected, as in the case of neglecting higher order displacement gradients in the deformation of an elastic solid (Eringen, 1966). Therefore, this work is only concerned with the case of grade 1 ($\alpha = 1$).

In order to represent the intrinsic deformation of a point, each deformable particle is replaced with a geometrical point P and some vectors attached to P. A particle P is defined by its position vector $\boldsymbol{X}$ ($X_K, K = 1, 2, 3$) in the reference state B and vectors attached to P, representing the inner structure of P by $\Xi_\alpha, \alpha = 1, 2, \ldots, N$. Both $\boldsymbol{X}$ and Ξ_α have their own motions

$$\boldsymbol{X} \xrightarrow{t} \boldsymbol{x}, \qquad \Xi_\alpha \xrightarrow{\boldsymbol{X},t} \boldsymbol{\xi}_\alpha, \qquad \alpha = 1, 2, \ldots, N. \tag{3.1}$$

Such a medium may be called microcontinuum of *grade N*. For the first order theory of the micromorphic continuum, the kinematics of each material particle is described by the mapping ($\Xi \xrightarrow{\boldsymbol{X},t} \boldsymbol{\xi}$) of its attached vector Ξ, located at the centroid of the particle,

$$\boldsymbol{\xi} = \boldsymbol{\chi}(\boldsymbol{X}, t)\ \Xi_K \tag{3.2}$$

in which

$$\boldsymbol{\chi}_K(\boldsymbol{X}, t) = \left.\frac{\partial \boldsymbol{\xi}}{\partial \Xi_K}\right|_{\Xi=0} \tag{3.3}$$

As exposed in Eringen (1999), the second order tensor $\boldsymbol{\chi}$ is called *microdeformation* tensor (alternatively, *deformable directors*) and represents three deformable directors related to the degrees of freedom arising from microdeformations of the physical particle. Thus, the micromorphic continuum is none other than a classical continuum endowed with nine additional degrees of freedom, being six related to the *micro deformations* and three to the *micro rotations*. The kinematics of a point can be illustrated with the deformable director triad as shown in Fig. 3.2.

According to the polar decomposition theorem, a matrix may be decomposed as product of an orthogonal matrix and a symmetric matrix (Mal and Singh, 1991, Eringen, 1980). Hence, the tensor $\boldsymbol{\chi}$ can be written as

$$\boldsymbol{\chi} = \boldsymbol{RU} = \boldsymbol{VR} \tag{3.4}$$

where $\boldsymbol{R}$ represents the *micro rotation tensor* related to rigid rotations, and $\boldsymbol{U}$ and $\boldsymbol{V}$ are called *right* and *left stretch tensors* for micro deformations.

In a micromorphic continuum the particle may experience stretching/compression and rotation comprised in the tensor $\boldsymbol{\chi}$ (Fig. 3.2). Several sub-theories can be derived from the general case applying constraints to the deformation of the microcontinuum, i.e., to the micro-deformation tensor $\boldsymbol{\chi}$ (Eringen, 1999, Hirschberger, 2008). The micromorphic theory and its sub-theories are grouped under the name *microcontinuum theories*, being this classification and the corresponding continuum frameworks well elaborated by Eringen (1999).

For instance, considering that the *micropolar continuum* (or *Cosserat continuum*) (Cosserat and Cosserat, 1909, Eringen, 1999) may only experience rotation, it can be obtained by assuming $\boldsymbol{\chi} = \boldsymbol{R}$, as illustrated in Fig. 3.3 with the rigid director triad. If a scalar variable χ, besides the rotation $\boldsymbol{R}$, is incorporated to account for isotropic extension, i.e., $\boldsymbol{\chi} = \chi\boldsymbol{R}$, the *microstretch continuum* (Eringen, 1999) is obtained, as depicted in Fig. 3.4. For the case in which only the stretch tensor $\boldsymbol{U}$ is considered and the rotation is neglected ($\boldsymbol{\chi} = \boldsymbol{U}$), as seen in Figure 3.5, the *microstrain continuum*, proposed by Forest and Sievert (2006), may be derived.

Lastly, if both stretch and rotation are restrained, the classical continuum is obtained, where the hypotheses of unalterable particles is considered. As seen in Fig. 3.6, for this case, $\boldsymbol{\chi} = \boldsymbol{I}$, in which $\boldsymbol{I}$ is the second order identity tensor.

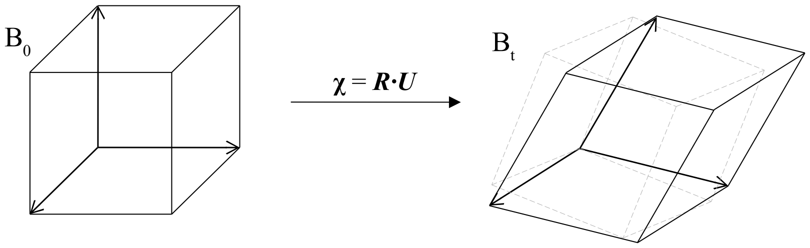

Figure 3.2: Micromorphic micro deformation: deformable director triad

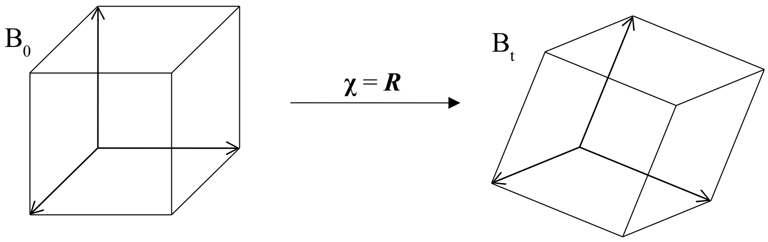

Figure 3.3: Micropolar micro deformation: rigid director triad

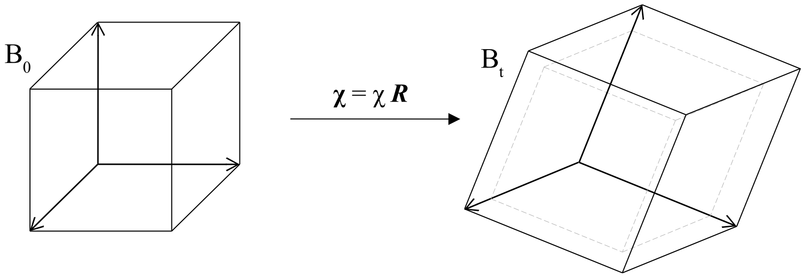

Figure 3.4: Microstretch micro deformation: extensible director triad

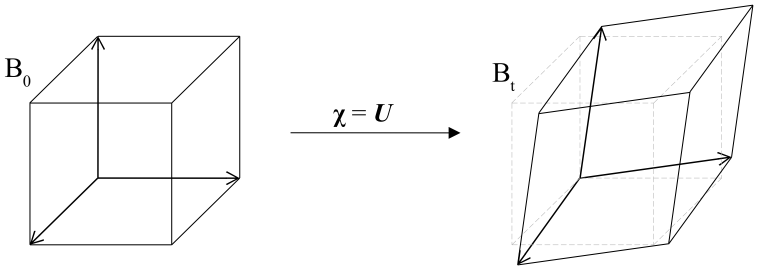

Figure 3.5: Microstrain micro deformation: stretchable director triad excluding rotation

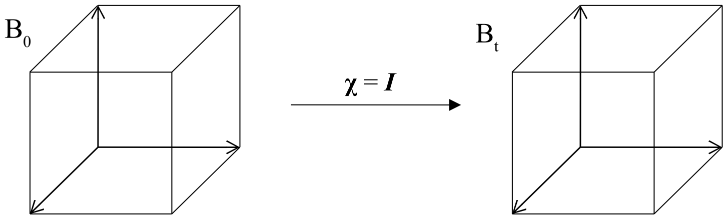

Figure 3.6: Classical micro deformation: no director triad

3.2.1 Kinematics of Deformation

A material point $P(\boldsymbol{X}, \boldsymbol{\Xi}) \in B$ is characterized by its centroid C and vector $\boldsymbol{\Xi}$ attached to C. The point C is identified by its rectangular coordinates X_K $(K = 1, 2, 3)$ and the vector $\boldsymbol{\Xi}$ by its components Ξ_K $(K = 1, 2, 3)$. Under solicitation, motion accompanied by deformation of the solid occurs and the point $P(\boldsymbol{X}, \boldsymbol{\Xi})$ is carried to $p(\boldsymbol{x}, \boldsymbol{\xi}, t)$ in a spatial frame of reference b, so that, $X_K \longrightarrow x_k, \Xi_K \longrightarrow \xi_k (K = 1, 2, 3; k = 1, 2, 3)$ (Fig. 3.7).

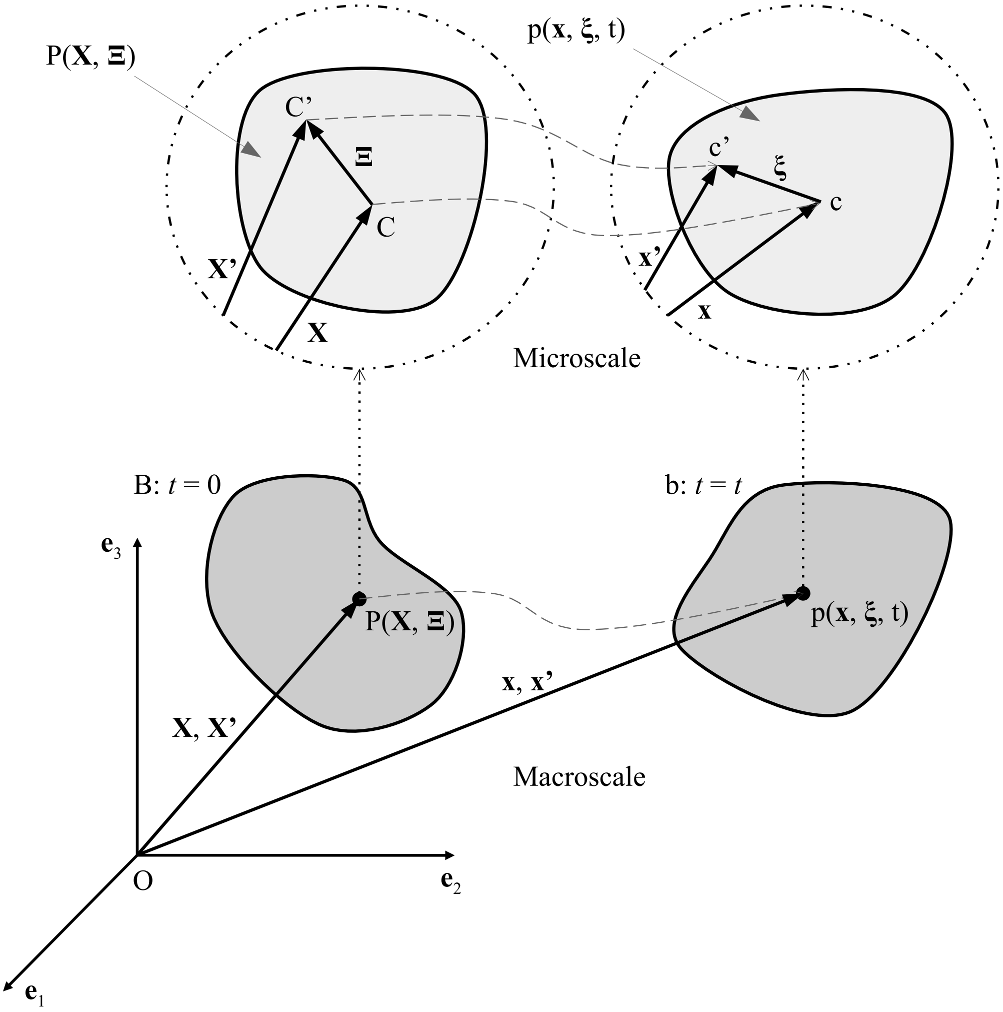

Figure 3.7: Micromorphic continuum kinematics (Silva, 2019)

As aforesaid, Ξ and $\boldsymbol{\xi}$ have their own motions, expressed by

$$\boldsymbol{X} \longrightarrow \boldsymbol{x} = \boldsymbol{x}(\boldsymbol{X}, t) \quad \text{or} \quad x_k = x_k(X_K, t) \tag{3.5}$$

$$\Xi \longrightarrow \boldsymbol{\xi} = \boldsymbol{\xi}(\boldsymbol{X}, \Xi, t) \quad \text{or} \quad \xi_k = \xi_k(X_K, \Xi_K, t) \tag{3.6}$$

The mapping in Eq. (3.5) is called *macromotion* (or simply, the motion) and Eq. (3.6) the *micromotion*. Considering that the material particles are of very small size (infinitesimally small) relatively to the mascroscopic scale, the micromotion in Eq. (3.6) can be approximated by a linear approximation in Ξ:

$$\boldsymbol{\xi} = \boldsymbol{\chi}_K(\boldsymbol{X}, t)\Xi_K \quad \text{or} \quad \xi_k = \chi_{kK}(\boldsymbol{X}, t)\Xi_K \tag{3.7}$$

where $\boldsymbol{\chi}$ is the microdeformation gradient (alternatively, deformable directors) and defined in Eq. (3.3). Note that $\Xi = 0$ is taken to be the centroid of P in the particle local system.

The motion of the material point $C' \in P$ with coordinates X'_K $(K = 1, 2, 3)$ is, thus, completely described by the macro-micromotion composition

$$\boldsymbol{x}' = \boldsymbol{x}(\boldsymbol{X}, t) + \boldsymbol{\xi}(\boldsymbol{X}, \Xi, t) \tag{3.8}$$

Then, from Eq. (3.7),

$$\boldsymbol{x}' = \boldsymbol{x}(\boldsymbol{X}, t) + \boldsymbol{\chi}_K(\boldsymbol{X}, t)\Xi_K \tag{3.9}$$

Note that, by Eq. (3.7), the motion of the centroid of P is, by definition, entirely described in the macroscale. A material point in the body is now considered to possess three deformable directors ($\mathfrak{X}_k \longrightarrow \boldsymbol{\chi}_K$), as illustrated in Fig. 3.8, which represent the degrees of freedom arising from microdeformations of the physical particle.

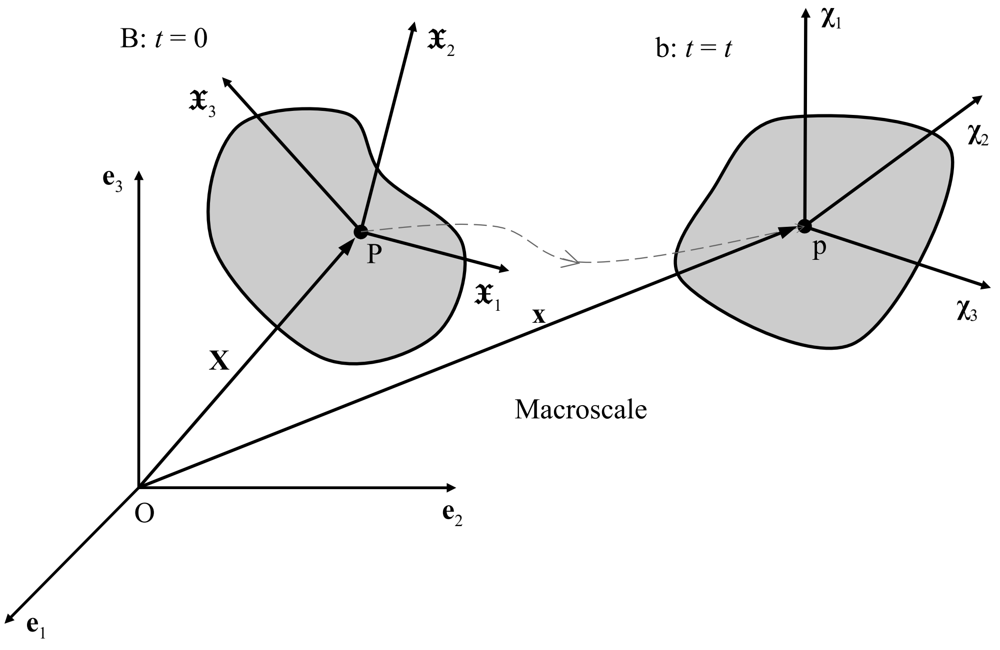

Figure 3.8: Deformable directors

3.2.2 Linear Elasticity

Based on the kinematics of deformation presented here briefly, Eringen and Şuhubi (1964) and Suhubi and Eringen (1964) constructed several sets of strain tensors. One such set of strain measures is given by

$$\mathfrak{C}_{KL} = x_{k,K}\mathfrak{X}_{Lk}, \qquad \mathcal{C}_{KL} = \chi_{kK}\chi_{kL} = \mathcal{C}_{LK}, \qquad \Gamma_{KLM} = \mathfrak{X}_{Kk}\chi_{kL,M} \tag{3.10}$$

where $\mathfrak{C}_{KL}$ is called the *deformation tensor*, $\mathcal{C}_{KL}$ the *microdeformation tensor*, and Γ_{KLM} the *wryness tensor*. In a linear approximation:

$$\mathfrak{C}_{KL} - \delta_{KL} \approx \epsilon_{kl}\delta_{kK}\delta_{lL}, \quad \mathcal{C}_{KL} - \delta_{KL} \approx 2e_{kl}\delta_{kK}\delta_{lL}, \quad \Gamma_{KLM} = \gamma_{klm}\delta_{kK}\delta_{lL}\delta_{mM} \tag{3.11}$$

in which ϵ_{kl}, e_{kl}, and γ_{klm} are the linear strain tensors defined by

$$\epsilon_{kl} = u_{l,k} - \phi_{lk}, \qquad 2e_{kl} = \phi_{kl} + \phi_{lk}, \qquad \gamma_{klm} = \phi_{kl,m} \tag{3.12a,b,c}$$

where u_l is the *displacement vector* related to the particle centroid and $\phi_{kl} = \chi_{kl} - \delta_{kl}$ is the *micromotion gradient tensor*. Disregarding temperature variations the *free energy density* ψ is, then, approximated by

$$\begin{aligned} \psi \approx \psi^0 &+ \frac{1}{2}A_{klmn}\epsilon_{kl}\epsilon_{mn} + \frac{1}{2}B_{klmn}e_{kl}e_{mn} + \frac{1}{2}C_{klmnpq}\gamma_{klm}\gamma_{npq} + E_{klmn}\epsilon_{kl}e_{mn} + \\ &+ F_{klmnp}\epsilon_{kl}\gamma_{mnp} + G_{klmnp}e_{kl}\gamma_{mnp} \end{aligned} \tag{3.13}$$

where ψ^0 is the initial internal energy density; $A_{klmn}, B_{klmn}, C_{klmnpq}, E_{klmn}, F_{klmnp}$ and G_{klmnp} are the constitutive moduli with the following symmetries (Eringen, 1999)

$$\begin{gathered} A_{klmn} = A_{mnkl}, \qquad B_{klmn} = B_{mnkl} = B_{lkmn} = B_{nmkl}, \\ C_{klmnpq} = C_{npqklm}, \qquad E_{klmn} = E_{klnm}, \qquad G_{klmnp} = G_{lkmnp}\ . \end{gathered} \tag{3.14}$$

From Eq. (3.13), the linear constitutive equations of a micromorphic solid can be obtained:

$$t_{kl} \approx \frac{\partial\psi}{\partial\epsilon_{kl}} = A_{klmn}\epsilon_{mn} + E_{klmn}e_{mn} + F_{klmnp}\gamma_{mnp} \tag{3.15}$$

$$s_{kl} \approx \frac{\partial\psi}{\partial e_{kl}} = E_{mnkl}\epsilon_{mn} + B_{klmn}e_{mn} + G_{klmnp}\gamma_{mnp} \tag{3.16}$$

$$m_{klm} \approx \frac{\partial \psi}{\partial \gamma_{lmk}} = F_{nplmk}\epsilon_{np} + G_{nplmk}e_{np} + C_{lmknpq}\gamma_{npq} \tag{3.17}$$

where t_{kl} is the *stress tensor*, s_{kl} is a symmetric stress tensor named *micro-stress average tensor*, and m_{klm} is the *stress moments tensor* or the *first stress moments* and represented by the symbol λ^{klm} (Eringen and Şuhubi, 1964).

For an isotropic linear elastic micromorphic solid the constitutive equations in Eqs. (3.15), (3.16), and (3.17) can be simplified applying the appropriated symmetries (Eringen, 1999) and the constitutive moduli may be constructed by the product of the Kronecker delta δ_{kl}:

$$\begin{aligned}
A_{klmn} &= \lambda\delta_{kl}\delta_{mn} + (\mu+\kappa)\delta_{km}\delta_{ln} + \mu\delta_{kn}\delta_{lm},\\
E_{klmn} &= (\lambda+\nu)\delta_{kl}\delta_{mn} + (\mu+\sigma)(\delta_{km}\delta_{ln} + \delta_{kn}\delta_{lm})\\
F_{klmnp} &= 0,\\
B_{klmn} &= (\lambda+2\nu+\tau)\delta_{kl}\delta_{mn} + (\mu+2\sigma+\eta)(\delta_{km}\delta_{ln} + \delta_{kn}\delta_{lm}),\\
G_{klmnpq} &= 0,\\
C_{klmnpq} &= \tau_1(\delta_{kl}\delta_{mn}\delta_{pq} + \delta_{kq}\delta_{lm}\delta_{np}) + \tau_2(\delta_{kl}\delta_{mp}\delta_{nq} + \delta_{km}\delta_{lq}\delta_{np}) +\\
&+ \tau_3\delta_{kl}\delta_{mq}\delta_{np} + \tau_4\delta_{kn}\delta_{lm}\delta_{pq} + \tau_5(\delta_{km}\delta_{ln}\delta_{pq} + \delta_{kp}\delta_{lm}\delta_{nq}) +\\
&+ \tau_6\delta_{km}\delta_{lp}\delta_{nq} + \tau_7\delta_{kn}\delta_{lp}\delta_{mq} + \tau_8(\delta_{kp}\delta_{lq}\delta_{mn} + \delta_{kq}\delta_{ln}\delta_{mp}) +\\
&+ \tau_9\delta_{kn}\delta_{lq}\delta_{mp} + \tau_{10}\delta_{kp}\delta_{ln}\delta_{mq} + \tau_{11}\delta_{kq}\delta_{lp}\delta_{mn}
\end{aligned} \tag{3.18}$$

wherein λ, μ, κ, ν, τ, σ, η and $\tau_1 \ldots \tau_{11}$ are 18 elastic parameters.

Disregarding the constitutive moduli of odd order:

$$t_{kl} = A_{klmn}\epsilon_{mn} + E_{klmn}e_{mn} \tag{3.19}$$

$$s_{kl} = E_{mnkl}\epsilon_{mn} + B_{klmn}e_{mn} \tag{3.20}$$

$$m_{klm} = C_{lmknpq}\gamma_{npq} \tag{3.21}$$

The balance laws of micromorphic continua can be obtained considering the *Principle of Stationary Potential Energy*, stated in Dym and Shames (2013) as

$$\delta^{(1)}\Pi = \delta^{(1)}\left(U+V\right) = 0 \tag{3.22}$$

wherein $\delta^{(1)}$ is the first variation of Π; $\Pi = U + V$ é is the total potential energy of the body; U is the strain energy ($U = \int_{\mathcal{V}} U_0 dv$ in which $U_0 = \psi - \psi_0$); and V is the potential energy of the applied loads. Applying this principle to a micromorphic medium

$$\begin{aligned}
\delta^{(1)}U &= \delta^{(1)} \int_{\mathcal{V}} U_0 dv = \int_{\mathcal{V}} \delta^{(1)} U_0 dv = \int_{\mathcal{V}} \left(t_{kl}\delta\epsilon_{kl} + s_{kl}\delta e_{kl} + m_{klm}\delta\gamma_{lmk}\right) dv = \\
&= \int_{\mathcal{V}} \left\{t_{kl}\delta\left(u_{l,k} - \phi_{lk}\right) + s_{kl}\delta\left[\frac{1}{2}\left(\phi_{kl} + \phi_{lk}\right)\right] + m_{klm}\delta\phi_{lm,k}\right\} dv = \\
&= \int_{\mathcal{V}} \left(t_{kl}\delta u_{l,k} - t_{kl}\delta\phi_{lk} + s_{kl}\delta\phi_{lk} + m_{klm}\delta\phi_{lm,k}\right) dv = \\
&= \int_{\mathcal{V}} \left[t_{kl}\delta u_{l,k} + \left(s_{kl} - t_{kl}\right)\delta\phi_{lk} + m_{klm}\delta\phi_{lm,k}\right] dv = \\
&= \int_{\mathcal{V}} \left[t_{kl}\delta u_{l,k} + \left(s_{ml} - t_{ml}\right)\delta\phi_{lm} + m_{klm}\delta\phi_{lm,k}\right] dv \qquad (3.23)
\end{aligned}$$

$$\delta^{(1)}V = -\int_{\mathcal{V}} \left(\rho f_l \delta u_l + \rho l_{lm}\delta\phi_{lm}\right) dv - \int_{\partial\mathcal{V}} \left(\hat{t}_{(\boldsymbol{n})l}\delta u_l + \hat{m}_{(\boldsymbol{n})lm}\delta\phi_{lm}\right) ds \qquad (3.24)$$

where $\mathcal{V}$ is the considered domain; $\partial\mathcal{V}$ is the boundary of the domain; δ is the delta operator, which represent a small arbitrary change in the strain or displacement fields; ρ is the mass density in the reference configuration; f_l is the body force per unit mass; l_{lm} is the body couple per unit mass; $\hat{t}_{(\boldsymbol{n})l}$ is the stress vector; $\hat{m}_{(\boldsymbol{n})lm}$ is the surface couple tensor; and $\boldsymbol{n}$ is the unit normal vector on the surface of the body $\partial\mathcal{V}$.

The static balance laws can then be defined based on Eqs. (3.22), (3.23) and (3.24)

$$t_{kl,k} + \rho f_l = 0 \qquad \text{in} \qquad \mathcal{V} \qquad (3.25)$$

$$m_{klm,k} + t_{ml} - s_{ml} + \rho l_{lm} = 0 \qquad \text{in} \qquad \mathcal{V} \qquad (3.26)$$

as well as the boundary conditions

$$u_k = \hat{u}_k \quad \text{on} \quad \partial\mathcal{V}_{\boldsymbol{u}}, \quad t_{kl}n_k = \hat{t}_{(\boldsymbol{n})l} \quad \text{on} \quad \partial\mathcal{V}_{\boldsymbol{t}} \qquad (3.27)$$

$$\phi_{kl} = \hat{\phi}_{kl} \quad \text{on} \quad \partial\mathcal{V}_{\boldsymbol{\phi}}, \quad m_{klm}n_k = \hat{m}_{(\boldsymbol{n})lm} \quad \text{on} \quad \partial\mathcal{V}_{\boldsymbol{m}} \qquad (3.28)$$

in which $\hat{u}_k$ are prescribed components of the displacement vector on $\partial\mathcal{V}_{\boldsymbol{u}}$; $\hat{\phi}_{kl}$ are prescribed components of the microdisplacement tensor on $\partial\mathcal{V}_{\boldsymbol{\phi}}$; and $\partial\mathcal{V}_{\boldsymbol{u}} \cap \partial\mathcal{V}_{\boldsymbol{t}} = 0$, $\partial\mathcal{V}_{\boldsymbol{\phi}} \cap \partial\mathcal{V}_{\boldsymbol{m}} = 0$ e $\partial\mathcal{V} = \partial\mathcal{V}_{\boldsymbol{u}} \cup \partial\mathcal{V}_{\boldsymbol{t}} = \partial\mathcal{V}_{\boldsymbol{\phi}} \cup \partial\mathcal{V}_{\boldsymbol{m}}$.

The theoretical and numerical formulations of micromorphic continua are well established in the literature; however, their practical application is hindered by the complexity of identifying appropriate constitutive laws and the large number of material parameters required. For a linear isotropic micromorphic material, there are 18 elastic parameters, as presented in Eq. (3.18), compared to the two Lamé parameters in a classical isotropic continuum. To overcome these challenges, this study adopts the micromorphic homogenization approach proposed by Silva et al. (2022), which builds upon the work of Hütter (2017).

This method employs a multiscale formulation to derive macroscopic micromorphic constitutive relations from homogenized microscopic quantities, which are obtained by solving boundary value problems at the microscale within the framework of classical continuum mechanics. Since this strategy starts from classical continuum models at the microscale without imposing constitutive assumptions at the macroscale, the required material parameters remain those of the classical theory. Consequently, this homogenization strategy is utilized in the simulations presented in the following chapters.

3.3 A Unified Formulation for Elastic Degradation in Micromorphic Continua

As previously stated, this work proposes a continuous-discontinuous approach for modeling damage and fracture in micromorphic media. To model continuous damage a unified formulation for elastic degradation is utilized which builds upon some relevant works as de Borst (1987), Carol et al. (1994, 2001*a*,*b*), Armero and Oller (2000*a*,*b*), Gori et al. (2017*a*).

To better understand this framework, its basic concepts are discussed considering their extension to accommodate micromorphic media. It is worth mentioning that this framework was already explored in Reges et al. (2023) from the perspective of the compact tensorial formulation, which is recalled in Section 3.3.1. However, the formulation considering each of the micromorphic measures separately is particular of this work, although is has been previously explored for micropolar media by Gori et al. (2017*b*).

The following discussion focuses on a *strain-based* formulation in order to derive the equations for the stress rate tensors for micromorphic media. This formulation is presented in order to ground the study of discontinuous failure in Chapter 4 which is based on the definition of the tangent constitutive operators. Hence, completeness of this unified formulation is not claimed, as only the relevant aspects for this work are discussed.

The starting point for the formulation is the free energy density defined in Eq. (3.13), from which are written in Eq. (3.19)-(3.21) the stress tensor t_{kl}, the micro-stress average tensor s_{kl}, and the stress moments tensor m_{klm} for an isotropic linear elastic micromorphic solid. From the time derivative of the micromorphic stress tensors, it may be seen that each of the stress measures can be decomposed into two parts: an elastic ($\dot{t}^e_{kl}$, $\dot{s}^e_{kl}$, $\dot{m}^e_{klm}$) and a degrading one ($\dot{t}^d_{kl}$, $\dot{s}^d_{kl}$, $\dot{m}^d_{klm}$)

$$\dot{t}_{kl} = \dot{t}^e_{kl} + \dot{t}^d_{kl} \tag{3.29}$$

$$\dot{s}_{kl} = \dot{s}^e_{kl} + \dot{s}^d_{kl} \tag{3.30}$$

$$\dot{m}_{klm} = \dot{m}^e_{klm} + \dot{m}^d_{klm} \tag{3.31}$$

where the elastic part is defined as

$$\dot{t}^e_{kl} = A^S_{klpq}\dot{\epsilon}_{pq} + E^S_{klpq}\dot{e}_{pq} \tag{3.32}$$

$$\dot{s}^e_{kl} = E^S_{pqkl}\dot{\epsilon}_{pq} + B^S_{klpq}\dot{e}_{pq} \tag{3.33}$$

$$\dot{m}^e_{klm} = C^S_{lmkpqn}\dot{\gamma}_{pqn} \tag{3.34}$$

in which A^S_{klpq}, E^S_{klpq}, B^S_{klpq}, and C^S_{lmkpqn} are the *secant* constitutive moduli.

The degrading parts can then be written as

$$\dot{t}^d_{kl} = \dot{\lambda}\mathfrak{m}^a_{kl} \tag{3.35}$$

$$\dot{s}^d_{kl} = \dot{\lambda}\mathfrak{m}^b_{kl} \tag{3.36}$$

$$\dot{m}^d_{klm} = \dot{\lambda}\mathfrak{m}^A_{klm} \tag{3.37}$$

where $\dot{\lambda}$ is the *inelastic multiplier*, and $\mathfrak{m}^a_{kl}$, $\mathfrak{m}^b_{kl}$ and $\mathfrak{m}^A_{klm}$ are the *directions of degradation* for the increments of the stress tensor, the micro-stress average tensor, and the stress moments tensor, respectively.

A *degradation rule* for the secant constitutive operators is now also introduced for completely defining the damage process

$$\dot{A}^S_{klmn} = \dot{\lambda}M^a_{klmn} \tag{3.38}$$

$$\dot{B}^S_{klmn} = \dot{\lambda}M^b_{klmn} \tag{3.39}$$

$$\dot{E}^S_{klmn} = \dot{\lambda}M^c_{klmn} \tag{3.40}$$

$$\dot{C}^S_{lmknpq} = \dot{\lambda}M^A_{lmknpq} \tag{3.41}$$

where $\dot{\lambda}$ is the inelastic multiplier, defining the degrading process magnitude, and M^a_{klmn}, M^b_{klmn}, M^c_{klmn}, and M^A_{lmknpq} are the directions of degradation for the secant constitutive operators. The different directions of degradation can be related by

$$\mathfrak{m}^a_{kl} = \dot{\lambda} M^a_{klmn} \epsilon_{mn} + \dot{\lambda} M^c_{klmn} e_{mn} \tag{3.42}$$

$$\mathfrak{m}^b_{kl} = \dot{\lambda} M^c_{mnkl} \epsilon_{mn} + \dot{\lambda} M^b_{klmn} e_{mn} \tag{3.43}$$

$$\mathfrak{m}^A_{klm} = \dot{\lambda} M^A_{lmknpq} \gamma_{npq} \ . \tag{3.44}$$

The different phases of the loading process are described by a *loading function* that can be expressed as $F(\epsilon_{kl}, \gamma_{klm}, e_{kl}, p^a_q, p^b_q, p^A_q)$, where p^a_q, p^b_q and p^A_q are vectors of internal variables that control the deformation process and function of the degrading strains $\dot{t}^d_{kl}$, $\dot{s}^d_{kl}$ and $\dot{m}^d_{klm}$, respectively. Hence, the following *consistency condition* holds

$$\dot{F} = \frac{\partial F}{\partial \epsilon_{kl}} \dot{\epsilon}_{kl} + \frac{\partial F}{\partial e_{kl}} \dot{e}_{kl} + \frac{\partial F}{\partial \gamma_{klm}} \dot{\gamma}_{klm} + \frac{\partial F}{\partial p^a_q} \dot{p}^a_q + \frac{\partial F}{\partial p^b_q} \dot{p}^b_q + \frac{\partial F}{\partial p^A_q} \dot{p}^A_q = 0 \tag{3.45}$$

with

$$\dot{p}^a_q = \frac{\partial p^a_q}{\partial \epsilon^d_{kl}} \dot{\epsilon}^d_{kl} \ , \quad \dot{p}^b_q = \frac{\partial p^b_q}{\partial e^d_{kl}} \dot{e}^d_{kl} \ , \quad \text{and} \quad \dot{p}^A_q = \frac{\partial p^A_q}{\partial \gamma^d_{klm}} \dot{\gamma}^d_{klm} \ . \tag{3.46a,b,c}$$

The directions of the loading function can be defined as

$$n^a_{kl} = \frac{\partial F}{\partial \epsilon_{kl}} \ , \quad n^b_{kl} = \frac{\partial F}{\partial e_{kl}} \ , \quad \text{and} \quad n^A_{klm} = \frac{\partial F}{\partial \gamma_{klm}} \tag{3.47a,b,c}$$

and the Hardening-Softening modulus H as

$$H = -\frac{\partial F}{\partial \lambda} = -\frac{\partial F}{\partial p^a_q} \frac{\partial p^a_q}{\partial \epsilon^d_{kl}} \mathfrak{m}^a_{kl} - \frac{\partial F}{\partial p^b_q} \frac{\partial p^b_q}{\partial e^d_{kl}} \mathfrak{m}^b_{kl} - \frac{\partial F}{\partial p^A_q} \frac{\partial p^A_q}{\partial \gamma^d_{klm}} \mathfrak{m}^A_{klm} \ . \tag{3.48}$$

Replacing Eqs. (3.47) and (3.48) into the consistency condition (Eq. 3.45) considering the definition of the degrading stresses presented in Eqs. (3.35)-(3.37), it can be obtained an expression for the inelastic multiplier

$$\dot{\lambda} = \frac{1}{H} \left(n^a_{pq} \dot{\epsilon}_{pq} + n^b_{pq} \dot{e}_{pq} + n^A_{pqn} \dot{\gamma}_{pqn} \right) \tag{3.49}$$

which, when introduced into Equations (3.29)-(3.31), leads to the following equations for the stress rate tensors

$$\dot{t}_{kl} = \left[A^S_{klpq} + \frac{1}{H}\mathfrak{m}^a_{kl} n^a_{pq}\right] \dot{\epsilon}_{pq} + \left[E^S_{klpq} + \frac{1}{H}\mathfrak{m}^a_{kl} n^b_{pq}\right] \dot{e}_{pq} + \frac{1}{H}\left(n^A_{pqn}\dot{\gamma}_{pqn}\right)\mathfrak{m}^a_{kl} \tag{3.50}$$

$$\dot{s}_{kl} = \left[E^S_{pqkl} + \frac{1}{H} n^a_{pq}\mathfrak{m}^b_{kl}\right] \dot{\epsilon}_{pq} + \left[B^S_{klpq} + \frac{1}{H} n^b_{pq}\mathfrak{m}^b_{kl}\right] \dot{e}_{pq} + \frac{1}{H}\left(n^A_{pqn}\dot{\gamma}_{pqn}\right)\mathfrak{m}^b_{kl} \tag{3.51}$$

$$\dot{m}_{klm} = \frac{1}{H}\left(n^a_{pq}\mathfrak{m}^A_{klm}\right)\dot{\epsilon}_{pq} + \left[C^S_{lmkpqn} + \frac{1}{H}(n^A_{pqn}\mathfrak{m}^A_{klm})\right]\dot{\gamma}_{pqn} + \frac{1}{H}\left(n^b_{pq}\mathfrak{m}^A_{klm}\right)\dot{e}_{pq} \tag{3.52}$$

3.3.1 Compact tensorial formulation

In a geometrically linear context, a classical elastic-degrading medium is characterized by total stress-strain relations

$$\sigma_{ij} = D^S_{ijkl}\varepsilon_{kl} \qquad \text{and} \qquad \varepsilon_{ij} = C^S_{ijkl}\sigma_{kl} \tag{3.53a,b}$$

where D^S_{ijkl} and C^S_{ijkl} are the components of the fourth-order stiffness and compliance secant tensors. On the other hand, as presented in the previous section, a micromorphic elastic-degrading medium is characterized by three stress-strain relations (see Eqs. (3.19), (3.20), and (3.21)) for a linear isotropic micromorphic material. To approach the consistency problem between a classical and a micromorphic theory, a compact tensorial formulation was proposed in Reges et al. (2023), which is here briefly recalled for stating the format of the generalized stiffness tensor obtained. In this formulation, the total stress-strain relation for a micromorphic media is written in a compact format as

$$\Sigma_{\beta\nu} = \mathcal{E}^S_{\beta\nu\delta\psi}\Gamma_{\delta\psi}, \text{ for } \beta, \nu, \delta, \psi = 1, 2, ...9 \tag{3.54}$$

where the *generalized stress operator* $\Sigma_{\beta\nu}$ and the *generalized strain operator* $\Gamma_{\delta\psi}$ represent second-order tensors with dimension nine. The *generalized secant stiffness operator* ${\mathcal{E}^S}_{\beta\nu\delta\psi}$ gathers the four constitutive operators of the micromorphic theory for isotropic linear elastic solids, i.e., $A_{klmn}, B_{klmn}, C_{klmnpq}$, and E_{klmn}, in a fourth-order tensor with dimension nine respecting the total stress-strain relations of such continuum.

Similarly, a *generalized compliance operator* ${\mathcal{C}^S}_{\beta\nu\delta\psi}$ and a generalized relation in terms of flexibility can be defined:

$$\Gamma_{\beta\nu} = \mathcal{C}^S_{\beta\nu\delta\psi}\Sigma_{\delta\psi}, \text{ for } \beta, \nu, \delta, \psi = 1, 2, ...9\,. \tag{3.55}$$

Considering a strain-based approach, the tangent stiffness tensor can then be obtained

$$\mathcal{E}^t_{\beta\nu\delta\psi} = \mathcal{E}^S_{\beta\nu\delta\psi} + \frac{1}{H} M_{\beta\nu\alpha\eta} \Gamma_{\alpha\eta} n_{\delta\psi} \tag{3.56}$$

where H is the Hardening-Softening modulus, $M_{\beta\nu\alpha\eta}$ defines the direction of the rate of change of ${\mathcal{E}^S}_{\beta\nu\delta\psi}$, and $n_{\beta\nu}$ indicates the directions of the loading functions.

This format was used in the computational implementation of elastic-degrading models for micromorphic media in the INSANE system (Reges et al., 2023). Therefore, the proper understanding of the formulation is important for correctly defining the acoustic tensors presented in Chapter 4 which required some manipulation of the generalized tangent operator to obtain the tangent constitutive operators separately.

3.3.2 Scalar-isotropic damage models for micromorphic media

For *scalar-isotropic* damage models, the degrading process is characterized by the progressive reduction of the secant stiffness tensor controlled by a single scalar *damage variable.*

Damage variables quantify the material deterioration in terms of continuous field variables. Physically, the damage variable is "defined by the surface density of microcracks and intersections of microvoids lying on a plane cutting the RVE of cross section δS" (Lemaitre and Desmorat (2005), p. 3). Hence, this density, for a plane with normal $\boldsymbol{n}$, is defined as

$$\mathscr{D}(\boldsymbol{n}) = \frac{\delta S_{\mathscr{D}}}{\delta S} \tag{3.57}$$

where $\delta S_{\mathscr{D}}$ is the area of the defects (microcracks and voids) contained in δS. The damage variable $D(\boldsymbol{n})$ goes from 0 for an undamaged material to 1 where the material is completely damaged. For a scalar-isotropic damage model, the variable $\mathscr{D}(\boldsymbol{n})$ does not depend on the normal and the intrinsic variable is a scalar (Kachanov, 1958, Lemaitre and Desmorat, 2005), i.e.,

$$\mathscr{D} = \frac{\delta S_{\mathscr{D}}}{\delta S} \; . \tag{3.58}$$

The progressive material degradation may be represented by the deterioration of its elastic properties. In this case, for a uniaxial state in a classical framework, the original Young's modulus is progressively degraded passing from an initial value E^0 to E^S that represents the modulus for the damaged material and evolves during the loading process (Fig. 3.9):

$$\mathscr{D} = 1 - \frac{E^S}{E^0} \tag{3.59}$$

or

$$E^S = (1 - \mathscr{D})E^0 \ . \tag{3.60}$$

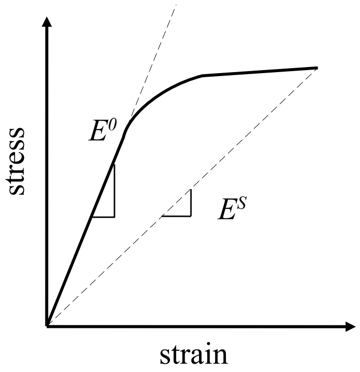

Figure 3.9: Elastic degradation

For a more general case, the process is represented by the degradation of the constitutive operator E^0_{ijkl} and the relation between the initial and current secant stiffness can be defined as

$$E^S_{ijkl} = (1 - \mathscr{D})E^0_{ijkl} \tag{3.61}$$

Such model is called an isotropic model since the damage variable impacts the whole initial constitutive operator E^0_{ijkl} and, therefore, does not compromise a possible isotropy of the tensor.

For cases wherein the hypotheses of a scalar damage variable is not sufficient to account for the damage dependence on the considered direction, tensorial damage variables may be used (e.g., vector, and second and fourth order tensors) (see Krajcinovic and Lemaitre (1987), Krajcinovic (1996), Lemaitre and Desmorat (2005)).

Therefore, the compact total stress-strain relation for a micromorphic continuum considering scalar-isotropic damage models, can be defined as

$$\Sigma_{\beta\nu} = (1 - \mathscr{D})\mathcal{E}^0{}_{\beta\nu\delta\psi}\Gamma_{\delta\psi} \tag{3.62}$$

wherein

$$\mathcal{E}^S_{\beta\nu\delta\psi} = (1 - \mathscr{D})\mathcal{E}^0{}_{\beta\nu\delta\psi} \ . \tag{3.63}$$

The tangent stiffness in Eq. (3.56) can be rewritten as

$$\mathcal{E}^{t}{}_{\beta\nu\delta\psi} = (1-\mathscr{D})\mathcal{E}^{0}{}_{\beta\nu\delta\psi} - \left(\frac{\partial\mathscr{D}(\Gamma_{eq})}{\partial\Gamma_{eq}}\right)\Sigma^{0}{}_{\beta\nu}\frac{\partial\Gamma_{eq}}{\partial\Gamma_{\delta\psi}}\,. \tag{3.64}$$

where $\mathscr{D}(\Gamma_{eq})$ is a damage law that describes the evolution of the damage variable, Γ_{eq} is defined as the generalized equivalent strain and $\Sigma^{0}{}_{\beta\nu} = \mathcal{E}^{0}{}_{\beta\nu\delta\psi}\Gamma_{\delta\psi}$.

Applying the general formulation proposed, different damage models for the micromorphic continuum can be obtained when specific equivalent strain measures are defined. The classic damage models of *Mazars-Lemaitre* (Mazars and Lemaitre, 1985), *Simo-Ju* (Simo and Ju, 1987), *Ju* (Ju, 1989), and *Marigo* (Marigo, 1985) are extended to the micromorphic continuum adopting the following equivalent strains (Reges et al., 2023):

$$\Gamma_{eq} = \begin{cases} \sqrt{\epsilon_{mn}\epsilon_{mn} + e_{mn}e_{mn}} & \text{(Mazars-Lemaitre micromorphic model)} \\ \sqrt{2\psi^{0}} & \text{(Simo-Ju micromorphic model)} \\ \psi^{0} & \text{(Ju micromorphic model)} \\ \sqrt{\frac{2\psi^{0}}{E}} & \text{(Marigo micromorphic model)} \end{cases} \tag{3.65}$$

in which $\psi^{0} = \frac{1}{2}A^{0}{}_{klmn}\epsilon_{kl}\epsilon_{mn} + \frac{1}{2}B^{0}{}_{klmn}e_{kl}e_{mn} + \frac{1}{2}C^{0}{}_{klmnpq}\gamma_{klm}\gamma_{npq} + E^{0}{}_{klmn}\epsilon_{kl}e_{mn}$, with $A^{0}{}_{klmn}$, $B^{0}{}_{klmn}$, $C^{0}{}_{klmnpq}$, and $E^{0}{}_{klmn}$ being the initial elastic operators, and E is the material Young's modulus used to construct an equivalent micromorphic continuum through the homogenization technique. As previously discussed, for the micromorphic continuum, there are 18 elastic parameters where there is no equivalence between one of the parameters and the Young's modulus of a classical continuum. Hence, in this work the Marigo model is only applied associated to the homogenization technique, where E is clearly defined.

Chapter 4

Discontinuous failure in micromorphic elastic-degrading media

This chapter focuses on the study of discontinuous failure in micromorphic media. It introduces the formulation of the micromorphic acoustic tensor using both macroscale and microscale approaches and presents numerical investigations that analyze their behavior.

4.1 Initial concepts

Deformation and failure are typically developed at multiple scales for the majority of engineering materials. At the macroscopic level of observation, structural rupture is triggered by a localized failure that corresponds to a loss in the material continuity within a specific region of the body. This localized failure is preceded by microcrack coalescence that can be observed at lower observation levels.

Failure conditions and failure modes at the material level, i.e., in a pointwise sense, have been extensively studied in terms of a *localization analysis* in which discontinuous failure initiates when the second order localization tensor or its symmetric counterpart is singular (Rizzi et al., 1996).

The necessary conditions for localization can be determined building upon the work of Hadamard (1903) and Hill (1958) and have been explored in the literature for plasticity Rudnicki and Rice (1975), Ottosen and Runesson (1991) and damage Rizzi et al. (1995). Discontinuous failure is associated to the singularity of the localization or *acoustic tensor*, which results, in a classical medium, by contracting the tangent stiffness tensor D^t_{ijkl} with the normal vector $\boldsymbol{n}$ associated to an eventual localization

$$Q_{jk} = n_i D^t_{ijkl} n_l \ . \tag{4.1}$$

Strain localization is then a discontinuous phenomenon related to the formation of jumps in the field variables across a singularity surface and identified, within the classical theory, when

$$det(Q_{jk}) = 0 \, . \tag{4.2}$$

As pointed out by Jirásek (2007), the singularity of the acoustic tensor is a necessary condition but not sufficient to determine whether the discontinuity develops. The surrounding material and the boundary conditions should be included in the analysis. Nevertheless, the analysis of the localization tensor is an important indicator of potential discontinuous failure and be applied in order to detect the onset of localization and discontinuities (Massart et al., 2007*a*,*b*).

Concerning generalized theories, the contributions in the field are more limited, specially concerning the micromorphic theory. An important contribution identified by the author includes the definition of the acoustic tensor for the nonlinear micromorphic medium by Eremeyev et al. (2018) drawing on the theory of acceleration waves. Other important works concerning the definition of an acoustic tensor and the localization analysis in micropolar media are Eremeyev (2005) and Gori et al. (2018).

Taking into account the contributions mentioned, it is proposed in this chapter an extension of the discontinuous failure concepts to elastic-degrading micromorphic media and the evaluation of a proper localization criterion for identifying the introduction of a discontinuity. Once the tangent stiffness operator for elastic-degrading micromorphic media is established in Section 3.3, failure at the constitutive level may be analyzed.

Considering the non-local formulation of the micromorphic theory in which kinematics is constructed based on macroscale and microscale variables, two approaches for the localization analysis are here proposed: one regarding the *macroscale* and the other related to the *miscroscale*. The motivation for such separation lies on the regularization capacity of the micromorphic theory that could lead to an acoustic tensor that does not indicate strain localization. As this work builds upon the localization analysis to determine whether a discontinuity should be inserted via the XFEM approach, this study aimed to establish a robust criterion for identification of onset of discontinuous failure in micromorphic media, contributing to advancements in the comprehension of this generalized theory regarding damage and failure.

4.1.1 Macroscale discontinuity

Let one consider discontinuous deformations on a singular surface $S(t)$, as represented in Fig. 4.1, where $\boldsymbol{n}$ is a unit vector normal to the singular surface and v is the local speed of propagation. As pointed out by Eremeyev et al. (2018), S is a non-material surface propagating across material points function of time t.

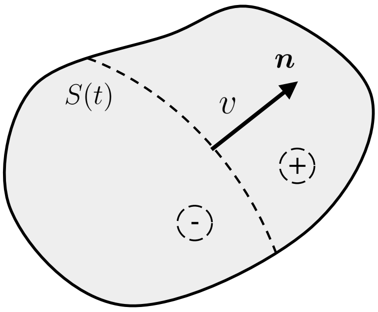

Figure 4.1: Body split by a potential discontinuity surface

If $v \neq 0$, the surface propagates and is therefore called a *wave.* An *acceleration wave* (or weak discontinuity) in a micromorphic medium within small deformations is considered to be a singular surface on which the second spatial and second time derivatives of $\boldsymbol{u}$ and $\boldsymbol{\phi}$ have jumps, while $\boldsymbol{u}$ and $\boldsymbol{\phi}$ together with their first derivatives are continuous (Truesdell and Noll, 2004, Eremeyev et al., 2018). Therefore, such a wave must carry a jump of the acceleration, hence the term acceleration wave.

The discontinuity $S(t)$ divides the body into two subdomains, + and −, and its orientation is characterized by a unit vector $\boldsymbol{n}$. As a point in the singular surface is approached from either side, the fields that exhibit discontinuity across $S(t)$ tend to different limits. These limits are denoted with superscripts $^+$ and $^-$, respectively. The difference between them, i.e., $[\![a]\!] = a^+ - a^-$, corresponds to the jump in the considered variable a across the wavefront. Therefore, the following conditions hold regarding the continuous quantities

$$[\![u_i]\!] = 0, \quad [\![\phi_{ij}]\!] = 0 \tag{4.3a,b}$$

$$[\![u_{i,j}]\!] = 0, \quad [\![\phi_{ij,k}]\!] = 0 \tag{4.4a,b}$$

$$[\![\dot{u}_i]\!] = \left[\!\!\left[\frac{\partial u_i}{\partial t}\right]\!\!\right] = 0, \quad [\![\dot{\phi}_{ij}]\!] = \left[\!\!\left[\frac{\partial \phi_{ij}}{\partial t}\right]\!\!\right] = 0 \tag{4.5a,b}$$

and the non-continuous

$$[\![\dot{u}_{i,j}]\!] = \left[\!\!\left[\frac{\partial u_{i,j}}{\partial t}\right]\!\!\right] \neq 0, \quad [\![\dot{\phi}_{ij,k}]\!] = \left[\!\!\left[\frac{\partial \phi_{ij,k}}{\partial t}\right]\!\!\right] \neq 0 \tag{4.6}$$

$$[\![\ddot{u}_i]\!] = \left[\!\!\left[\frac{\partial^2 u_i}{\partial t^2}\right]\!\!\right] \neq 0, \quad [\![\ddot{\phi}_{ij}]\!] = \left[\!\!\left[\frac{\partial^2 \phi_{ij}}{\partial t^2}\right]\!\!\right] \neq 0 \tag{4.7}$$

wherein the overdot stands for the time derivative. Applying Maxwell's theorem (Truesdell and Noll, 2004) to the continuous fields $[\![\dot{u}_i]\!]$ and $[\![\dot{\phi}_{ij}]\!]$, the following relations hold

$$[\![\dot{u}_{i,j}]\!] = a_i n_j \quad \text{and} \quad [\![\dot{\phi}_{ij,k}]\!] = A_{ij} n_k, \tag{4.8a,b}$$

where a_i and A_{ij} are the vectorial and second-order tensorial amplitudes of the jumps.

Considering the strain measure defined as $\epsilon_{ij} = u_{i,j} - \phi_{ij}$ in Eq. (3.12a), and the expressions in Eqs. (4.5b) and (4.8a), the jump in the time derivative $\dot{\epsilon}_{kl}$ can be written as

$$[\![\dot{\epsilon}_{ij}]\!] = [\![\dot{u}_{i,j}]\!] = a_i n_j \tag{4.9a}$$

$$\dot{\epsilon}^{+}_{ij} = \dot{\epsilon}^{-}_{ij} + a_i n_j \ . \tag{4.9b}$$

Regarding the second strain measure $2e_{ij} = \phi_{ij} - \phi_{ji}$ (Eq. (3.12b)) and observing Eq. (4.5b),

$$[\![\dot{e}_{ij}]\!] = 0 \tag{4.10a}$$

$$\dot{e}^{+}_{ij} = \dot{e}^{-}_{ij} \ . \tag{4.10b}$$

Lastly, the time derivative of the strain measure $\gamma_{ijk} = \phi_{ij,m}$ (Eq. (3.12c)), considering Eq. (4.8b), can be written as

$$[\![\dot{\gamma}_{ijk}]\!] = A_{ij} n_k \tag{4.11a}$$

$$\dot{\gamma}^{+}_{ijk} = \dot{\gamma}^{-}_{ijk} + A_{ij} n_k \ . \tag{4.11b}$$

Therefore, in the macroscale approach, only the strain tensors ϵ_{ij} and γ_{ijk} have jumps while e_{ij} remains continuous. The jump in the stress rate tensors $[[\dot{\boldsymbol{t}}]]$ and $[[\dot{\boldsymbol{m}}]]$ energetically related to the strain measures ϵ_{kl} and γ_{lmk} (see Eqs. 3.15 and 3.17) are considered to be constrained by the *traction continuity* condition (Rizzi et al., 1996, Jirásek, 2007). This condition implies that only the in-plane stress rates (with respect to the plane tangent to the discontinuity surface) can be discontinuous. This condition in the macroscale approach can be written as

$$n_k \dot{t}^+_{kl} = n_k \dot{t}^-_{kl} \tag{4.12}$$

$$n_k \dot{m}^+_{klm} = n_k \dot{m}^-_{klm} \; . \tag{4.13}$$

Considering initially the hypothesis of undamaged material and that the constitutive operators can be different on both sides of the discontinuity surface, the time derivative of the stress-strain equations, observing Eqs. (3.19) and (3.21), can be written as

$$\dot{t}^+_{kl} = A^{0+}_{klmn} \dot{\epsilon}^+_{mn} + E^{0+}_{klmn} \dot{e}^+_{mn} \tag{4.14a}$$

$$\dot{t}^-_{kl} = A^{0-}_{klmn} \dot{\epsilon}^-_{mn} + E^{0-}_{klmn} \dot{e}^-_{mn} \tag{4.14b}$$

$$\dot{m}^+_{klm} = C^{0+}_{lmknpq} \dot{\gamma}^+_{npq} \tag{4.15a}$$

$$\dot{m}^-_{klm} = C^{0-}_{lmknpq} \dot{\gamma}^-_{npq} \tag{4.15b}$$

where A^0_{klmn}, E^0_{klmn}, and C^0_{lmknpq} are the initial constitutive operators. Substituting Eqs. (4.14) and (4.15) into the condition expressed in Eqs. (4.12) and (4.13) leads to

$$n_k A^{0+}_{klmn} \dot{\epsilon}^+_{mn} + n_k E^{0+}_{klmn} \dot{e}^+_{mn} = n_k A^{0-}_{klmn} \dot{\epsilon}^-_{mn} + n_k E^{0-}_{klmn} \dot{e}^-_{mn} \tag{4.16}$$

$$n_k C^{0+}_{lmknpq} \dot{\gamma}^+_{npq} = n_k C^{0-}_{lmknpq} \dot{\gamma}^-_{npq} \; . \tag{4.17}$$

Introducing the jump in the strain rate tensors defined in Eqs. (4.9) and (4.11)

$$n_k A^{0+}_{klmn} \dot{\epsilon}^-_{mn} + n_k A^{0+}_{klmn} a_m n_n + n_k E^{0+}_{klmn} \dot{e}^+_{mn} = n_k A^{0-}_{klmn} \dot{\epsilon}^-_{mn} + n_k E^{0-}_{klmn} \dot{e}^-_{mn} \tag{4.18}$$

$$n_k C^{0+}_{lmknpq} \dot{\gamma}^-_{npq} + n_k C^{0+}_{lmknpq} A_{np} n_q = n_k C^{0-}_{lmknpq} \dot{\gamma}^-_{npq} \tag{4.19}$$

This is a general equation for describing an incipient discontinuity and can be considerably simplified considering that the constitutive operators are the same on both sides of the discontinuity ($\boldsymbol{A}^+ = \boldsymbol{A}^- = \boldsymbol{A}$, $\boldsymbol{C}^+ = \boldsymbol{C}^- = \boldsymbol{C}$, and $\boldsymbol{E}^+ = \boldsymbol{E}^- = \boldsymbol{E}$). Therefore, Eqs. (4.18) and (4.19) can be rewritten as

$$Q^a_{lm} a_m = 0 \tag{4.20}$$

$$Q^A_{lmnp} A_{np} = 0 \tag{4.21}$$

where

$$Q^a_{lm} := A^0_{klmn} n_n n_k \tag{4.22a}$$
$$Q^A_{lmnp} := C^0_{lmknpq} n_q n_k \tag{4.22b}$$

are the *macroscale initial acoustic tensors* associated to the initial constitutive operators $\boldsymbol{A}$ and $\boldsymbol{C}$, respectively. The name acoustic is due to the fact that, for a classical continuum, if the tangent constitutive operators are taken as the elastic tensors, their eigenvalues divided by the mass density are squares of the speeds of elastic waves propagating in the direction $\boldsymbol{n}$. Then, the corresponding eigenvectors are polarization vectors that determine the type of waves (longitudinal, transversal, mixed) (Jirásek, 2007). For the case of the micromorphic continuum, similar results are presented by Eremeyev et al. (2018) in which Eqs. (4.20) and (4.21) are written as

$$Q^a_{lm} a_m := \rho v^2 a_l \tag{4.23}$$

$$Q^A_{lmnp} A_{np} := j v^2 A_{lm} \tag{4.24}$$

where ρ is the mass density in the reference configuration; $j \geq 0$ is the scalar measure of microinertia; v is the speed of propagation of the singular surface (Fig. 4.1).

On the other hand, if a *damaging wave* is considered instead of an elastic one, both sides of the discontinuity are supposed to be in a damaged state[1] [2]. Considering the rate equations for a micromorphic elastic-degrading medium (see Eqs. (3.50) and 3.52), it may be stated

---

[1] A more complex scenario could involve a mixed damaged-undamaged state in the constitutive relations. However, this condition is not considered due to the assumption of a single loading function, which ensures that all constitutive tensors transition into a damaged state simultaneously.

[2] In this study, the degradation evolution is assumed to be identical on both sides of the discontinuity surface. Consequently, cases involving loading and unloading waves—where one side of the discontinuity is in a damaged state while the other remains elastic—are not considered. While this assumption has been explored in classical media (see, e.g., Jirásek (2007)), further investigation is needed for micromorphic media.

$$\left\{\left[A^S_{klpq} + \frac{1}{H}\boldsymbol{\mathfrak{m}}^a_{kl} n^a_{pq}\right] a_p n_q + \frac{1}{H}\left(n^A_{pqn}\boldsymbol{\mathfrak{m}}^a_{kl}\right) A_{pq} n_n\right\} n_k = 0 \tag{4.25a}$$

$$\left\{\frac{1}{H}\left(n^a_{pq}\boldsymbol{\mathfrak{m}}^A_{klm}\right) a_p n_q + \left[C^S_{lmkpqn} + \frac{1}{H}(n^A_{pqn}\boldsymbol{\mathfrak{m}}^A_{klm})\right] A_{pq} n_n\right\} n_k = 0\ . \tag{4.25b}$$

The *tangent acoustic tensors* are then defined

$$Q^{t,aa}_{lp} := Q^{S,aa}_{lp} + \frac{1}{H}\boldsymbol{\mathfrak{m}}^a_{kl} n^a_{pq} n_q n_k \tag{4.26a}$$

$$Q^{t,aA}_{pql} := \frac{1}{H} n^A_{pqn} n_n \boldsymbol{\mathfrak{m}}^a_{kl} n_k \tag{4.26b}$$

$$Q^{t,AA}_{lmpq} := Q^{S,AA}_{lmpq} + \frac{1}{H} n^A_{pqn} n_n \boldsymbol{\mathfrak{m}}^A_{klm} n_k \tag{4.26c}$$

$$Q^{t_A a}_{plm} := \frac{1}{H} n^a_{pq} n_q \boldsymbol{\mathfrak{m}}^A_{klm} n_k \tag{4.26d}$$

where the *secant acoustic tensors* have been introduced

$$Q^{S,aa}_{lp} := A^S_{klpq} n_q n_k \tag{4.27a}$$

$$Q^{S,AA}_{lmpq} := C^S_{lmkpqn} n_n n_k \tag{4.27b}$$

The expressions in Eq. (4.25) can be rewritten in terms of the tangent acoustic tensors

$$Q^{t,aa}_{lp} a_p + Q^{t,aA}_{pql} A_{pq} = 0 \tag{4.28a}$$

$$Q^{t,Aa}_{plm} a_p + Q^{t,AA}_{lmpq} A_{pq} = 0 \tag{4.28b}$$

that may be arranged in matrix form (Eremeyev et al., 2018)

$$\mathcal{Q}^t \cdot \boldsymbol{\xi} = 0 \tag{4.29}$$

where $\mathcal{Q}$ is the *macroscale generalized acoustic tensor*, being defined as followed as well as $\boldsymbol{\xi}$

$$\mathcal{Q}^t := \begin{bmatrix} Q^{t,aa}_{lp} & Q^{t,aA}_{pql} \\ Q^{t,Aa}_{plm} & Q^{t,AA}_{lmpq} \end{bmatrix} \quad \text{and} \quad \boldsymbol{\xi} := \begin{bmatrix} a_p \\ A_{pq} \end{bmatrix}\ . \tag{4.30}$$

4.1.2 Microscale discontinuity

Similarly, the condition for the onset of localization from a *microscale perspective* can be determined considering now the hypothesis of a discontinuity related only to the strain field e_{ij}. As stated in Equation (3.12c), this strain measure only relates to the micromotion gradient field ϕ_{ij} which describes the state of the material particle. Therefore, recalling Fig. 4.1, it holds

$$[\![\dot{\epsilon}_{ij}]\!] = 0 \ , \quad [\![\dot{e}_{ij}]\!] = b_i n_j \ , \quad \text{and} \quad [\![\dot{\gamma}_{ijk}]\!] = 0 \tag{4.31a,b,c}$$

where b_i is the vectorial amplitude of the jump and n_j is a unit vector normal to the singular surface.

Similarly, the traction continuity condition holds for the stress rate jump $[[\dot{\boldsymbol{s}}]]$ (Eq. 3.16)

$$n_k \dot{s}^+_{kl} = n_k \dot{s}^-_{kl} \tag{4.32}$$

and, considering that the strain tensor e_{kl} is defined as the symmetric part of the micromotion gradient tensor ϕ_{kl} (Eq. (3.12b)), it holds

$$\dot{e}^+_{kl} = \dot{e}^-_{kl} + \frac{1}{2}(b_k n_l + b_l n_k) \ . \tag{4.33}$$

Observing that the constitutive tensors can be different on both sides of the discontinuity, the time derivative of the stress-strain equation (Eq. 3.20) can be written as

$$\dot{s}^+_{kl} = E^{0+}_{mnkl}\dot{\epsilon}^+_{mn} + B^{0+}_{klmn}\dot{e}^+_{mn} \qquad \text{and} \qquad \dot{s}^-_{kl} = E^{0-}_{mnkl}\dot{\epsilon}^-_{mn} + B^{0-}_{klmn}\dot{e}^-_{mn} \tag{4.34a,b}$$

leading to

$$n_k E^{0+}_{mnkl}\dot{\epsilon}^+_{mn} + n_k B^{0+}_{klmn}\dot{e}^+_{mn} = n_k E^{0-}_{mnkl}\dot{\epsilon}^-_{mn} + n_k B^{0-}_{klmn}\dot{e}^-_{mn} \ . \tag{4.35}$$

Applying Eqs. (4.31) and (4.33) , and exploiting the symmetry of the tensor B_{klmn} (Eq. 3.14))

$$n_k E^{0+}_{mnkl}\dot{\epsilon}^{+}_{mn} + n_k B^{0+}_{klmn}\dot{e}^{-}_{mn} + n_k B^{0+}_{klmn} b_m n_n = n_k E^{0-}_{mnkl}\dot{\epsilon}^{-}_{mn} + n_k B^{0-}_{klmn}\dot{e}^{-}_{mn} \tag{4.36}$$

which can be simplified considering that the constitutive tensors are the same on both sides of the discontinuity ($\boldsymbol{B}^{+} = \boldsymbol{B}^{-} = \boldsymbol{B}$ and $\boldsymbol{E}^{+} = \boldsymbol{E}^{-} = \boldsymbol{E}$)

$$n_k B^{0+}_{klmn} b_m n_n = 0 \tag{4.37}$$

where

$$Q^{b}_{lm} := B^{0}_{klmn} n_n n_k \tag{4.38}$$

is called the *microscale initial acoustic tensor* for the micromorphic continuum.

Regarding a damaging wave and considering the expression for the stress rate tensor stated in Eq.(3.51), it can be written

$$\left[B^{S}_{klpq} + \frac{1}{H} n^{b}_{pq} \mathfrak{m}^{b}_{kl} \right] b_p n_q n_k = 0 \tag{4.39}$$

which leads to the definition of the *microscale tangent acoustic tensor*

$$Q^{t,b}_{lp} := Q^{S,b}_{lp} + \frac{1}{H} \mathfrak{m}^{b}_{kl} n^{b}_{pq} n_q n_k \tag{4.40}$$

where the *microscale secant acoustic tensor* has been introduced

$$Q^{S,b}_{lp} := B^{S}_{klpq} n_q n_k \ . \tag{4.41}$$

4.2 Localization analysis

From Eqs. (4.29) and (4.40), considering that, for a potential weak discontinuity, the localization tensor is singular, the *macroscale localization condition* is defined

$$\det(\mathcal{Q}^{t}) = 0 \tag{4.42}$$

as well as the *microscale localization condition*

$$det(\boldsymbol{Q}^{t,b}) = 0\,. \tag{4.43}$$

Considering the macroscale analysis, two special cases can also be derived considering: (i) a discontinuity only in the displacement u_i ($\llbracket \ddot{u}_i \rrbracket \neq 0$ and $\llbracket \ddot{\phi}_{ij} \rrbracket = 0$), and (ii) only in the micromotion gradient ϕ_{ij} ($\llbracket \ddot{u}_i \rrbracket = 0$ and $\llbracket \ddot{\phi}_{ij} \rrbracket \neq 0$). Focusing on the first special case, Eq. (4.28) is stated as

$$Q^{t,aa}_{lp} a_p = \rho v^2 a_l \quad \therefore \quad Q^{S,aa}_{lp} a_p + \frac{1}{H}(\mathfrak{m}^{a}_{kl} n_k)(n^{a}_{pq} n_q) a_p = \rho v^2 a_l \tag{4.44a}$$

$$Q^{t,Aa}_{plm} a_p = 0 \quad \therefore \quad \frac{1}{H}(n^{a}_{pq} n_q)(\mathfrak{m}^{A}_{klm} n_k) a_p = 0 \tag{4.44b}$$

These conditions, as presented for the micropolar continuum in Gori et al. (2018), can be reduced to

$$Q^{t,aa}_{lp} a_p = 0\ . \tag{4.45}$$

The same consideration apply for the micromotion gradient field ϕ_{ij}, and a non-trivial solution is possible for cases (i) and (ii) presented, respectively, if

$$\text{(i) } \det\left(Q^{t,aa}_{lp}\right) = 0 \quad \text{and} \quad \text{(ii) } \det\left(Q^{t,AA}_{lmpq}\right) = 0 \tag{4.46a,b}$$

The conditions here presented, when met, indicate loss of *ellipticity* of the governing differential equation and correspond to a weak localization condition. The boundary value problems become *ill-posed* as there is not only one unique solution. This problem can be manifested numerically by mesh sensitivity of the results. For a strong localization condition, the symmetric part of the acoustic tensor should be analyzed. Is is worth noting that, for the case of associated scalar-isotropic damage models, the condition for a weak and a strong discontinuity coincide (Neilsen and Schreyer, 1993).

The acoustic tensor defined in Eq. (4.1) depends on the tangent stiffness tensor $\boldsymbol{D}$ and on the unit normal to the discontinuity surface $\boldsymbol{n}$. The stiffness, in most cases, depends only on the current state and is known. The normal vector, however, is not given in advance. Therefore, localization analysis consists in searching for a unit vector for which the tensor is singular. If this condition is met, a strain jump can develop across a surface with normal $\boldsymbol{n}$, otherwise the strain field remains continuous.

Therefore, the macroscale and microscale localization analysis are investigated in this study as a threshold for the introduction of a discrete failure.

4.3 Numerical simulations

The present section is dedicated to the investigation of the behavior of the micromorphic acoustic tensor on the onset of expected localization based on the derivations presented in the previous section for the macro and micro scales approaches.

To perform the localization analysis, a numerical technique based on a Cartesian parametrization was employed to determine the orientation $\boldsymbol{n}$ at which the classical and micromorphic acoustic tensors become singular. This approach, originally proposed by Mota et al. (2016), was later implemented in the INSANE system for classical continua, as detailed in Fioresi et al. (2020). In this method, the normal vector corresponding to the singular acoustic tensor is not constrained to be unitary. Instead, the search space is defined within a cube centered at the origin with a side length of two.

In the context of a nonlinear analysis, localization is assessed at the material level for the integration point after the convergence of each step, where the constitutive model framework provides the necessary tangent constitutive operator for this investigation. The analysis is formulated as a numerical optimization problem. If the determinant of the acoustic tensor is less than or equal to zero, localization is identified. Otherwise, the next face of the cube is examined until all three faces are assessed. The reader is referred to Fioresi et al. (2020) for more details on the numerical approach.

Two numerical simulations are presented in this section: a uniaxial stress state and an L-shaped panel. The first simulation aimed to investigate the localization phenomenon in a micromorphic medium, considering both macroscale and microscale approaches, and comparing the results with those obtained from a classical continuum analysis. Building on these findings, the second simulation examined the L-shaped panel to assess the effectiveness of the microscale acoustic tensor in detecting localization within the micromorphic continuum.

4.3.1 Uniaxial stress state

Initially, a uniaxial stress state is investigated. Fig. 4.2 illustrates the adopted model analyzed under plane stress conditions. The 3×1 m^2 panel is discretized with three 4-node quadrilateral elements with four integration points and subjected to a traction load q. The model is simulated considering both classical and micromorphic theories.

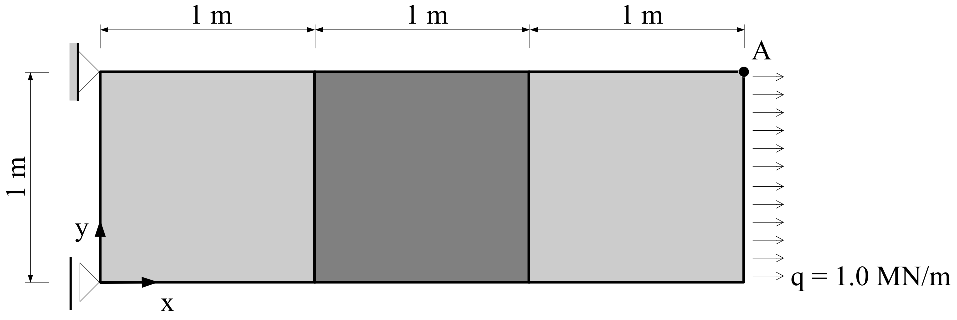

Figure 4.2: Uniaxial stress state: geometry

For the classical analysis, the constitutive models proposed by Simo-Ju (Simo and Ju, 1987), Ju (Ju, 1989), Marigo (Marigo, 1985), and Mazars-Lemaitre (Mazars and Lemaitre, 1985) are employed associated to a Young's modulus $E = 20000$ MPa and a Poisson's ratio $\nu = 0.2$. For the micromorphic continuum, the generalized models presented in Eq. (3.65) are used considering the same Young's modulus ($E = 20000$ MPa) and Poisson's ratio ($\nu = 0.2$). The adoption of the classical constants for both analysis is made possible by a homogenization technique (Silva et al., 2022) which considered, for this example, a square microcontinuum with 0.5 m to obtain the micromorphic constitutive equations.

The appropriated parameters for each constitutive model were adopted considering an exponential damage law described by

$$\mathscr{D}(\Gamma_{eq}) = 1 - \frac{K_0}{\Gamma_{eq}} \left(1 - \alpha + \alpha e^{-\beta(\Gamma_{eq} - K_0)}\right) \tag{4.47}$$

in which K_0 is the threshold for the equivalent strain, α and β define the maximum damage level allowed and the damage evolution intensity, respectively, and Γ_{eq} is the generalized equivalent strain (see Eq. (3.65)). The central element, highlighted in Fig. 4.2, was considered to be less resistant and associated to material M2 while the two other elements were associated to material M1. The parameters adopted for M1 and M2 considered in the classical and the micromorphic analysis are detailed in Table 4.1 for each damage model.

Table 4.1: Uniaxial stress state: constitutive parameters

Constitutive model	Parameters
Simo-Ju	M1: $\alpha = 0.999$; $\beta = 30.0$; $K_0 = 0.0148$
	M2: $\alpha = 0.999$; $\beta = 30.0$; $K_0 = 0.0133$
Ju	M1: $\alpha = 0.999$; $\beta = 15.0$; $K_0 = 0.00011$
	M2: $\alpha = 0.999$; $\beta = 15.0$; $K_0 = 0.000099$
Marigo	M1: $\alpha = 0.99$; $\beta = 4000.0$; $K_0 = 0.0001049$
	M2: $\alpha = 0.99$; $\beta = 4000.0$; $K_0 = 0.000094$
Mazars-Lemaitre	M1: $\alpha = 0.99$; $\beta = 4000.0$; $K_0 = 0.0001049$
	M2: $\alpha = 0.99$; $\beta = 4000.0$; $K_0 = 0.000094$

The loading process is driven by the displacement control method assuming an increment of 1×10^{-5} m for the horizontal displacement of node A (see Fig. 4.2), and a tolerance for the convergence of 10^{-4} in displacements.

Figure 4.3 presents the results for the analysis wherein the relation between the horizontal displacement for node A (Fig. 4.2) and the load factor q is given. Steps highlighted with an mark "X" indicate the first detection of strain localization. For the classical continuum, simulations with models Simo-Ju and Marigo displayed localization after the peak for step 29 and with the Mazars-Lemaitre model for step 28. For the Ju model, the simulation presented numerical instabilities as soon as damage initiated due to the strain localization.

The micromorphic continuum, as it can be seen in the obtained equilibrium paths illustrated in Fig. 4.3(b), presents some differences when compared to the classical analysis. For the micromorphic analysis the peak load is higher and the post-peak branch is not directly correlated to the exponential damage law adopted as it can be observed for the classical analysis. Furthermore, there were no numerical instabilities for any of the damage models employed.

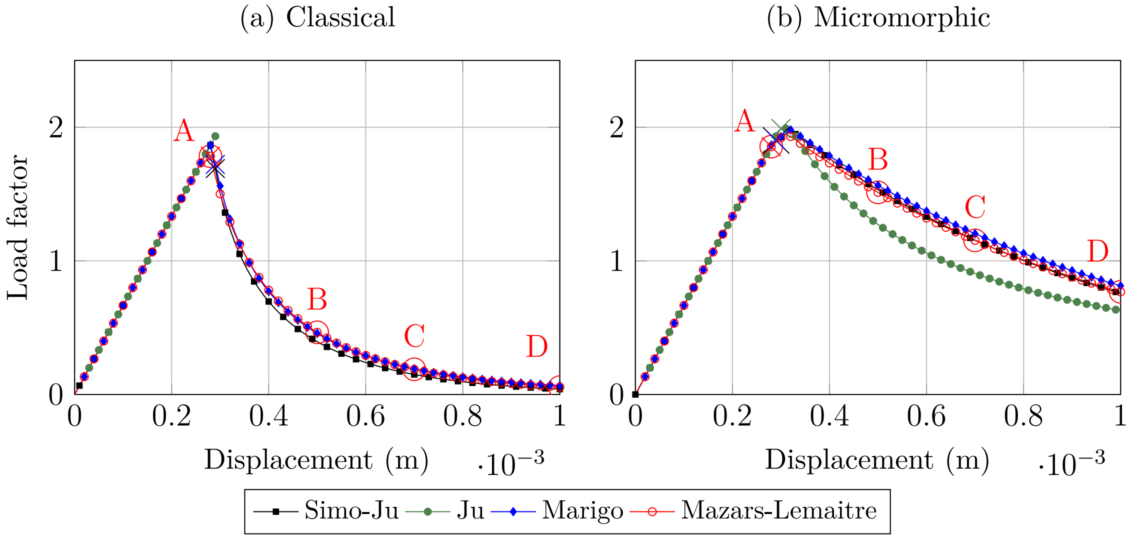

Figure 4.3: Uniaxial stress state: load factor versus horizontal displacement

In order to study the behavior of the acoustic tensor in a micromorphic medium, two approaches are used, both considering the first integration point of the weakened element. First, the acoustic tensor determinant is calculated for different normal directions $\boldsymbol{n}$ adopting a sweep procedure. Second, the minimum value of the acoustic tensor is found throughout the nonlinear process applying the Cartesian parametrization detailed in the introduction of this section.

Regarding initially the sweep procedure, the normal vector is described in terms of the angle θ measured clockwise from the vertical direction considering an analysis in the $x-y$ plane. Angles ranging from 0 to 180 degrees were investigated considering a 5 degrees step. The results for $\det(\boldsymbol{Q})/\max[\det(\boldsymbol{Q})]$ versus θ in different steps in the nonlinear analysis are presented in Fig. 4.4 considering the Mazars-Lemaitre damage model. Five stages in the analysis were considered: the elastic branch and points A to D marked in the equilibrium paths (Fig. 4.3).

(a) Classical (b) Micromorphic ($\boldsymbol{Q}^{t,b}$)

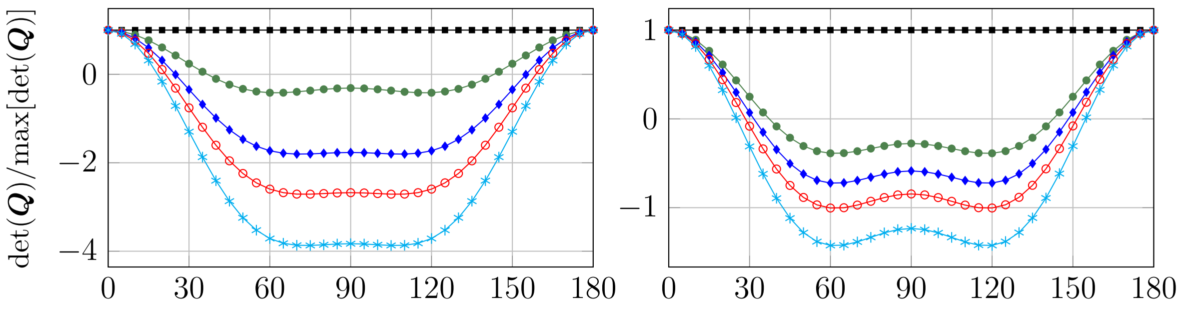

(c) Micromorphic ($\boldsymbol{Q}^{t,aa}$) (d) Micromorphic ($\boldsymbol{Q}^{t,AA}$)

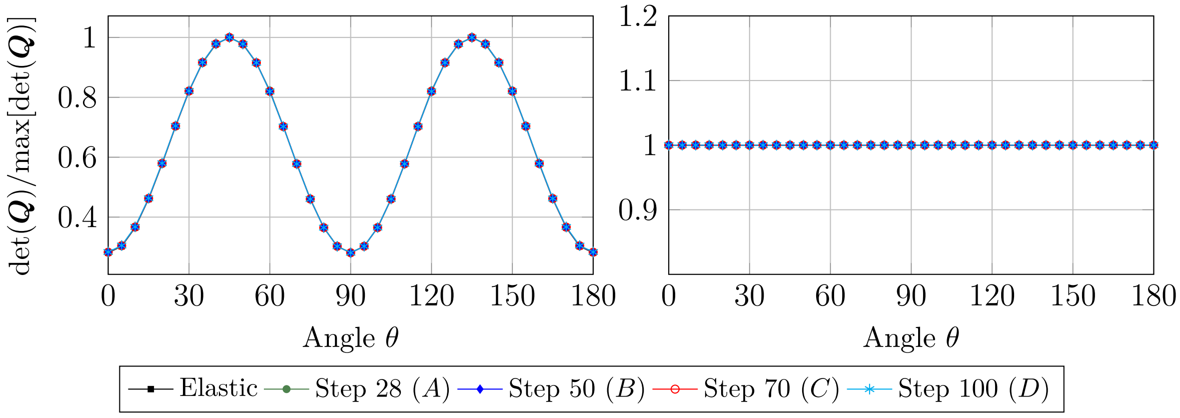

Figure 4.4: Uniaxial stress state: $\det(\boldsymbol{Q})$ for different angles

Regarding a macroscale localization analysis in which the macroscale acoustic tensors $\boldsymbol{Q}^{t,aa}$ and $\boldsymbol{Q}^{t,AA}$ (see Eq. (4.46)) are considered, it can be noticed that the tensors do not become singular or experience change (see Figs. 4.4(c) and 4.4(d)), as for the classical continuum. Therefore, the macroscale acoustic tensors are not able to indicate neither the introduction of a discontinuity nor its direction. These results reflect the known regularization properties of generalized theories due to their non-local formulation.

On the other hand, the overall behavior for the microscale micromorphic acoustic tensor (Fig. 4.4(b)) is similar for the classical acoustic tensor (Fig. 4.4(a)), where the determinant becomes negative for step 28, indicating the localization phenomenon.

Considering the second study, the results for the minimum value computed for the determinant of the considered acoustic tensor $\boldsymbol{Q}$ at each step of the nonlinear analysis for the four damage models considered is presented in Fig. 4.5. During elastic loading, the determinant remains constant for classical and micromorphic continuum. However, once damage initiates, the determinant in the classical and microscale analyses becomes negative, indicating localization. In contrast, for the macroscale micromorphic analysis, the determinant experiences a sharp decrease but remains positive throughout the loading process.

It is important to note that the acoustic tensor $\boldsymbol{Q}^{t,AA}$ was not included in this analysis. As presented in Fioresi et al. (2020), the numerical technique applied requires that the equation for the determinant is given explicitly. The higher-order nature of this tensor (fourth order) results in a complicated function that would be computationally challenging to implement, making its consideration impractical.

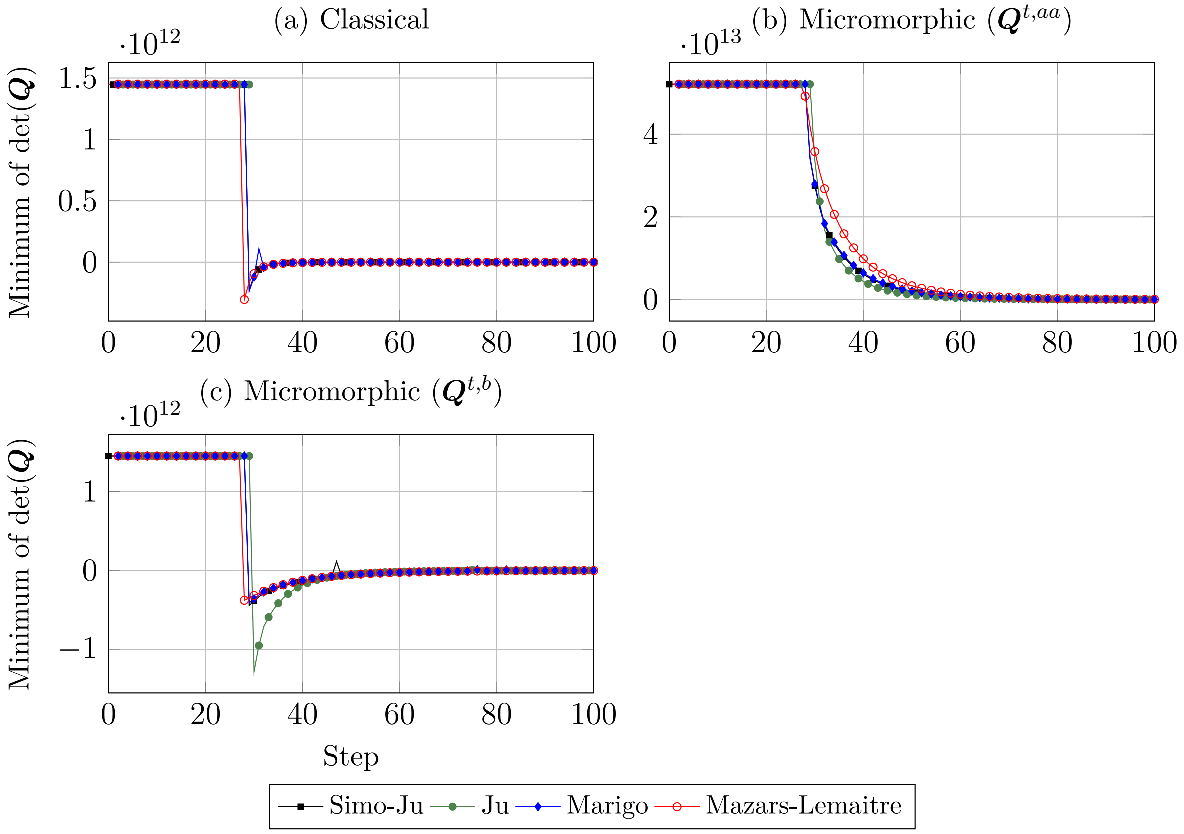

Figure 4.5: Uniaxial stress state: minimum of det($\boldsymbol{Q}$)

Finally, the damage distribution for points A (where localization is first detected) and

D (the final step of the nonlinear analysis, see Fig. 4.3) is shown in Fig. 4.6.

For the classical continuum (Figs. 4.6(a) and 4.6(c)), material degradation is entirely confined to the weakened element, while the surrounding elements unload. Strain localization is observed at all material points within this element. The red line and arrow represent the numerically computed unit vector $\boldsymbol{n}$, while the green line qualitatively indicates the potential crack direction.

In contrast, the micromorphic continuum (Figs. 4.6(b) and 4.6(d)) provides a more accurate representation of localization. Although damage initially concentrates in the weakened element, and localization is first detected at its material points, all three elements eventually exhibit damage as the analysis progresses. Strain localization is identified in all material points throughout the model adopting the microscale acoustic tensor $\boldsymbol{Q}^{t,b}$. Furthermore, the predicted direction for discontinuity insertion fits well with the expectations for a tensile problem.

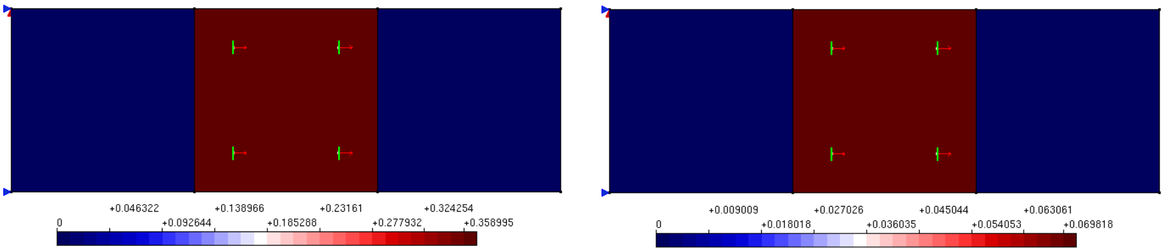

(a) Classical continuum (A)

(b) Micromorphic continuum (A)

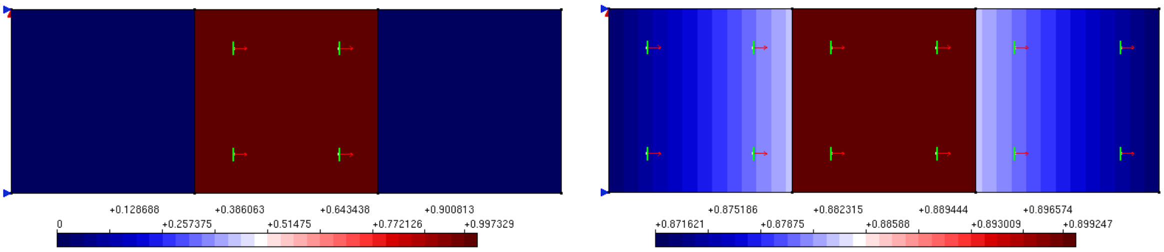

(c) Classical continuum (D)

(d) Micromorphic continuum (D)

Figure 4.6: Uniaxial stress state: damage (Mazars-Lemaitre damage model)

The results of this example lead to the definition of a localization analysis based on the microscale acoustic tensor, defined in Eq. (4.43), which is able to circumvent the regularization properties of the micromorhic continuum and indicate the moment and direction for the introduction of a strong discontinuity.

4.3.2 L-shaped panel

In order to verify the effectiveness of the microscale acoustic tensor $\boldsymbol{Q}^{t,b}$ for the localization analysis in a micromorphic medium, the L-shaped concrete panel shown in Fig. 4.7 is studied. This model was investigated both numerically and experimentally by Winkler et al. (2004) and, as explored by Reges et al. (2023), presents mesh dependent results when considering a classical continuum theory.

For this simulation, the material behavior was reproduced adopting the Mazars-Lemaitre micromorphic damage model with evolution defined by an exponential law (see Eq. (4.47)) and the following parameters: $\alpha = 0.950$, $\beta = 1100$, and $K_0 = 1.12 \times 10^{-4}$. The homogenization technique adopted a square microcontinuum with size 1 mm, Young's modulus $E = 25850$ MPa, and Poisson's ratio $\nu = 0.18$.

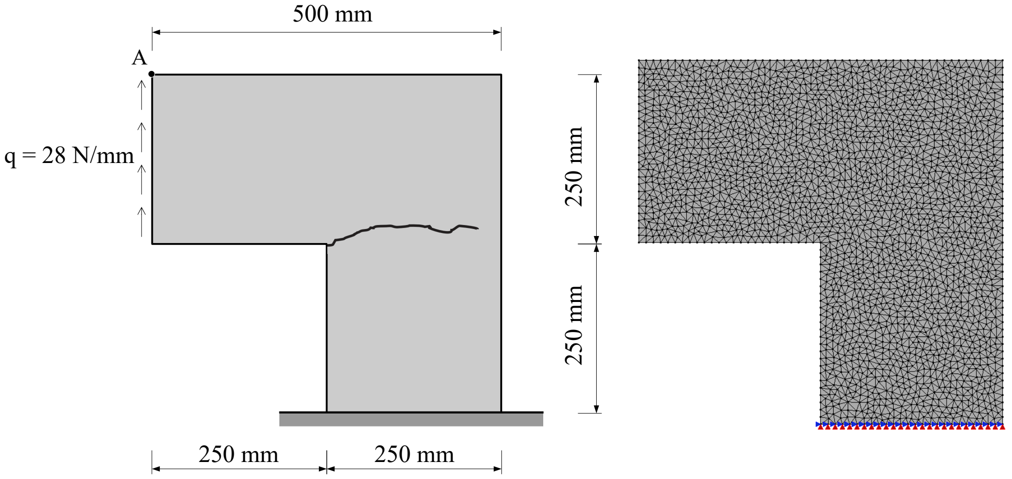

Figure 4.7: L-shaped panel: geometry and mesh

For the simulation, a mesh formed by three-node triangular elements with mean nodal spacing of 10 mm in a plane-stress state and thickness of 100 mm was adopted. The nonlinear analysis was conducted adopting the displacement control method (Yang and Shieh, 1990) with an increment of 1×10^{-2} mm for the vertical displacement of node A in the upper left corner (Fig. 4.7), and a tolerance of 10^{-3} regarding displacements.

The results of the analyses conducted with the classical and the micromorphic theories are illustrated in Fig. 4.8, in which the vertical displacement of the control point A (Fig. 4.7) is plotted against the load factor as well as the experimental range obtained by Winkler et al. (2004).

The results with the use of the micromorphic continuum were similar to the experimental findings in regards to the maximum value of the load factor and the shape of the softening branch. However, the initial stiffness was greater than that observed in the experimental data. Nevertheless, this is a common problem in other simulations of this test, as evidenced by the numerical results presented for this problem in Winkler et al.

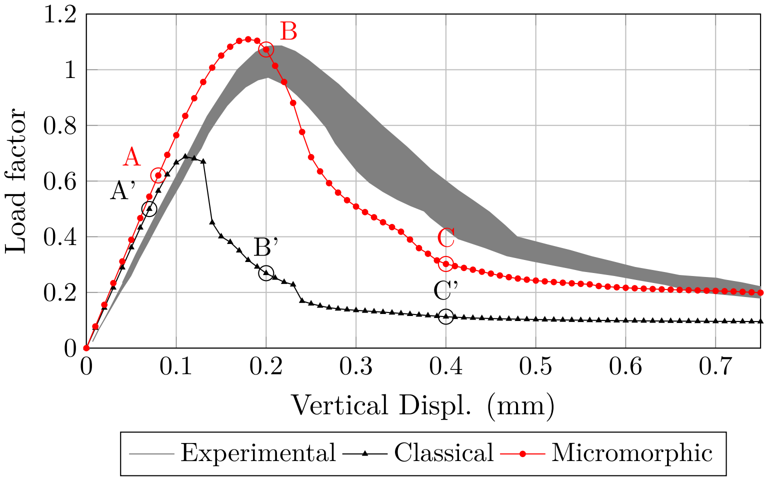

Figure 4.8: L-shaped panel: equilibrium paths

(2004). Considering the classical continuum, the results seemed to be significantly influenced by the mesh with a much lower maximum load factor value and some instabilities in the softening branch.

The damage configurations for the classical and micromorphic analyses are shown in Figs. 4.9 and 4.10, respectively, where the points marked in the equilibrium paths (see Fig. 4.8) are used as reference. Regarding points A and A', that mark the first step in which localization is detected, it can be noticed that localization is first detected in the classical continuum for a load inferior to that of the micromorphic continuum, pointing to the tendency of the classical analysis to concentrate the damage. Additionally, while both simulations exhibit a damage zone shape that closely resembles the experimental cracking path shown in Fig. 4.7, the classical continuum yields a narrower damage zone. This indicates a stronger influence of mesh discretization in the classical model when compared to the more distributed damage response observed in the micromorphic formulation, in accordance with the results in Reges et al. (2023).

Furthermore, the micromorphic theory is also able to detect damage in the bottom left side of the panel, region also subjected to traction stresses, as seen in Figs. 4.10(b) and 4.10(c). The classical continuum, on the other hand, is not able to detect this phenomenon (Fig. 4.9) as damage tend to concentrate near the inner corner, also pointing to the regularization capacity of the micromorphic theory.

As in the uniaxial example discussed in Section 4.3.1, the normal direction for which the determinant of the acoustic tensor becomes negative is represented geometrically by a red arrow, while the expected discontinuity direction, perpendicular to $\boldsymbol{n}$, is depicted by a green line. The findings confirm that the localization analysis based on the microscale acoustic tensor $\boldsymbol{Q}^{t,b}$ (Eq. 4.43) is capable of identifying localization in micromorphic media. Moreover, it effectively guides the insertion of a strong discontinuity in the appropriate direction.

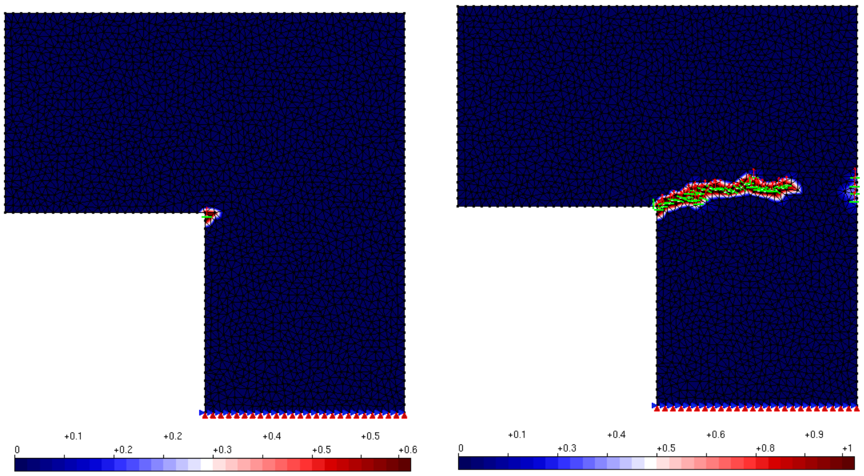

(a) Step 7 (A')

(b) Step 20 (B')

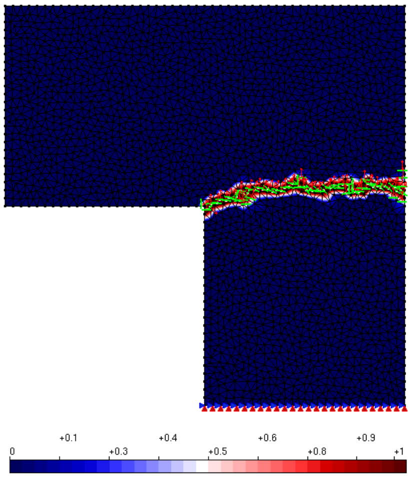

(c) Step 40 (C')

Figure 4.9: L-shaped panel: localization analysis and damage distribution for the classical continuum

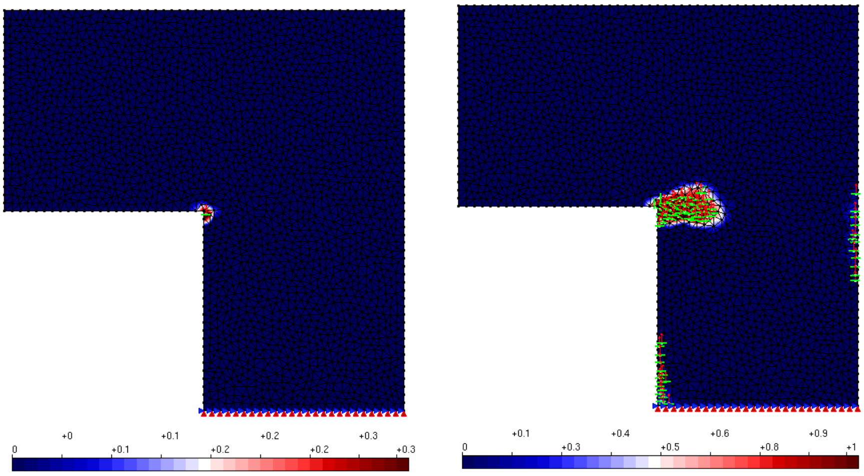

(a) Step 8 (A)   (b) Step 20 (B)

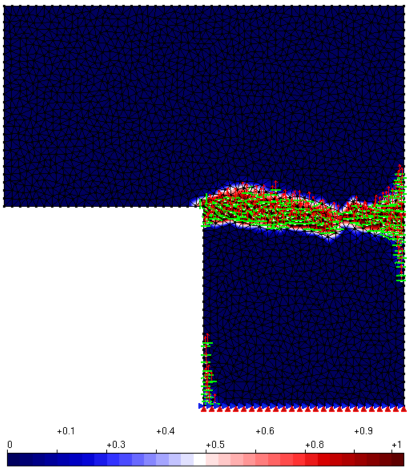

(c) Step 40 (C)

Figure 4.10: L-shaped panel: localization analysis and damage distribution for the micromorphic continuum

Chapter 5

Micromorphic enriched-FEM model

This chapter introduces the micromorphic enriched-FEM formulation, detailing its implementation and presenting numerical examples that validate the proposed approach.

5.1 Basic concepts

The methodology adopted in this study is based on the extended finite element method (XFEM), initially introduced by Oden et al. (1998) and Strouboulis et al. (2000). As noted in Belytschko et al. (2009), the terms Generalized Finite Element Method (GFEM) and XFEM refer to the same approach and are used interchangeably in this work. Originally developed as an extension of the finite element method (FEM), XFEM incorporates additional functions that enhance the modeling of complex material behaviors, particularly in problems involving discontinuities and singularities.

One of the main advantages of this technique is its ability to effectively handle discontinuities without requiring remeshing. By incorporating appropriate enrichment functions, XFEM can accurately capture the characteristics of cracks and other localized phenomena. Several studies have explored this method over the years, and comprehensive reviews can be found in Belytschko et al. (2009) and Fries and Belytschko (2010).

Despite its extensive application in classical continuum mechanics, the use of XFEM within the framework of higher-order continuum models remains relatively unexplored. To the best of the author's knowledge, no prior studies have applied XFEM to micromorphic continua, although an application to micropolar theory has been proposed by Khoei and Karimi (2008).

In this study, a novel combined micromorphic continuum–XFEM model is introduced to simulate crack propagation. The formulation of this model is detailed in the next section. The standard finite element approximation is enriched by additional terms based on the Heaviside function to effectively capture discontinuities. The terms introduced in this chapter are detailed in matrix and vector form in Appendix A for better readability.

5.2 Formulation

To formulate a finite element interpolation that considers displacements jumps, first it is considered a body $\mathcal{V}$ split by a discontinuity $\partial\mathcal{V}_d$, as shown in Fig. 5.1.

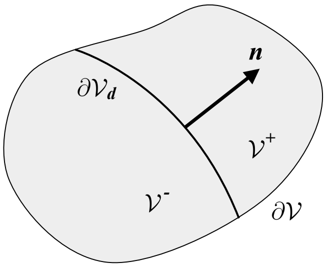

Figure 5.1: Domain $\mathcal{V}$ split by a discontinuity $\partial\mathcal{V}_d$

In a general case, similar to a classical framework (Wells and Sluys, 2001), both displacement u_i and micromotion gradient ϕ_{ij} fields present a discontinuity and can be decomposed into a *continuous* part and a *discontinuous* part

$$\boldsymbol{u}(\boldsymbol{x},t) = \hat{\boldsymbol{u}}(\boldsymbol{x},t) + \mathcal{H}[\![\boldsymbol{u}(\boldsymbol{x},t)]\!] \tag{5.1}$$

$$\boldsymbol{\phi}(\boldsymbol{x},t) = \hat{\boldsymbol{\phi}}(\boldsymbol{x},t) + \mathcal{H}[\![\boldsymbol{\phi}(\boldsymbol{x},t)]\!] \tag{5.2}$$

where $\boldsymbol{u}$, $[\![\boldsymbol{u}]\!]$, $\boldsymbol{\phi}$, and $[\![\boldsymbol{\phi}]\!]$ are continuous functions on $\mathcal{V}$ and $\mathcal{H}$ is the Heaviside function centered on the discontinuity $\partial\mathcal{V}_d$ ($\mathcal{H} = 1$ if $\boldsymbol{x} \in \mathcal{V}^+$, $\mathcal{H} = 0$ if $\boldsymbol{x} \in \mathcal{V}^-$).

Based on Eqs. (5.1) and (5.2), the displacement and micromotion gradient fields can be interpolated, adopting different interpolations for macro and micromotion (Hirschberger (2008), Silva et al. (2022)), by

$$\boldsymbol{u} = \underbrace{\boldsymbol{N}\boldsymbol{d}_{\boldsymbol{u}}}_{\hat{u}} + \mathcal{H}\underbrace{\boldsymbol{N}\boldsymbol{d}'_{\boldsymbol{u}}}_{[\![u]\!]} \tag{5.3}$$

$$\boldsymbol{\phi} = \underbrace{\bar{\boldsymbol{N}}\boldsymbol{d}_{\phi}}_{\hat{\phi}} + \mathcal{H}\underbrace{\bar{\boldsymbol{N}}\boldsymbol{d}'_{\phi}}_{[\![\phi]\!]} \tag{5.4}$$

where $\boldsymbol{N}$ and $\bar{\boldsymbol{N}}$ are the standard finite element shape function for the macro and micromotion, respectively; $\boldsymbol{d}_{\boldsymbol{u}}$ and $\boldsymbol{d}_{\phi}$ are the regular micromorphic nodal degrees of freedom; $\boldsymbol{d}'_{\boldsymbol{u}}$ and $\boldsymbol{d}'_{\phi}$ are the enhanced nodal degrees of freedom. The first term in Eqs. (5.3) and (5.4) can be considered to represent the continuous part of the interpolated fields and the second term, multiplying the Heaviside function, the discontinuous part.

The jump in the displacement $\boldsymbol{u}$ correspond to a discontinuity in the macroscale degrees of freedom, similar to that of a classical continuum. In contrast, the micromotion gradient ϕ_{ij} characterizes the deformation state at the microscale level. Consequently, a discontinuity in this field indicates that particles on either side of the interface can undergo distinct deformations. In the context of XFEM applied to generalized continua, different hypotheses can be assumed including the possibility of only enriching the macroscale degrees of freedom (e.g., Khoei and Karimi (2008)).

Accordingly, the strain tensors defined in Eq. (3.12) in elements where the degrees of freedom have been enhanced can be expressed as

$$\begin{aligned}\boldsymbol{\epsilon} &= \boldsymbol{M}\boldsymbol{L_u}\boldsymbol{N}\boldsymbol{d_u} + \mathcal{H}\boldsymbol{M}\boldsymbol{L_u}\boldsymbol{N}\boldsymbol{d}'_{\boldsymbol{u}} + \boldsymbol{\nabla}\mathcal{H}\boldsymbol{N}\boldsymbol{d}'_{\boldsymbol{u}} - \boldsymbol{M}\bar{\boldsymbol{N}}\boldsymbol{d}_{\phi} - \boldsymbol{M}\mathcal{H}\bar{\boldsymbol{N}}\boldsymbol{d}'_{\phi} \\ \boldsymbol{\epsilon} &= \boldsymbol{B_u}\boldsymbol{d_u} + \mathcal{H}\boldsymbol{B_u}\boldsymbol{d}'_{\boldsymbol{u}} + \boldsymbol{\nabla}\mathcal{H}\boldsymbol{N}\boldsymbol{d}'_{\boldsymbol{u}} - \bar{\boldsymbol{N}}_{\boldsymbol{T}}\boldsymbol{d}_{\phi} - \mathcal{H}\bar{\boldsymbol{N}}_{\boldsymbol{T}}\boldsymbol{d}'_{\phi} \end{aligned} \tag{5.5}$$

$$\begin{aligned} 2\boldsymbol{e} &= \bar{\boldsymbol{N}}\boldsymbol{d}_{\phi} + \mathcal{H}\bar{\boldsymbol{N}}\boldsymbol{d}'_{\phi} + \boldsymbol{M}\bar{\boldsymbol{N}}\boldsymbol{d}_{\phi} + \mathcal{H}\boldsymbol{M}\bar{\boldsymbol{N}}\boldsymbol{d}'_{\phi} \\ \boldsymbol{e} &= \bar{\boldsymbol{N}}_{\boldsymbol{S}}\boldsymbol{d}_{\phi} + \mathcal{H}\bar{\boldsymbol{N}}_{\boldsymbol{S}}\boldsymbol{d}'_{\phi} \end{aligned} \tag{5.6}$$

$$\begin{aligned} \boldsymbol{\gamma} &= \boldsymbol{L}_{\phi}\bar{\boldsymbol{N}}\boldsymbol{d}_{\phi} + \mathcal{H}\boldsymbol{L}_{\phi}\bar{\boldsymbol{N}}\boldsymbol{d}'_{\phi} + \boldsymbol{\nabla}\mathcal{H}\bar{\boldsymbol{N}}\boldsymbol{d}'_{\phi} \\ \boldsymbol{\gamma} &= \boldsymbol{B}_{\phi}\boldsymbol{d}_{\phi} + \mathcal{H}\boldsymbol{B}_{\phi}\boldsymbol{d}'_{\phi} + \boldsymbol{\nabla}\mathcal{H}\bar{\boldsymbol{N}}\boldsymbol{d}'_{\phi} \end{aligned} \tag{5.7}$$

where $\boldsymbol{B_u}$ and $\boldsymbol{B}_{\phi}$ are strain approximation matrices, and $\bar{\boldsymbol{N}}_{\boldsymbol{T}}$ and $\bar{\boldsymbol{N}}_{\boldsymbol{S}}$ are matrices of the interpolation functions of the micromotion "transposed" and "symmetric"

$$\boldsymbol{B_u} = \boldsymbol{M}\boldsymbol{L_u}\boldsymbol{N}, \quad \boldsymbol{B}_{\phi} = \boldsymbol{L}_{\phi}\bar{\boldsymbol{N}}, \quad \bar{\boldsymbol{N}}_{\boldsymbol{T}} = \boldsymbol{M}\bar{\boldsymbol{N}}, \quad \bar{\boldsymbol{N}}_{\boldsymbol{S}} = \frac{1}{2}\left(\bar{\boldsymbol{N}} + \bar{\boldsymbol{N}}_{\boldsymbol{T}}\right) \tag{5.8}$$

in which $\boldsymbol{M}$ is a rearrangement matrix, necessary for the proper computation of the strain components in vector form; $\boldsymbol{L_u}$ and $\boldsymbol{L}_{\phi}$ are differential operators ($\partial_i = \partial/\partial X_i$).

Based on the approximations defined in Eqs. (5.5) through (5.7), the strain fields variations may be written as

$$\delta\boldsymbol{\epsilon} = \boldsymbol{B_u}\delta\boldsymbol{d_u} + \mathcal{H}\boldsymbol{B_u}\delta\boldsymbol{d}'_{\boldsymbol{u}} + \boldsymbol{\nabla}\mathcal{H}\boldsymbol{N}\delta\boldsymbol{d}'_{\boldsymbol{u}} - \bar{\boldsymbol{N}}_{\boldsymbol{T}}\delta\boldsymbol{d}_{\phi} - \mathcal{H}\bar{\boldsymbol{N}}_{\boldsymbol{T}}\delta\boldsymbol{d}'_{\phi} \tag{5.9}$$

$$\delta\boldsymbol{e} = \bar{\boldsymbol{N}}_{\boldsymbol{S}}\delta\boldsymbol{d}_{\phi} + \mathcal{H}\bar{\boldsymbol{N}}_{\boldsymbol{S}}\delta\boldsymbol{d}'_{\phi} \tag{5.10}$$

$$\delta\boldsymbol{\gamma} = \boldsymbol{B}_{\phi}\delta\boldsymbol{d}_{\phi} + \mathcal{H}\boldsymbol{B}_{\phi}\delta\boldsymbol{d}'_{\phi} + \boldsymbol{\nabla}\mathcal{H}\bar{\boldsymbol{N}}\delta\boldsymbol{d}'_{\phi}\ . \tag{5.11}$$

Following, the stress-strain relations presented in Eqs. (3.19), (3.20), and (3.21) are rewritten in matrix format to obtain the stress fields approximations

$$\boldsymbol{t} = \boldsymbol{A}\boldsymbol{\epsilon} + \boldsymbol{E}\boldsymbol{e} \quad \therefore \tag{5.12a}$$

$$\boldsymbol{t} = \boldsymbol{A}[\boldsymbol{B_u}\boldsymbol{d_u} + \mathcal{H}\boldsymbol{B_u}\boldsymbol{d}'_{\boldsymbol{u}} + \boldsymbol{\nabla}\mathcal{H}\boldsymbol{N}\boldsymbol{d}'_{\boldsymbol{u}} - \bar{\boldsymbol{N}}_{\boldsymbol{T}}\boldsymbol{d}_\phi - \mathcal{H}\bar{\boldsymbol{N}}_{\boldsymbol{T}}\boldsymbol{d}'_\phi] + \boldsymbol{E}[\bar{\boldsymbol{N}}_{\boldsymbol{S}}\boldsymbol{d}_\phi + \mathcal{H}\bar{\boldsymbol{N}}_{\boldsymbol{S}}\boldsymbol{d}'_\phi] \tag{5.12b}$$

$$\boldsymbol{s} = \boldsymbol{E}^T\boldsymbol{\epsilon} + \boldsymbol{B}\boldsymbol{e} \quad \therefore \tag{5.13a}$$

$$\boldsymbol{s} = \boldsymbol{E}^T[\boldsymbol{B_u}\boldsymbol{d_u} + \mathcal{H}\boldsymbol{B_u}\boldsymbol{d}'_{\boldsymbol{u}} + \boldsymbol{\nabla}\mathcal{H}\boldsymbol{N}\boldsymbol{d}'_{\boldsymbol{u}} - \bar{\boldsymbol{N}}_{\boldsymbol{T}}\boldsymbol{d}_\phi - \mathcal{H}\bar{\boldsymbol{N}}_{\boldsymbol{T}}\boldsymbol{d}'_\phi] + \boldsymbol{B}[\bar{\boldsymbol{N}}_{\boldsymbol{S}}\boldsymbol{d}_\phi + \mathcal{H}\bar{\boldsymbol{N}}_{\boldsymbol{S}}\boldsymbol{d}'_\phi] \tag{5.13b}$$

$$\boldsymbol{m} = \boldsymbol{C}\boldsymbol{\gamma} \quad \therefore \tag{5.14a}$$

$$\boldsymbol{m} = \boldsymbol{C}[\boldsymbol{B}_\phi\boldsymbol{d}_\phi + \mathcal{H}\boldsymbol{B}_\phi\boldsymbol{d}'_\phi + \boldsymbol{\nabla}\mathcal{H}\bar{\boldsymbol{N}}\boldsymbol{d}'_\phi] \tag{5.14b}$$

The equilibrium condition is obtained restructuring Eqs. (3.23) and (3.24) in matrix format

$$\begin{aligned}\delta^{(1)}\Pi &= \int_{\mathcal{V}} \left(\delta\boldsymbol{\epsilon}^T\boldsymbol{t} + \delta\boldsymbol{e}^T\boldsymbol{s} + \delta\boldsymbol{\gamma}^T\boldsymbol{m}\right) dv - \\ &- \int_{\mathcal{V}} \left(\delta\boldsymbol{u}^T\rho\boldsymbol{f} + \delta\boldsymbol{\phi}^T\rho\boldsymbol{l}\right) dv - \int_{\partial\mathcal{V}} \left(\delta\boldsymbol{u}^T\hat{\boldsymbol{t}}_{(\boldsymbol{n})} + \delta\boldsymbol{\phi}^T\hat{\boldsymbol{m}}_{(\boldsymbol{n})}\right) ds = 0\end{aligned} \tag{5.15}$$

Substituting into the stationary condition in Eq. (5.15) the approximations for the strain and stress fields (Eqs. (5.9) to (5.14))

$$\begin{aligned}\delta^{(1)}\boldsymbol{\Pi} = \int_{\mathcal{V}} &\left[\delta\boldsymbol{d}_{\boldsymbol{u}}^T\boldsymbol{B}_{\boldsymbol{u}}^T + \mathcal{H}\delta\boldsymbol{d}_{\boldsymbol{u}}'^T\boldsymbol{B}_{\boldsymbol{u}}^T + \delta\boldsymbol{d}_{\boldsymbol{u}}'^T\boldsymbol{N}^T\left(\boldsymbol{\nabla}^T\mathcal{H}\right) - \delta\boldsymbol{d}_{\boldsymbol{\phi}}^T\bar{\boldsymbol{N}}_{\boldsymbol{T}}{}^T - \mathcal{H}\delta\boldsymbol{d}_{\boldsymbol{\phi}}'^T\bar{\boldsymbol{N}}_{\boldsymbol{T}}{}^T\right] \\ &\left\{\boldsymbol{A}\left[\boldsymbol{B_u}\boldsymbol{d_u} + \mathcal{H}\boldsymbol{B_u}\boldsymbol{d}'_{\boldsymbol{u}} + (\boldsymbol{\nabla}\mathcal{H})\,\boldsymbol{N}\boldsymbol{d}'_{\boldsymbol{u}} - \bar{\boldsymbol{N}}_{\boldsymbol{T}}\boldsymbol{d}_\phi - \mathcal{H}\bar{\boldsymbol{N}}_{\boldsymbol{T}}\boldsymbol{d}'_\phi\right] + \boldsymbol{E}\left[\bar{\boldsymbol{N}}_{\boldsymbol{S}}\boldsymbol{d}_\phi + \mathcal{H}\bar{\boldsymbol{N}}_{\boldsymbol{S}}\boldsymbol{d}'_\phi\right]\right\} dv \\ &+ \int_{\mathcal{V}} \left(\delta\boldsymbol{d}_{\boldsymbol{\phi}}^T\bar{\boldsymbol{N}}_{\boldsymbol{S}}{}^T + \mathcal{H}\delta\boldsymbol{d}_{\boldsymbol{\phi}}'^T\bar{\boldsymbol{N}}_{\boldsymbol{S}}{}^T\right)\left\{\boldsymbol{E}^T\left[\boldsymbol{B_u}\boldsymbol{d_u} + \mathcal{H}\boldsymbol{B_u}\boldsymbol{d}'_{\boldsymbol{u}} + (\boldsymbol{\nabla}\mathcal{H})\,\boldsymbol{N}\boldsymbol{d}'_{\boldsymbol{u}} - \right.\right. \\ &\left.\left.\bar{\boldsymbol{N}}_{\boldsymbol{T}}\boldsymbol{d}_\phi - \mathcal{H}\bar{\boldsymbol{N}}_{\boldsymbol{T}}\boldsymbol{d}'_\phi\right] + \boldsymbol{B}\left[\bar{\boldsymbol{N}}_{\boldsymbol{S}}\boldsymbol{d}_\phi + \mathcal{H}\bar{\boldsymbol{N}}_{\boldsymbol{S}}\boldsymbol{d}'_\phi\right]\right\} dv \\ &+ \int_{\mathcal{V}} \left[\delta\boldsymbol{d}_{\boldsymbol{\phi}}^T\boldsymbol{B}_{\boldsymbol{\phi}}^T + \mathcal{H}\delta\boldsymbol{d}_{\boldsymbol{\phi}}'^T\boldsymbol{B}_{\boldsymbol{\phi}}^T + \delta\boldsymbol{d}_{\boldsymbol{\phi}}'^T\bar{\boldsymbol{N}}^T\left(\boldsymbol{\nabla}^T\mathcal{H}\right)\right]\left\{\boldsymbol{C}\left[\boldsymbol{B}_\phi\boldsymbol{d}_\phi + \mathcal{H}\boldsymbol{B}_\phi\boldsymbol{d}'_{\boldsymbol{\phi}} + (\boldsymbol{\nabla}\mathcal{H})\,\bar{\boldsymbol{N}}\boldsymbol{d}'_{\boldsymbol{\phi}}\right]\right\} dv \\ &- \int_{\mathcal{V}} \left[\left(\delta\boldsymbol{d}_{\boldsymbol{u}}^T\boldsymbol{N}^T + \mathcal{H}\delta\boldsymbol{d}_{\boldsymbol{u}}'^T\boldsymbol{N}^T\right)\rho\boldsymbol{f} + \left(\delta\boldsymbol{d}_{\boldsymbol{\phi}}^T\bar{\boldsymbol{N}}^T + \mathcal{H}\delta\boldsymbol{d}_{\boldsymbol{\phi}}'^T\bar{\boldsymbol{N}}^T\right)\rho\boldsymbol{l}\right] dv \\ &- \int_{\partial\mathcal{V}} \left[\left(\delta\boldsymbol{d}_{\boldsymbol{u}}^T\boldsymbol{N}^T + \mathcal{H}\delta\boldsymbol{d}_{\boldsymbol{u}}'^T\boldsymbol{N}^T\right)\hat{\boldsymbol{t}}_{(\boldsymbol{n})} + \left(\delta\boldsymbol{d}_{\boldsymbol{\phi}}^T\bar{\boldsymbol{N}}^T + \mathcal{H}\delta\boldsymbol{d}_{\boldsymbol{\phi}}'^T\bar{\boldsymbol{N}}^T\right)\hat{\boldsymbol{m}}_{(\boldsymbol{n})}\right] ds = 0\end{aligned} \tag{5.16}$$

Considering that the traction transmitted across a crack is zero, i.e., traction-free discontinuity, it can be obtained

$$\begin{bmatrix} \boldsymbol{K_{uu}} & \boldsymbol{K_{u\phi}} & \boldsymbol{K_{uu'}} & \boldsymbol{K_{u\phi'}} \\ \boldsymbol{K_{\phi u}} & \boldsymbol{K_{\phi\phi}} & \boldsymbol{K_{\phi u'}} & \boldsymbol{K_{\phi\phi'}} \\ \boldsymbol{K_{u'u}} & \boldsymbol{K_{u'\phi}} & \boldsymbol{K_{u'u'}} & \boldsymbol{K_{u'\phi'}} \\ \boldsymbol{K_{\phi'u}} & \boldsymbol{K_{\phi'\phi}} & \boldsymbol{K_{\phi'u'}} & \boldsymbol{K_{\phi'\phi'}} \end{bmatrix} \begin{Bmatrix} \boldsymbol{d_u} \\ \boldsymbol{d_\phi} \\ \boldsymbol{d_{u'}} \\ \boldsymbol{d_{\phi'}} \end{Bmatrix} = \begin{Bmatrix} \boldsymbol{f}_{eq,\boldsymbol{u}} \\ \boldsymbol{f}_{eq,\phi} \\ \boldsymbol{f}_{eq,\boldsymbol{u'}} \\ \boldsymbol{f}_{eq,\phi'} \end{Bmatrix} \tag{5.17}$$

where

$$\boldsymbol{K_{uu}} = \int_{\mathcal{V}} \boldsymbol{B_u^T A B_u} dv \tag{5.18}$$

$$\boldsymbol{K_{u\phi}} = \int_{\mathcal{V}} \left(\boldsymbol{B_u^T E \bar{N}_S} - \boldsymbol{B_u^T A \bar{N}_T} \right) dv = \boldsymbol{K_{\phi u}^T} \tag{5.19}$$

$$\boldsymbol{K_{uu'}} = \int_{\mathcal{V}} \mathcal{H} \boldsymbol{B_u^T A B_u} dv = \boldsymbol{K_{u'u}^T} \tag{5.20}$$

$$\boldsymbol{K_{u\phi'}} = \int_{\mathcal{V}} \left(\mathcal{H} \boldsymbol{B_u^T E \bar{N}_S} - \mathcal{H} \boldsymbol{B_u^T A \bar{N}_T} \right) dv = \boldsymbol{K_{\phi'u}^T} = \boldsymbol{K_{u'\phi}} = \boldsymbol{K_{\phi u'}^T} \tag{5.21}$$

$$\boldsymbol{K_{\phi\phi}} = \int_{\mathcal{V}} \left(\boldsymbol{\bar{N}_T^T A \bar{N}_T} - \boldsymbol{\bar{N}_T^T E \bar{N}_S} - \boldsymbol{\bar{N}_S^T E^T \bar{N}_T} + \boldsymbol{\bar{N}_S^T B \bar{N}_S} + \boldsymbol{B_\phi^T C B_\phi} \right) dv \tag{5.22}$$

$$\boldsymbol{K_{\phi\phi'}} = \int_{\mathcal{V}} (\mathcal{H} \boldsymbol{\bar{N}_T^T A \bar{N}_T} - \mathcal{H} \boldsymbol{\bar{N}_T^T E \bar{N}_S} - \mathcal{H} \boldsymbol{\bar{N}_S^T E^T \bar{N}_T} + \mathcal{H} \boldsymbol{\bar{N}_S^T B \bar{N}_S} + \mathcal{H} \boldsymbol{B_\phi^T C B_\phi}) dv = \boldsymbol{K_{\phi'\phi}^T} \tag{5.23}$$

$$\boldsymbol{K_{u'u'}} = \int_{\mathcal{V}} \mathcal{H}^2 \boldsymbol{B_u^T A B_u} dv \tag{5.24}$$

$$\boldsymbol{K_{u'\phi'}} = \int_{\mathcal{V}} \left(\mathcal{H}^2 \boldsymbol{B_u^T E \bar{N}_S} - \mathcal{H}^2 \boldsymbol{B_u^T A \bar{N}_T} \right) dv = \boldsymbol{K_{\phi'u'}^T} \tag{5.25}$$

$$\boldsymbol{K_{\phi'\phi'}} = \int_{\mathcal{V}} \mathcal{H}^2 \boldsymbol{\bar{N}_T^T A \bar{N}_T} - \mathcal{H}^2 \boldsymbol{\bar{N}_T^T E \bar{N}_S} - \mathcal{H}^2 \boldsymbol{\bar{N}_S^T E^T \bar{N}_T} + \mathcal{H}^2 \boldsymbol{\bar{N}_S^T B \bar{N}_S} + \mathcal{H}^2 \boldsymbol{B_\phi^T C B_\phi} dv \tag{5.26}$$

$$\boldsymbol{f}_{eq,\boldsymbol{u}} = \int_{\mathcal{V}} \boldsymbol{N}^T \rho \boldsymbol{f} dv + \int_{\partial\mathcal{V}} \boldsymbol{N}^T \hat{\boldsymbol{t}}_{(\boldsymbol{n})} ds \tag{5.27}$$

$$\boldsymbol{f}_{eq,\boldsymbol{\phi}} = \int_{\mathcal{V}} \bar{\boldsymbol{N}}^T \rho \boldsymbol{l} dv + \int_{\partial\mathcal{V}} \bar{\boldsymbol{N}}^T \hat{\boldsymbol{m}}_{(\boldsymbol{n})} ds \tag{5.28}$$

$$\boldsymbol{f}_{eq,\boldsymbol{u}'} = \int_{\mathcal{V}} \mathcal{H}\boldsymbol{N}^T \rho \boldsymbol{f} dv + \int_{\partial\mathcal{V}} \mathcal{H}\boldsymbol{N}^T \hat{\boldsymbol{t}}_{(\boldsymbol{n})} ds \tag{5.29}$$

$$\boldsymbol{f}_{eq,\boldsymbol{\phi}'} = \int_{\mathcal{V}} \mathcal{H}\bar{\boldsymbol{N}}^T \rho \boldsymbol{l} dv + \int_{\partial\mathcal{V}} \mathcal{H}\bar{\boldsymbol{N}}^T \hat{\boldsymbol{m}}_{(\boldsymbol{n})} ds \tag{5.30}$$

Hence, all the terms necessary for the computational implementation of the micromorphic enriched-FEM approach are determine considering a traction-free discontinuity in which all degrees of freedom are equally enriched. As mentioned, the structure implemented in the INSANE system for XFEM/GFEM and micromorphic media (FEM analysis) were used and expanded to accommodate the proposed approach.

5.3 Numerical simulations

To illustrate the application of the XFEM technique within the framework of the micromorphic continuum, this section presents two numerical simulations: a tensile strip analysis and a three-point bending test. Initially, both cases are modeled using a standard finite element (FEM) approach without enrichment functions. When localization occurs, identified by monitoring the behavior of the microscale micromorphic acoustic tensor as formulated in Section 4.1.2, the enrichment function is incorporated into the standard shape functions.

In the proposed approach, localization is detected at step n and the Heaviside enrichment function is then implemented at step $n + 1$ activating all the additional DOFs corresponding to the generalized displacements of the micromorphic continuum for that specific problem (12 additional DOFs for a three dimensional analysis and 6 for a plane one per node). The discontinuity is introduced adopting the normal direction that resulted from the analysis of the microscale micromorphic acoustic tensor. For a more detailed discussion of the adopted approach, which was initially implemented in the INSANE system for classical continua, the reader is referred to Silva et al. (2016).

5.3.1 Strip in tension

The first example for this section to illustrate the use of XFEM in a micromorphic medium is of a plane strain strip with dimensions 60 mm by 120 mm subjected to a traction load q as illustrated in Fig. 5.2(a). In order to represent the loading conditions of a tensile test, all the points in the loaded face are restrained to the same displacement using the strategy *leader-follower* available in the INSANE system.

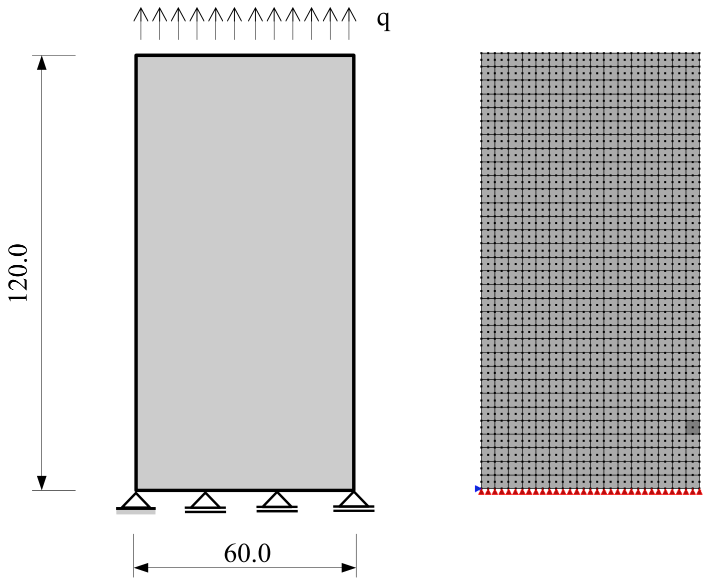

(a) Geometry (b) Mesh

Figure 5.2: Strip in tension: geometry (unit of length: mm), loading, boundary conditions, and mesh

A square homogeneous microcontinuum with dimension 1.25 mm was used associated to a Young's modulus $E = 12000$ MPa and a Poisson's ratio $\nu = 0.35$. The Mazars-Lemaitre damage model (Eq. (3.65) is employed with a linear damage law defined as

$$\mathscr{D}(\Gamma_{eq}) = \frac{K_f}{K_f - K_0}\left(1 - \frac{K_0}{\Gamma_{eq}}\right) \tag{5.31}$$

where K_0 and K_f are threshold values for the equivalent strain defined as $K_0 = 0.0017$ and $K_f = 0.325$, respectively. This study was conducted for the mesh depicted in Fig. 5.2(b) composed of 512 quadrilateral elements with nine nodes and nine integration points. To induce the localization phenomenon a less resistant region was introduced, as highlighted in Fig. 5.2(b), adopting $K_0 = 0.001$ for the respective element, which implies an approximated 40% reduction in the stress corresponding to the elastic limit.

For the loading process, the displacement control method was employed with an initial load factor of 20.0 N, a displacement increment of $1{\times}10^{-3}$ for the loaded face in the vertical direction, and a tolerance for convergence of 10^{-4}. The load factor versus the vertical displacement of the loaded face is show for the micromorphic XFEM technique using the Heaviside function in Fig. 5.3. Steps 119, 124, and 127 are marked in the equilibrium path, corresponding to points A, B e C. These points are used in the discussion of the results presented in the next paragraphs.

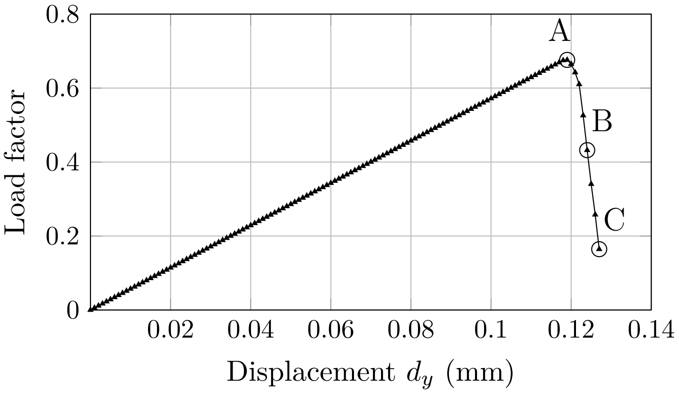

Figure 5.3: Strip in tension: equilibrium path

Figure 5.4 presents the crack path together with the enriched nodes at points A, B, and C. Point A marks the first step in which the crack nucleates in the less resistant element in a direction that agrees with the shear band that tends to develop in this type of problem (Khoei and Karimi, 2008, Silva et al., 2022, Reges et al., 2023). Between points A and B the discontinuity is introduced horizontally and, between steps B and C (last step of the simulation), tends to incline upwards. The discontinuity is not added to the last two elements as, with no cohesion, the analysis does not converge when the whole strip is sectioned by the crack. As observed, the nodes along the edge containing the crack tip are not enriched to ensure a null crack opening at the crack tip.. At the end of simulation, the total number of 576 additional DOFs has been added to the system as all 6 degrees of freedom (d_{u1}, d_{u2}, $d_{\phi 11}$, $d_{\phi 22}$, $d_{\phi 12}$, and $d_{\phi 21}$, as defined in Section 5.2 and Appendix A) of 96 nodes are enriched.

As it can be observed, comparing Figs. 5.3 and 5.4, with no cohesion, the strip under a uniform tension tends to present a brittle fracture corresponding to a sudden drop in the load factor as soon as localization is detected in the weakest element (point A) and the discontinuity is introduced.

Figure 5.5 illustrates the results for the crack mouth opening considering the normal displacement of the first point of the introduced discontinuity throughout the nonlinear analysis. As the crack is first inserted, its opening is zero and, as the load rises and crack propagates, the opening increases rapidly which is consistent with the brittle fracture modeled due to the traction-free crack consideration.

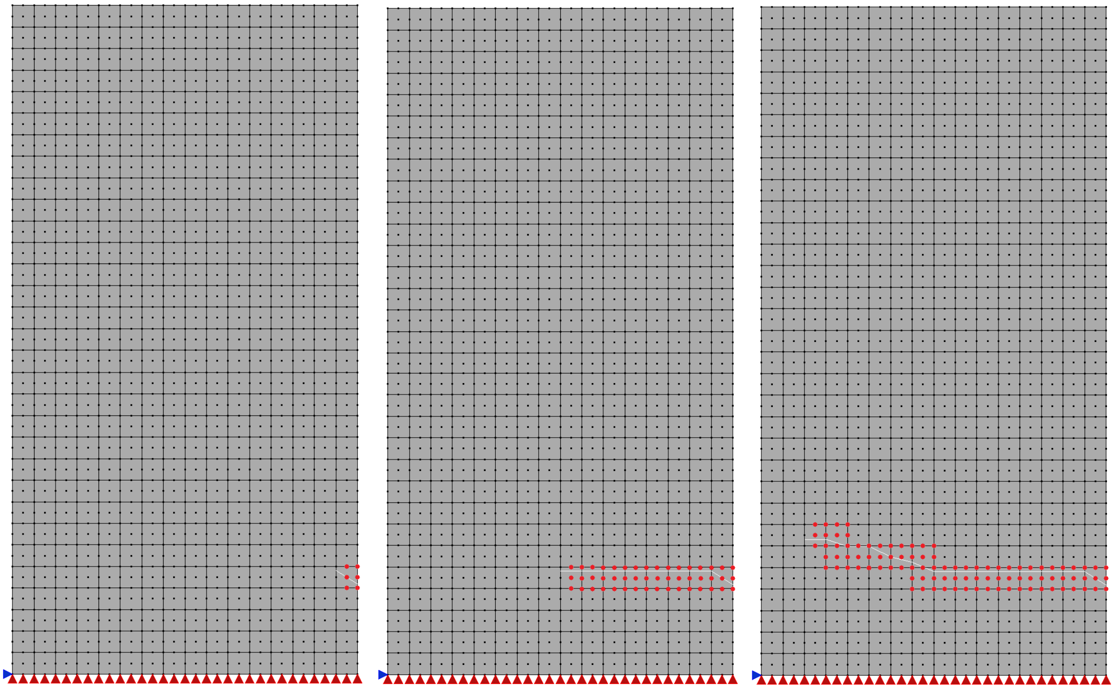
(a) Point A (b) Point B (c) Point C

Figure 5.4: Strip in tension: enriched nodes

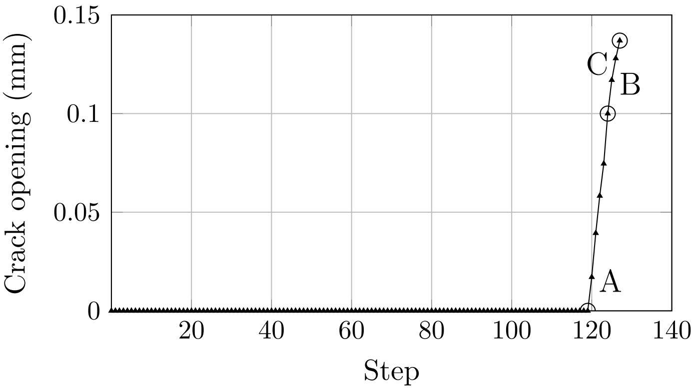

Figure 5.5: Strip in tension: crack opening

Figure 5.6 presents the deformed configuration for points A, B, and C corresponding to displacements of the loaded face $d_y = 0.676$, 0.432, and 0.164 mm. The overall failure observed corresponds to the expected behavior for this simulation under the specified conditions, attesting the effectiveness of the XFEM micromorphic model.

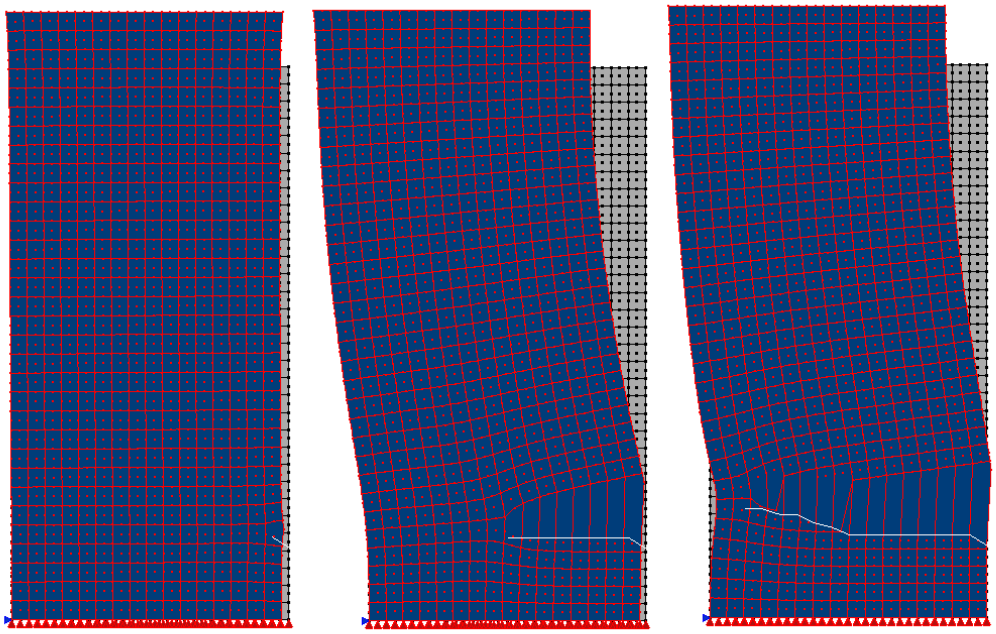
(a) Point A (b) Point B (c) Point C

Figure 5.6: Strip in tension: deformed shape

5.3.2 Three-point bending test

The second and last example to be considered in this chapter is the three-point bending test on a notched concrete beam reported by García-Álvarez et al. (2012). The geometric, loading, and boundary conditions are show in Fig. 5.7(a). The failure of the beam is caused by a crack emerging from the notch tip and propagating vertically along the line of symmetry. For the material, the following properties, taken from García-Álvarez et al. (2012), were adopted: Young's modulus $E = 33800$ MPa and Poisson's ration $\nu = 0.2$. These properties are associated to a square microcontinuum with dimension 1×10^{-10} mm.

In a three-point bending test with an initial notch, it is well known that strain tends to concentrate around the crack tip, potentially leading to numerical instabilities caused by localization, especially when using classical continuous damage models (Souza et al., 2017). This issue can be mitigated by adopting a non-local approach, such as the micromorphic continuum framework, which inherently regularizes strain localization and improves numerical stability.

As illustrated in Fig. 5.7(b), the problem domain is divided into two sub-domains: one nonlinear subdomain to which a Mazars-Lemaitre damage model (Eq. (3.65) is associated and a remaining linear-elastic one. This definition was required to restrict damage evolution only to the region subjected to traction stresses. A linear damage law is employed (see Equation 5.31) where $K_0 = 2 \times 10^{-4}$ and $K_f = 2 \times 10^{-3}$.

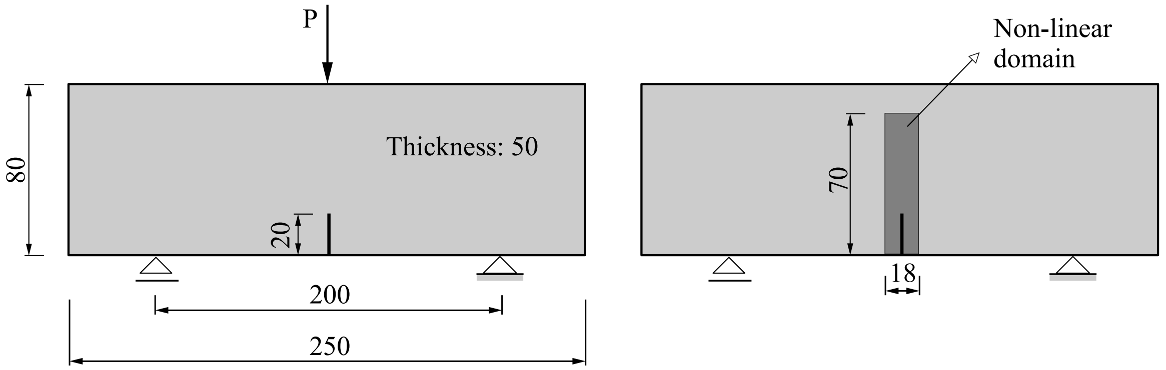

(a) Geometry

(b) Nonlinear domain

Figure 5.7: Three-point bending test: geometry (unit of length: mm), loading, boundary conditions, and selected nonlinear domain

In the numerical simulation the mesh depicted in Fig. 5.8 is considered, composed by triangular linear elements in a plane-stress state with size ranging from 10 mm in the linear-elastic domain to 2 mm in the nonlinear domain. The notch was represented as rectangular with an initial opening of 2 mm.

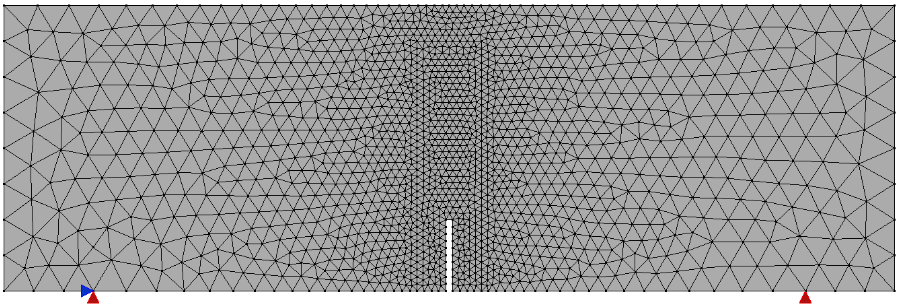

Figure 5.8: Three-point bending test: finite element mesh

For the loading process, the displacement control method was adopted assuming a reference load $P = 1$ N, an increment of 5×10^{-4} mm for the vertical displacement of the point where the load is applied, and a tolerance of 1×10^{-4} for convergence. The results for this analysis performed both for the classical and micromorphic media in terms of crack mouth displacement (CMD) plotted against the load factor are illustrated in Fig. 5.9 as well as the experimental results by García-Álvarez et al. (2012). The classical and the micromorphic analyses were conducted adopting the same parameters for the XFEM model as well as the same discretization.

As it can be observed, the proposed enriched micromorphic model associated to a simple scalar damage model had a good agreement with the experimental data in the ascending branch and for the peak load. The post-peak branch is clearly more steep than the expected one as the proposed model involves a brittle fracture, wherein no cohesion is inserted between crack surfaces. The simulation with the classical continuum and same parameters show a lower peak load. This could be associated to the stronger mesh dependency for analyses involving classical media modeled with scalar damage models Silva et al. (2022), Reges et al. (2023).

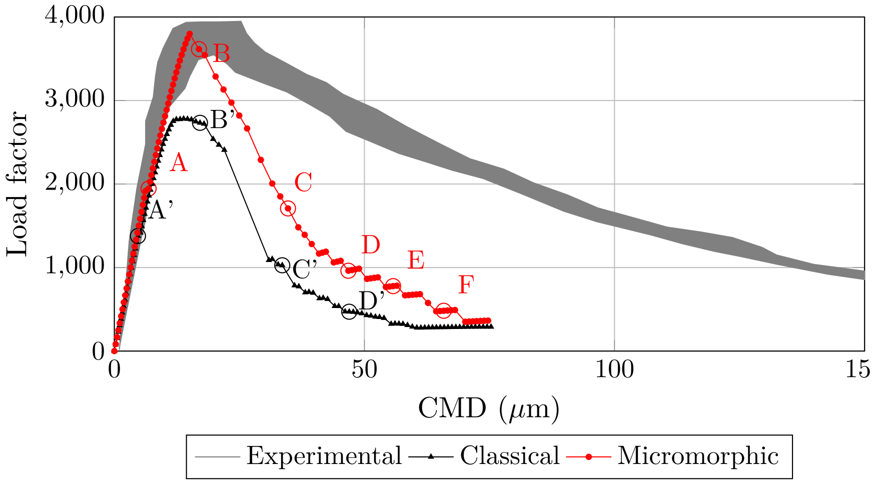

Figure 5.9: Three-point bending test: equilibrium paths

The differences between both analyses can also be observed in the damage distribution displayed in Fig. 5.10 for four steps in the nonlinear process which correspond to points A to D in the equilibrium paths presented in Fig. 5.9. The first two presented (Figs. 5.10(a) and 5.10(b)) for classical and micromorphic continuum, respectively, mark the last step after the detection of localization where the nodes in the first element are enriched. Even though the load factor for which the localization was detected is higher for the micromorphic continuum, the damage observed around the notch tip is lower than the classical continuum, pointing to a more localized phenomenon in the latter.

As the load increases the same tendency of higher values of damage is observed in Figs. 5.10(c) and 5.10(d). Following, damage for points B and B' are displayed in Figs. 5.10(e) and 5.10(f). For the classical continuum, though damage continues to develop as load increases, the discontinuity represented by the enrichment of the nodes with the Heaviside function does not continue as localization via the analysis of the classical acoustic tensor determinant is not identified in the element in front of the crack tip. The reason for this may be related to the damage tending to concentrated in the classical continuum, however this was not further studied in this work and needs more simulations to attest the hypothesis validity. Furthermore, it can be observed that for the classical continuum the damage tends to concentrate in a narrower and longer domain in front of the notch tip when compared to the micromorphic continuum. The same tendency is observed in Figs. 5.10(g) and 5.10(h) for a higher load factor. This can be credited to the known regularization properties of the micromorphic continuum due to its non-local formulation.

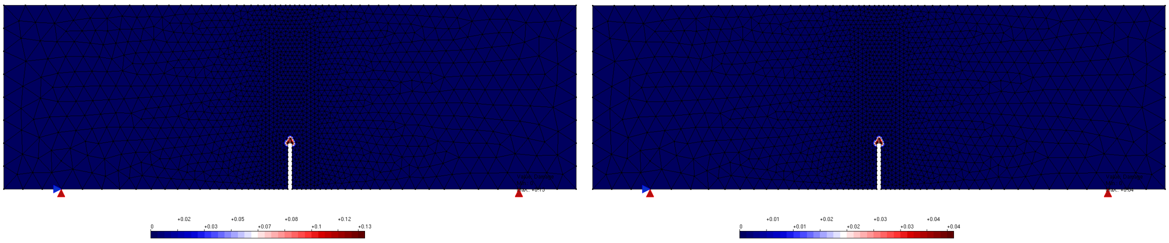

(a) Classical - A’ (b) Micromorphic - A

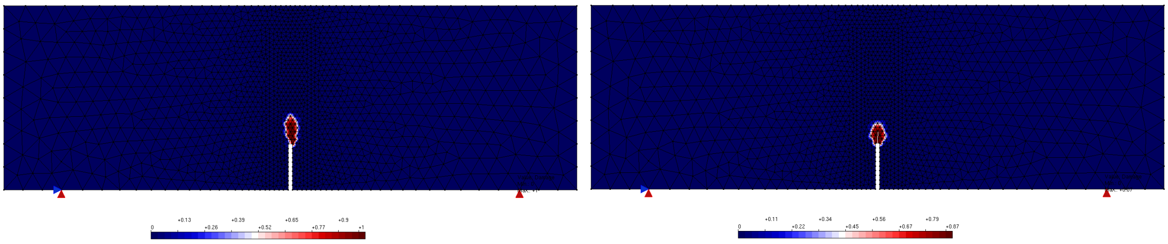

(c) Classical - B’ (d) Micromorphic - B

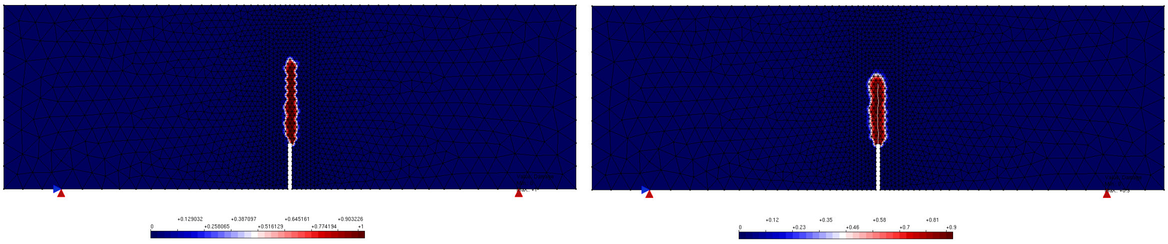

(e) Classical - C’ (f) Micromorphic - C

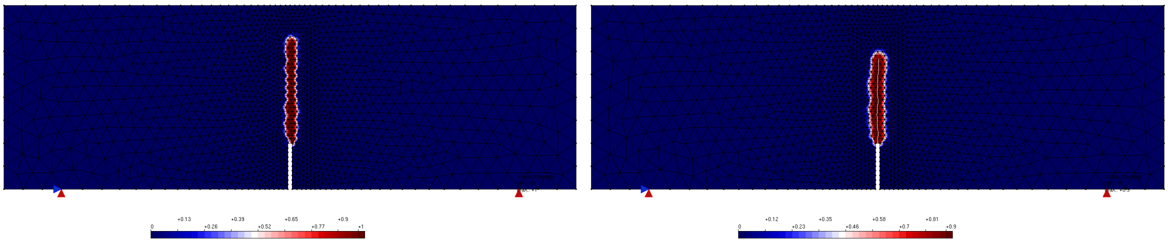

(g) Classical - D’ (h) Micromorphic - D

Figure 5.10: Three-point bending test: damage

The evolution of the discontinuity as well as the deformed shape throughout the loading process for the micromorphic continuum is illustrated in Fig. 5.11. In total, 57 nodes were enriched during the analysis, getting a total of 342 additional DOFs in the system, considering that, for a plane problem, each node in a micromorphic medium is endowed with 6 degrees of freedom (d_{u1}, d_{u2}, $d_{\phi 11}$, $d_{\phi 22}$, $d_{\phi 12}$, and $d_{\phi 21}$, as defined in Section 5.2 and Appendix A) and all DOF are enriched in the process. The discontinuity propagates vertically along the symmetry axis starting from the notch tip as expected. As previously mentioned, point A (see Fig. 5.9) marks the first step for which occurs crack nucleation. Therefore, localization is detected is the precious step, i.e., the determinant of the microscale micromorphic acoustic tensor introduced in Section 4.1.2 becomes negative. The crack propagates faster from points B to C, what corresponds to the steeper part of the descending branch. Again, this behavior is related to the choice of not considering cohesion in this study, leading to a more brittle failure.

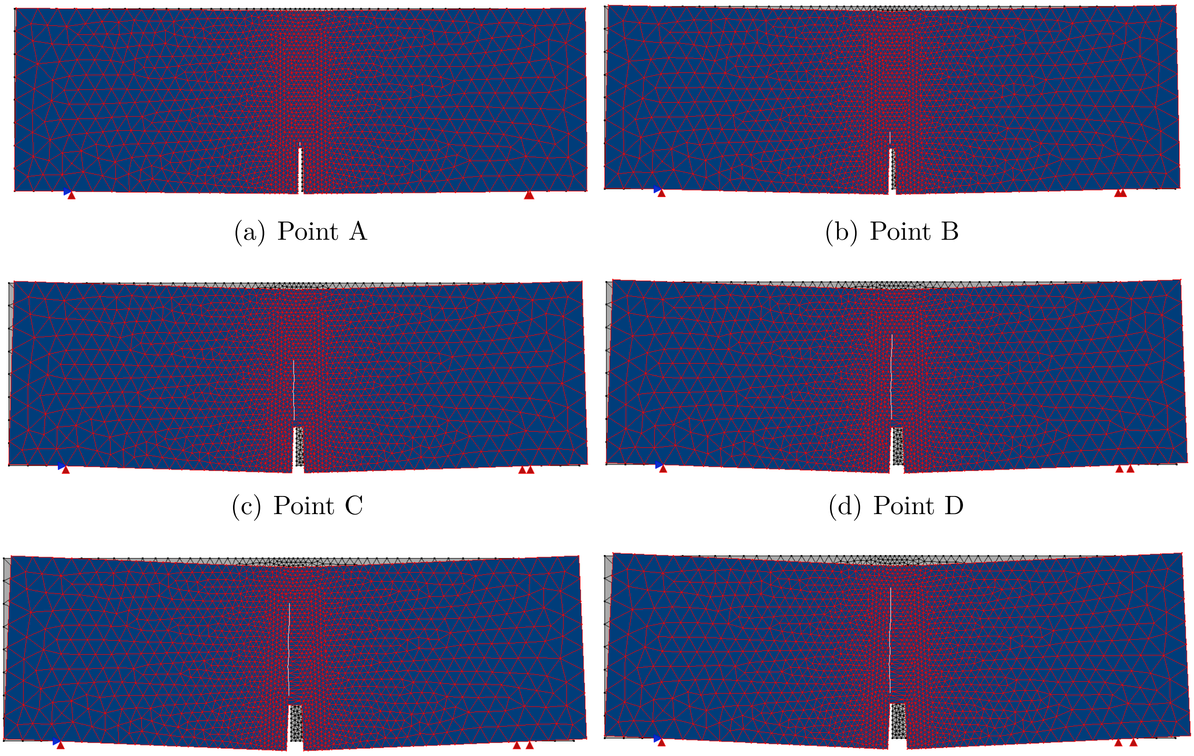
(a) Point A

(b) Point B

(c) Point C

(d) Point D

(e) Point E

(f) Point F

Figure 5.11: Three-point bending test: deformed configuration (micromorphic continuum) for points A to F

Lastly, the strain distribution for the micromorphic continuum corresponding to the component of the strain tensor $\boldsymbol{e}$ in the horizontal direction (i.e., e_{11}) is shown in Fig. 5.12. As expected for a bending test, there is a concentration of traction around the crack tip as compression develops in the upper part of the beam where the load is applied.

The results obtained for the three-point bending test demonstrate that the proposed micromorphic approach effectively captures the expected crack propagation behavior. The crack initiates at the notch tip and progresses vertically along the plane of symmetry, in agreement with experimental observations and previous numerical studies. Additionally, the adoption of the micromorphic formulation successfully mitigates mesh dependency associated with strain localization.

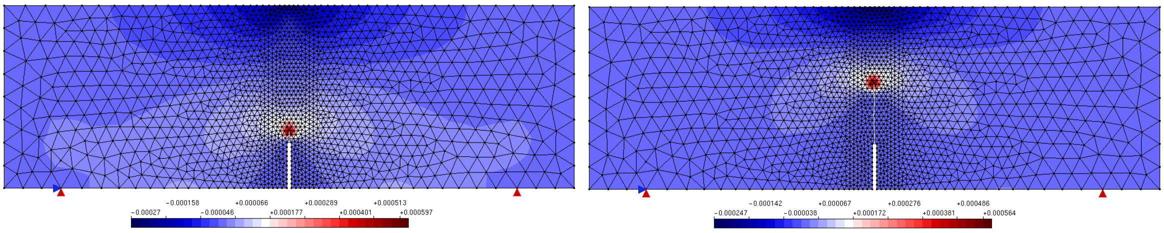

(a) Point B (b) Point C

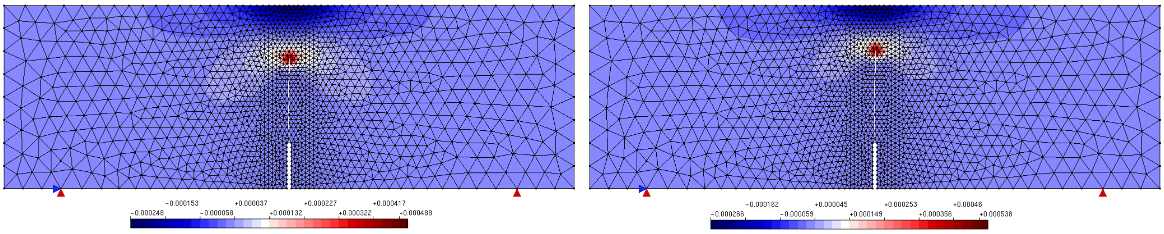

(c) Point D (d) Point E

Figure 5.12: Three-point bending test: strain e_{xx} (micromorphic continuum)

Chapter 6

Pressurized fracture

This chapter examines the problem of pressurized fractures, providing a brief overview of hydraulic fracturing and its computational modeling. It introduces the formulation of the micromorphic-XFEM framework for modeling fluid-driven crack propagation and presents numerical examples demonstrating its application.

6.1 Basic concepts

In the field of hydraulic engineering, various types of dams are commonly employed. Concrete dams undergo a number of degrading processes which could lead to significant cracking and consequently reduced lifespan. Thermal gradients (e.g., due to cement hydration), fluid-structure interaction (water pressure within fractures), and chemical attacks (as in alkali-aggregate reactions) may cause cracking. Furthermore, concrete gravity dams are known to have weaker planes and highly stressed areas, such as the interface between the dam and the underlying foundation, where cracks are prone to develop (ICOLD, 1999). In this study, only the fluid-structure interaction is of interest, in which a hydraulic loading (i.e., pressure) applied by the fluid inside the fracture causes the initiation and propagation of the fracture. The fracture process creates pathways that enable fluid movement through the concrete, thereby increasing its permeability.

With respect to the underling physics, at least three basic processes need to be considered when modeling the hydraulic fracturing process: (1) mechanical deformation around the fracture induced by the fluid pressure; (2) fluid-flow in the fracture; and (3) fracture propagation (Adachi et al., 2007). Hydraulic fracturing also involves other physical processes, often viewed as secondary in order to make the study more tractable, as leak-off, interaction with natural fractures, and heterogeneity. A brief review of the mentioned basic aspects is presented in the next paragraphs and the reader may refer to Chen et al. (2022) and the references within for a more thorough review.

The first physical aspect to be considered is the material deformation. The material surrounding a fracture could be concrete, for the case of concrete dams wherein fluid-driven fracturing can occur naturally, or rock, for the case in which hydraulic fracturing is a technique to fracture underground rock formation using pressurized fluid to extract, for example, shale gas (Adachi et al., 2007). In both cases, however, the material is highly heterogeneous and simplifying assumptions are usually introduced, as the hypothesis of a linear elastic material. To consider the effect of porosity in the solid medium, poroelasticty has been widely adopted, which is based on Biot's consolidation theory (Biot, 1941).

Following, the fluid flow within the fracture must be modeled. The simplest manner to do so is to consider an uniform pressure on the fracture surface. A more realistic approach is based on the lubrification theory and Poiseuille's law that relates the flow rate with the pressure gradient along the fracture. For the fracture propagation, linear elasticity fracture mechanics (LEFM) and cohesive zone model are usually adopted. The validity of models based on LEFM and lubrification theory is studied, among other authors, by Deb et al. (2021), in which the mentioned approach was able to describe sufficiently well the processes in controlled laboratory-scale hydraulic fracturing experiments in granite samples.

Analytical models for the hydraulic fracturing process have been developed for more than half a century, dating back to the 1950s. One of the first classical models is the PKN model proposed by Perkins and Kern (1961) and Nordgren (1972), hence the name. This model applied theory of elasticity to compute the fracture width as a function of the local fluid pressure, assuming that the height of the fracture is constant along the propagation direction. The PKN model is applicable when the fracture length is much greater than the height as, for each vertical cross section, a plane strain state is assumed. For the case in which the restriction to only constant height for the fracture is removed, the cell-based P3D model is obtained (Cleary, 1980) that features a 3D fracture geometry and 1D fluid flow. A further improvement of the PKN model is presented by the PL3D model that considers a 2D fluid flow and a planar fracture (Clifton and Abou-Sayed, 1979).

Unlike the PKN model, the KGD (Khristianovic-Geertsma-de Klerk) model, based on Khristianovic and Zheltov (1955) and Geertsma and De Klerk (1969), imposes a plane strain condition on the horizontal section. Therefore, this model is suitable when the height is significantly greater than its length. A study by Sneddon (1946) examines a model for penny-shaped hydraulic fractures with constant fluid pressure. This radial model bears similarities to the KGD model, except that it replaces the plane strain assumption with the axisymmetric assumption

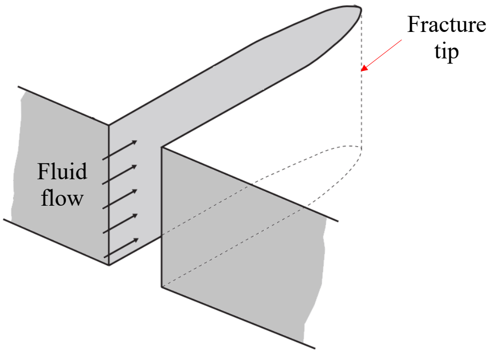

Figure 6.1: Schematic showing KGD fracture geometry (adapted from Adachi et al., 2007)

The classical models discussed have limitations regarding the propagation direction of hydraulic fractures, as they are restricted to straight lines or planar planes. Additionally, these models do not fully consider the influence of natural fractures. As a result, more realistic numerical models have been developed in the literature. Based on the discretization method adopted for the media, three methods are commonly identified: *continuum-based* methods, *discontinuum-based* methods, and *hybrid continuum/discontinuum* methods (Chen et al., 2022). In the context of this study, we will focus on presenting some continuum-based models applied to the discrete approach to crack representation, as they are particularly relevant.

In *continuum-based* methods, considering the discrete crack approach, the FEM has long been used for simulating hydraulic fracturing. One remarkable work in the field is presented by Boone and Ingraffea (1990) that applied a KGD-type model to simulate two-dimensional hydraulic fracture propagation in a poroelastic media. A finite element approximation is used for the poroelastic medium and a finite difference method (FDM) for modeling fluid along the fracture following Poiseulle's law and the continuity equation. The fracture dimensions are determined using a generalized cohesive crack model (Dugdale-Barenblatt fracture mechanics model) presented by Boone et al. (1986).

Also considering a discrete cohesive crack model, Secchi and Schrefler (2012) presented a method for the simulation of 3D hydraulic fractures in fully saturated porous media. The crack propagates along the face of the elements around the fracture tip under the assumption of mode I crack opening, requiring a continuous updating of the mesh geometry. For the liquid phase, the validity of Poiseuille's law is also assumed. This model was validated with a concrete dam example proposed as a benchmark by ICOLD (1999).

Considering the limitations of the FEM approach in modeling fracture propagation, specially related to difficulties in remeshing, XFEM/GFEM has also been applied in simulating hydraulic fracturing (Gupta and Duarte, 2014, Roth et al., 2020).As highlighted by Chen et al. (2022), XFEM provides an effective representation of sharp fracture surfaces and enables accurate calculations of fracture width while circumventing the need for remeshing. Different from FEM, XFEM captures crack deformation via discontinuous fields. The displacement approximation, as discussed in Chapter 5, is formulated by applying enrichment functions as the Heaviside function. Additionally, near-tip asymptotic field functions can be incorporated to enhance the accuracy of displacement fields around crack tips.

The application of XFEM to pressurized fractures was first introduced by Lecampion (2009) and Ren et al. (2009), who employed the two-dimensional KGD model for hydraulic fracturing. Specifically, Ren et al. (2009) assumed a uniform constant fluid pressure to model hydraulic fractures in gravity dams. Further developments have included cohesive zone models and fracture propagation in fluid-saturated porous media (Mohammadnejad and Khoei, 2013). Additionally, XFEM has been extended to three-dimensional non-planar hydraulic fracture propagation (Gupta and Duarte, 2014, 2018).

Despite its advantages, XFEM/GFEM has certain limitations, particularly when dealing with complex fracture topologies, such as the interaction between pressurized fractures and natural fractures (Ren et al., 2009).

In addition to the discussed continuum-based models, other discrete numerical methods have been used for simulating fracture propagation in hydraulic fractures. These methods include BEM, and peridynamics. However, since this work primarily focuses on finite element applications, readers are encouraged to refer to Chen et al. (2022) for a review of these numerical methods.

To avoid the need for remeshing, which is often necessary for discrete crack models, smeared approaches have also been explored, in which both the fracture and the surrounding media are represented by continuous elements but in different states. Considering FEM applications, Li et al. (2012) and Wangen (2013) can be mentioned.

Another rapidly developing approach in hydraulic fracturing modeling is the phase-field method (PFM) (Bourdin et al., 2012, Miehe and Mauthe, 2016, Lee et al., 2016, Ferreira et al., 2024). This approach offers several advantages, including the ability to represent cracks without the need for remeshing, the capability to model complex interactions between pressurized and natural fractures, and the straightforward incorporation of material heterogeneity into the solution scheme. However, despite these benefits, PFM simulations are computationally expensive, requiring extremely fine meshes and small time steps to achieve accurate results (Chen et al., 2022).

The hydraulic fracturing process can also be modeled using discontinuum-based models that describe the medium as a discrete system of deformable (DEM) or rigid blocks (Rigid-Body-Spring Network - RBSN) linked by special elements. These models are specially suitable for microscale analysis as the material grains can be represented (Chen et al., 2022).

Considering that, in some problems, there is a progressive failure of the material, transitioning from a continuous to a discontinuous model, the combined finite-discrete element method (FDEM) has been developed by Munjiza (2004). This technique begins with a representation of the medium as a continuum using finite elements, and then enable a progressive transition from a continuous representation to a discontinuous one by incorporating new discontinuities (Lisjak et al., 2017). Since then, numerous works have explored this method due to its applicability to progressive fracturing (Chen et al., 2022).

Applications of generalized continua in modeling pressurized fractures is not well explored in the literature. Although, some studies related to hydro-mechanical analysis can be mentioned. Considering unsaturated granular material, Wan and Li (2015) proposed a multi-scale hydro-mechanical analysis with a macroscopic Biot-Cosserat continuum simulated with FEM and a fine-scale simulated with DEM. Also considering the association of Biot's model and the Cosserat continuum, Giorgio et al. (2020) proposed a novel nonlinear, elastic bi-dimensional model that is able to account for the microstructure of materials composed by grains embedded in a porous matrix.

Using Finite Element squared (FE^2) method, van den Eijnden et al. (2016) and van den Eijnden et al. (2017) presented an approach for modeling hydro-mechanical coupling in which the macroscopic constitutive behavior is derived from the interaction between a solid granular micro-structure and the pore fluid. As the work mentioned proposed to model materials with softening, a local second gradient paradigm is used. This generalized theory can be interpreted as a specific case of micromorphic medium in which the micro-kinematic gradient is constrained to be equal to the macro displacement gradient.

Considering the lack of studies applying micromorphic theory to the modeling of pressurized fractures, this work proposes an extension of the XFEM approach, as detailed in Chapter 5, by incorporating a constant pressure load to simulate fluid-driven crack propagation.

6.1.1 Propagation regimes

The behavior of hydraulic fracturing can be categorized into different regimes based on the dominant energy dissipation and the fluid storage mechanisms. Energy dissipation is primarily controlled by either the fracture toughness of the medium or the viscosity of the injected fluid. A dimensionless stiffness parameter, which accounts for the Young's modulus of the material, fluid viscosity, and injection rate, helps distinguish between these two dissipation regimes.

Regarding storage, two key mechanisms are considered: fluid storage within the fracture itself and fluid leak-off into the surrounding porous matrix. The relative significance of these processes is quantified by a dimensionless leak-off coefficient (Adachi and Detournay, 2008, Carrier and Granet, 2012). Based on the values of these dimensionless parameters, the crack propagation process can be classified into four distinct regimes: storage-toughness, storage-viscosity, leak-off-toughness, and leak-off-viscosity (Bao et al., 2015).

Fracture behavior varies significantly depending on the regime considered in the analysis. For instance, in the case of multiple hydraulic fractures, Dontsov and Suarez-Rivera (2020) points out that fractures in the viscosity-dominated regime are minimally influenced by the stress field generated by adjacent cracks and tend to grow predominantly in a radial pattern. In contrast, fractures propagating in the toughness-dominated regime exhibit different geometries and are significantly affected by the stress field from other cracks. The propagation regime also influences how hydraulic fractures interact with natural fractures, leading to different propagation patterns, as noted by Rueda et al. (2020).

This study focuses on low-permeability media, where fluid leak-off across the fracture faces is negligible. Furthermore, the fluid is assumed to have a viscosity similar to that of water. Under these conditions, the fracture regime is storage-toughness dominated. The problem formulation, presented in Section 6.2, assumes that the fluid pressure remains constant along the fracture faces, although it is time-dependent, i.e, incremental in relation to the time step. These assumptions are particularly valid for deep reservoirs and low-viscosity fluids, where pressure remains nearly uniform along the fracture faces, especially near the wellbore (Gupta and Duarte, 2014). Additionally, under these conditions, the fluid and fracture fronts are assumed to coincide, meaning that the fluid lag is negligible.

6.2 Formulation

Considering initially a domain $\mathcal{V}$ containing an edge crack described by $\partial\mathcal{V}_d$ as illustrated in Fig. 6.2(a). The crack faces $\partial\mathcal{V}_d^+$ and $\partial\mathcal{V}_d^-$ are distinguished as shown in Fig. 6.2(b), such that $\partial\mathcal{V}_d = \partial\mathcal{V}_d^+ \cup \partial\mathcal{V}_d^-$ and with the normals to $\partial\mathcal{V}_d^+$ and $\partial\mathcal{V}_d^-$ by $\boldsymbol{n}^+$ and $\boldsymbol{n}^-$, respectively. A constant fluid pressure $\boldsymbol{p}$ is imposed on the crack surface, described by $\boldsymbol{p}^+$ and $\boldsymbol{p}^-$ on $\partial\mathcal{V}_d^+$ and $\partial\mathcal{V}_d^-$, respectively.

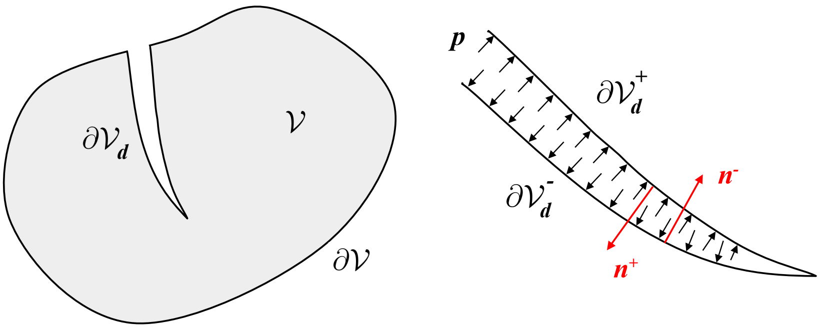

(a) Domain (b) Crack

Figure 6.2: Notation for the cracked domain and for the crack (Ren et al., 2009)

For the domain including a crack as shown in Fig. 6.2(a), $\boldsymbol{n}^- = -\boldsymbol{n}^+ = \boldsymbol{n}$ is defined and the hypotheses of small strains and displacements is adopted. Then, based on Eq.

(3.22), Eq. (3.24) is rewritten including the water pressures $\boldsymbol{p}^+$ and $\boldsymbol{p}^-$ on the crack surfaces

$$\begin{aligned} \delta^{(1)}V = & - \int_{\mathcal{V}} (\rho f_l \delta u_l + \rho l_{lm} \delta\phi_{lm})\, dv - \int_{\partial\mathcal{V}} \left(\hat{t}_{(\boldsymbol{n})l}\delta u_l + \hat{m}_{(\boldsymbol{n})lm}\delta\phi_{lm}\right) ds - \\ & - \int_{\partial\mathcal{V}_d^+} p_l^+ \delta u_l^+ ds - \int_{\partial\mathcal{V}_d^-} p_l^- \delta u_l^- ds \end{aligned} \tag{6.1}$$

Since $p_l = p_l^+ = -p_l^-$ on the crack surfaces, Eq. (6.1) can be written as

$$\begin{aligned} \delta^{(1)}V = & - \int_{\mathcal{V}} (\rho f_l \delta u_l + \rho l_{lm} \delta\phi_{lm})\, dv - \int_{\partial\mathcal{V}} \left(\hat{t}_{(\boldsymbol{n})l}\delta u_l + \hat{m}_{(\boldsymbol{n})lm}\delta\phi_{lm}\right) ds - \\ & - \int_{\partial\mathcal{V}_d} p_l(\delta u_l^+ - \delta u_l^-) ds \end{aligned} \tag{6.2}$$

By defining $\delta w_l = \delta u_l^+ - \delta u_l^-$, where δw_l is the separation between the two surfaces of the crack, Eq. (6.2) may be rewritten as

$$\begin{aligned} \delta^{(1)}V = & - \int_{\mathcal{V}} (\rho f_l \delta u_l + \rho l_{lm} \delta\phi_{lm})\, dv - \int_{\partial\mathcal{V}} \left(\hat{t}_{(\boldsymbol{n})l}\delta u_l + \hat{m}_{(\boldsymbol{n})lm}\delta\phi_{lm}\right) ds - \\ & - \int_{\partial\mathcal{V}_d} (p_{(\boldsymbol{n})l}\delta w_l) ds \end{aligned} \tag{6.3}$$

The equilibrium condition in Eq. (5.15) is then restructured as

$$\begin{aligned} \delta^{(1)}\Pi = & \int_{\mathcal{V}} \left(\delta\boldsymbol{\epsilon}^T\boldsymbol{t} + \delta\boldsymbol{e}^T\boldsymbol{s} + \delta\boldsymbol{\gamma}^T\boldsymbol{m}\right) dv - \\ & - \int_{\mathcal{V}} \left(\delta\boldsymbol{u}^T\rho\boldsymbol{f} + \delta\boldsymbol{\phi}^T\rho\boldsymbol{l}\right) dv - \int_{\partial\mathcal{V}} \left(\delta\boldsymbol{u}^T\hat{\boldsymbol{t}}_{(\boldsymbol{n})} + \delta\boldsymbol{\phi}^T\hat{\boldsymbol{m}}_{(\boldsymbol{n})}\right) ds - \\ & - \int_{\partial\mathcal{V}_d} (\delta\boldsymbol{w}^T\boldsymbol{p}_{(\boldsymbol{n})}) ds = 0 \end{aligned} \tag{6.4}$$

For the element including enrichment function H, based on Eq. (5.3), the separation between surfaces of the crack observing only macro displacements is

$$\boldsymbol{w} = \boldsymbol{n}(\boldsymbol{u}^+ - \boldsymbol{u}^-) = \boldsymbol{n}(\boldsymbol{N}\boldsymbol{d}'_{\boldsymbol{u}}) \tag{6.5}$$

Hence, Eq. (5.16) can be rewritten as

$$
\begin{aligned}
\delta^{(1)}\mathbf{\Pi} = \int_{\mathcal{V}} \Big[\delta \boldsymbol{d}_{\boldsymbol{u}}^{T} \boldsymbol{B}_{\boldsymbol{u}}^{T} + \mathcal{H}\delta \boldsymbol{d}_{\boldsymbol{u}}^{\prime T} \boldsymbol{B}_{\boldsymbol{u}}^{T} + \delta \boldsymbol{d}_{\boldsymbol{u}}^{\prime T} \boldsymbol{N}^{T} \left(\boldsymbol{\nabla}^{T}\mathcal{H}\right) - \delta \boldsymbol{d}_{\boldsymbol{\phi}}^{T} \bar{\boldsymbol{N}}_{\boldsymbol{T}}{}^{T} - \mathcal{H}\delta \boldsymbol{d}_{\boldsymbol{\phi}}^{\prime T} \bar{\boldsymbol{N}}_{\boldsymbol{T}}{}^{T}\Big] \\
\Big\{\boldsymbol{A}\Big[\boldsymbol{B}_{\boldsymbol{u}}\boldsymbol{d}_{\boldsymbol{u}} + \mathcal{H}\boldsymbol{B}_{\boldsymbol{u}}\boldsymbol{d}_{\boldsymbol{u}}^{\prime} + (\boldsymbol{\nabla}\mathcal{H})\,\boldsymbol{N}\boldsymbol{d}_{\boldsymbol{u}}^{\prime} - \bar{\boldsymbol{N}}_{\boldsymbol{T}}\boldsymbol{d}_{\phi} - \mathcal{H}\bar{\boldsymbol{N}}_{\boldsymbol{T}}\boldsymbol{d}_{\phi}^{\prime}\Big] + \boldsymbol{E}\Big[\bar{\boldsymbol{N}}_{\boldsymbol{S}}\boldsymbol{d}_{\phi} + \mathcal{H}\bar{\boldsymbol{N}}_{\boldsymbol{S}}\boldsymbol{d}_{\phi}^{\prime}\Big]\Big\}\, dv \\
+ \int_{\mathcal{V}} \left(\delta \boldsymbol{d}_{\boldsymbol{\phi}}^{T} \bar{\boldsymbol{N}}_{\boldsymbol{S}}{}^{T} + \mathcal{H}\delta \boldsymbol{d}_{\boldsymbol{\phi}}^{\prime T} \bar{\boldsymbol{N}}_{\boldsymbol{S}}{}^{T}\right) \Big\{\boldsymbol{E}^{T}\left[\boldsymbol{B}_{\boldsymbol{u}}\boldsymbol{d}_{\boldsymbol{u}} + \mathcal{H}\boldsymbol{B}_{\boldsymbol{u}}\boldsymbol{d}_{\boldsymbol{u}}^{\prime} + (\boldsymbol{\nabla}\mathcal{H})\,\boldsymbol{N}\boldsymbol{d}_{\boldsymbol{u}}^{\prime} - \right. \\
\left. \bar{\boldsymbol{N}}_{\boldsymbol{T}}\boldsymbol{d}_{\phi} - \mathcal{H}\bar{\boldsymbol{N}}_{\boldsymbol{T}}\boldsymbol{d}_{\phi}^{\prime}\right] + \boldsymbol{B}\Big[\bar{\boldsymbol{N}}_{\boldsymbol{S}}\boldsymbol{d}_{\phi} + \mathcal{H}\bar{\boldsymbol{N}}_{\boldsymbol{S}}\boldsymbol{d}_{\phi}^{\prime}\Big]\Big\}\, dv \\
+ \int_{\mathcal{V}} \Big[\delta \boldsymbol{d}_{\boldsymbol{\phi}}^{T} \boldsymbol{B}_{\boldsymbol{\phi}}^{T} + \mathcal{H}\delta \boldsymbol{d}_{\boldsymbol{\phi}}^{\prime T} \boldsymbol{B}_{\boldsymbol{\phi}}^{T} + \delta \boldsymbol{d}_{\boldsymbol{\phi}}^{\prime T} \bar{\boldsymbol{N}}^{T} \left(\boldsymbol{\nabla}^{T}\mathcal{H}\right)\Big] \Big\{\boldsymbol{C}\Big[\boldsymbol{B}_{\phi}\boldsymbol{d}_{\phi} + \mathcal{H}\boldsymbol{B}_{\phi}\boldsymbol{d}_{\phi}^{\prime} + (\boldsymbol{\nabla}\mathcal{H})\,\bar{\boldsymbol{N}}\boldsymbol{d}_{\phi}^{\prime}\Big]\Big\}\, dv \\
- \int_{\mathcal{V}} \Big[\left(\delta \boldsymbol{d}_{\boldsymbol{u}}^{T} \boldsymbol{N}^{T} + \mathcal{H}\delta \boldsymbol{d}_{\boldsymbol{u}}^{\prime T} \boldsymbol{N}^{T}\right) \rho \boldsymbol{f} + \left(\delta \boldsymbol{d}_{\boldsymbol{\phi}}^{T} \bar{\boldsymbol{N}}^{T} + \mathcal{H}\delta \boldsymbol{d}_{\boldsymbol{\phi}}^{\prime T} \bar{\boldsymbol{N}}^{T}\right) \rho \boldsymbol{l}\Big]\, dv \\
- \int_{\partial\mathcal{V}} \Big[\left(\delta \boldsymbol{d}_{\boldsymbol{u}}^{T} \boldsymbol{N}^{T} + \mathcal{H}\delta \boldsymbol{d}_{\boldsymbol{u}}^{\prime T} \boldsymbol{N}^{T}\right) \hat{\boldsymbol{t}}_{(\boldsymbol{n})} + \left(\delta \boldsymbol{d}_{\boldsymbol{\phi}}^{T} \bar{\boldsymbol{N}}^{T} + \mathcal{H}\delta \boldsymbol{d}_{\boldsymbol{\phi}}^{\prime T} \bar{\boldsymbol{N}}^{T}\right) \hat{\boldsymbol{m}}_{(\boldsymbol{n})}\Big]\, ds - \\
- \int_{\partial\mathcal{V}_d} (\delta \boldsymbol{d}_{\boldsymbol{u}}^{\prime T} \boldsymbol{N}^{T} \boldsymbol{n}^{T}) \boldsymbol{p}_{(\boldsymbol{n})} ds = 0
\end{aligned}
\tag{6.6}
$$

Finally, with some rearranging, the water pressure contribution in the problem can be defined as

$$
\boldsymbol{f}_{eq,\boldsymbol{p}} = \int_{\partial\mathcal{V}_d} \boldsymbol{N}^{T} \boldsymbol{n}^{T} \boldsymbol{p}_{(\boldsymbol{n})} ds \tag{6.7}
$$

and added to the system presented in Eq. (5.17) to the external forces term $\boldsymbol{f}_{eq,\boldsymbol{u}^{\prime}}$ related to the macro additional displacements $\boldsymbol{u}^{\prime}$

$$
\boldsymbol{f}_{eq,\boldsymbol{u}^{\prime}} = \int_{\mathcal{V}} \mathcal{H}\boldsymbol{N}^{T} \rho \boldsymbol{f} dv + \int_{\partial\mathcal{V}} \mathcal{H}\boldsymbol{N}^{T} \hat{\boldsymbol{t}}_{(\boldsymbol{n})} ds + \int_{\partial\mathcal{V}_d} \boldsymbol{N}^{T} \boldsymbol{n}^{T} \boldsymbol{p}_{(\boldsymbol{n})} ds \boldsymbol{N}^{T} ds \tag{6.8}
$$

Therefore, to include the contribution of a constant pressure load to micromorphic enriched-FEM approach, the term presented in Eq. (6.8) must be added to the system. To accommodate this change, some alterations related to the nonlinear process were also necessary considering that, even though the pressure remains constant along the crack surface, it is time-dependent and it is incrementally increased throughout the analysis.

6.3 Numerical simulations

Three models are studied in this section adopting the formulation proposed that considers a constant pressure load on the crack surface. Crack nucleation and propagation are determined based on the microscale localization analysis detailed in Chapter 4. The examples explore, regarding pressurized fractures, crack opening displacement, interaction with natural fractures, and combination of pressure with a traction loading condition.

6.3.1 Static crack

To validate the proposed model, a two-dimensional static case in plane stress is considered. An infinite domain composed of a homogeneous isotropic material with Young's modulus E and Poisson ratio ν is analyzed, containing a single preexisting crack $\partial\mathcal{V}_d$ of length $2l_o$. Assuming that the stress and strain fields tend to zero at infinity, an exact expression can be derived for the boundary displacement of the crack surface when subjected to a uniform pressure force p (refer to Sneddon and Lowengrub (1969) and Bourdin et al. (2012)). Defining $E' = E/(1-\nu^2)$, the follow expression holds for $l_0 \leq x \leq l_0$

$$u^+(x) = \frac{2pl_0}{E'}\left(1 - \frac{x^2}{l_0^2}\right)^{1/2} \tag{6.9}$$

considering that $u^-(x) = u^+(x)$. In order to compare the analytical expression of the crack opening displacement to the numerical solution here proposed, a finite square domain of size 4×4 with a centered crack of length $2l_0 = 0.4$, unit Young's modulus and Poisson's ratio $\nu = 0.2$ was modeled. The adopted boundary conditions and geometry are illustrated in Fig. 6.3. Three meshes composed of quadrilateral elements of 4 nodes were used as shown in Fig. 6.4 wherein the initial crack, introduced using the XFEM micromorphic model, crosses 2, 4, and 8 elements in meshes 1, 2, and 3, respectively. A constant internal pressure $p = 10^{-3}$ is applied to the crack surface and its opening is computed from the additional macroscale displacements of the enriched nodes considering the discontinuous term in Eq. (5.3).

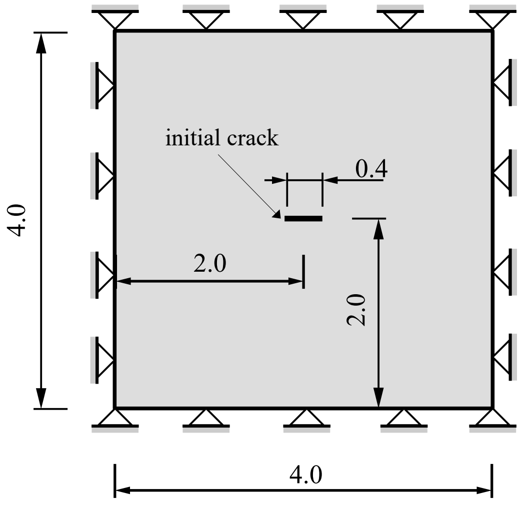

Figure 6.3: Static crack: geometry and boundary conditions

The crack opening displacement along the crack obtained for this analysis is presented in Fig. 6.5 for the three meshes in comparison to the analytical result given by Eq. (6.9). The approximation of the open displacement converge to the analytical solution with mesh refinement, attesting the model proper response. The results for the displacement

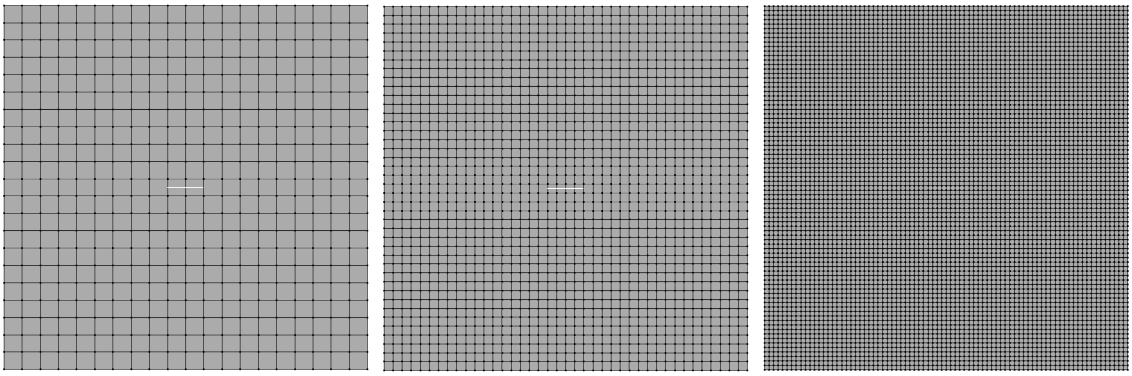

(a) Mesh 1 (b) Mesh 2 (c) Mesh 3

Figure 6.4: Static crack: meshes

in the y direction computed for the additional degrees of freedom d'_y used for computing the crack opening as well as the deformed shape are presented in Fig. 6.6. Once more, the results are in accordance with the expected behavior for a pressurized fracture.

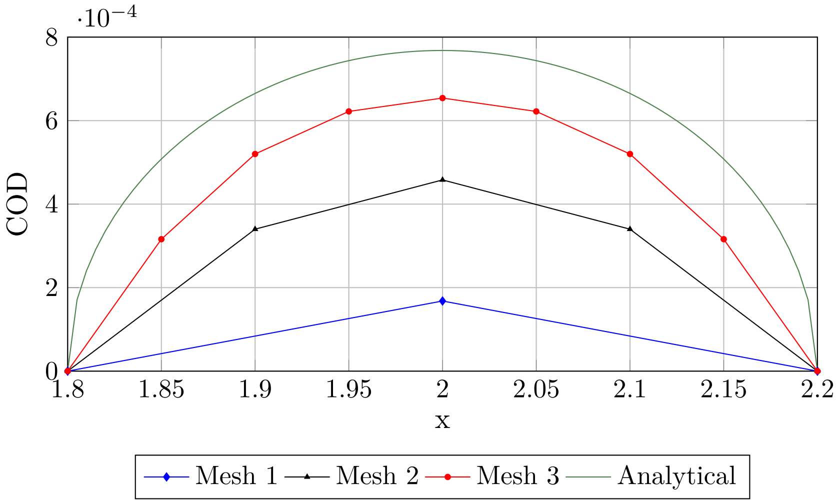

Figure 6.5: Static crack: crack opening displacement (COD)

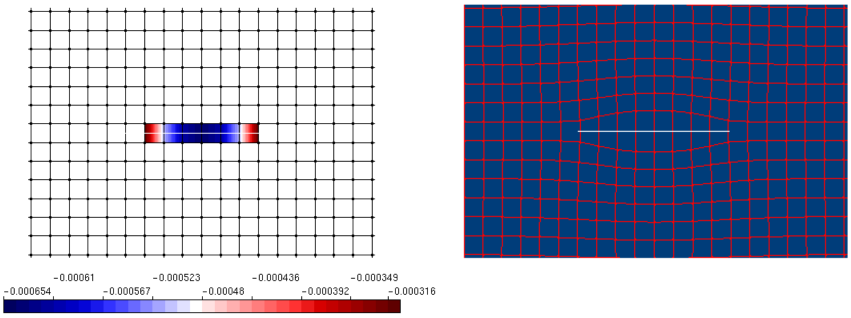

(a) Additional displacement d'_y for the enriched nodes along the crack

(b) Deformed shape

Figure 6.6: Static crack: results for mesh 3

6.3.2 Interaction with natural fracture

The second example involves the propagation of a pressurized fracture in a micromorphic medium in the presence of a pre-existing natural fracture. Natural fractures can greatly impact the propagation of a pressurized fracture as it deflect, penetrate, or stop propagating when intersecting with weak planes. Several factors influence the interaction between pressurized fractures and natural fractures, including the in-situ stress conditions, fluid pressure, injection rate, and the position and properties of natural fractures, such as their inclination and mechanical characteristics (Cruz, 2018, Li et al., 2020).

The adopted geometry in this example is similar to that of the static crack example, differing only in the presence of a natural fracture, as shown in Fig. 6.7(a). The most refined mesh used in the previous example is employed here (Fig. 6.4(c)), consisting of linear quadrilateral elements with a size of 0.05.

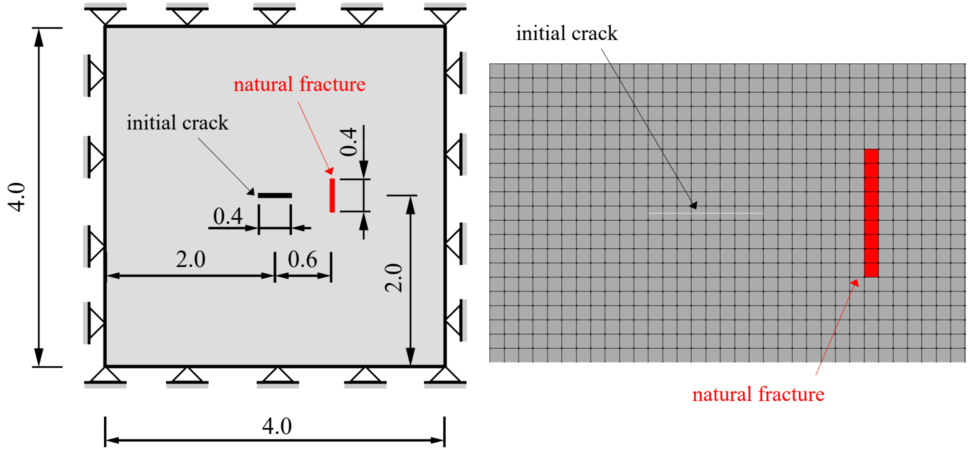

(a) Geometry (b) Mesh detail

Figure 6.7: Interaction with natural fracture: problem setting and detail of the adopted mesh

As illustrated in Fig. 6.7(a), the model, under plane stress conditions, consists of a quadrilateral domain with unit thickness, a horizontal pressurized crack at its center, and a perpendicular natural fracture of same length. The analysis is carried out over 44 load steps, with an increasing fluid pressure defined as $p = 2 \times 10^{-4} \Delta t$, where Δt represents the analysis step. The micromorphic medium is characterized by the following dimensionless material parameters: Young's modulus $E = 1.0$ and Poisson's ratio $\nu = 0.2$. The damage evolution follows the micromorphic Mazars-Lemaitre model with a linear damage law (Eq. 5.31), where the parameters are set to $K_0 = 0.01$ and $K_f = 0.1$.

The initial crack is modeled using XFEM, while the natural fracture is represented as a weakened region, highlighted in Fig. 6.7(b), considering that a natural fracture is not necessarily always open (Li et al., 2022). The elements within this weakened region have the same material properties as the rest of the domain, except for the initial deformation threshold, which is set to 10% of the domain value ($K_0 = 0.001$). Crack propagation is analyzed at the material points of the elements at both ends of the crack tip. When localization is detected using the microscale localization criterion, the crack is inserted in a direction that deviates by no more than five degrees from the previous one.

The crack propagation results are presented in Fig. 6.8. Localization is first detected at step 38, initiating crack propagation at step 39 under a pressure of $p = 7.8 \times 10^{-3}$. The crack propagates symmetrically until step 43. At steps 43 and 44, the right-side crack branch tends to deviate downward as it approaches the natural fracture, altering the fracture trajectory. The analysis becomes unstable when both fractures tend to intersect.

These results indicate that the presence of the natural fracture influenced crack initiation and propagation, leading to the trajectory deviation. However, further studies are necessary to refine the proposed approach and improve its ability to capture the interaction between pressurized and natural fractures. Additionally, further investigation is required to determine why the crack does not propagate horizontally toward the natural fracture as expected, given the problem's symmetry.

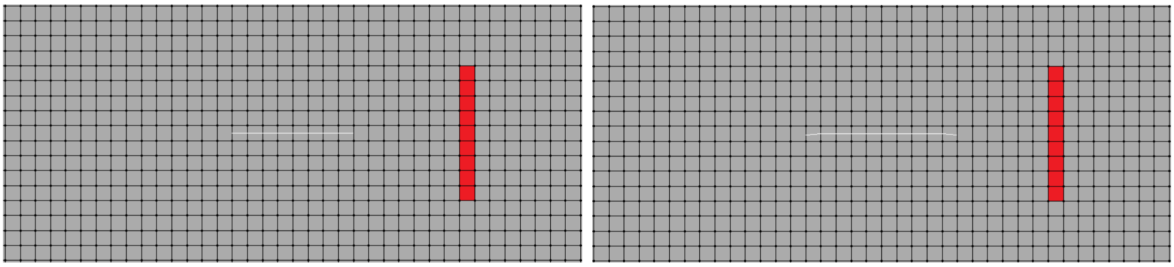

(a) Load step 39 ($p = 7.8 \times 10^{-3}$) (b) Load step 40 ($p = 8.0 \times 10^{-3}$)

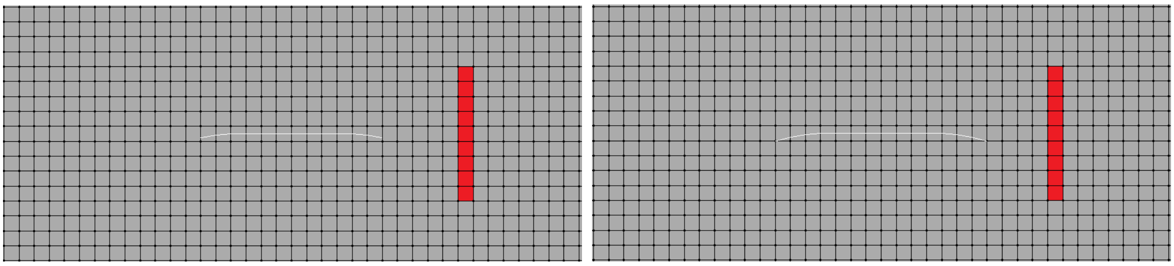

(c) Load step 41 ($p = 8.2 \times 10^{-3}$) (d) Load step 42 ($p = 8.4 \times 10^{-3}$)

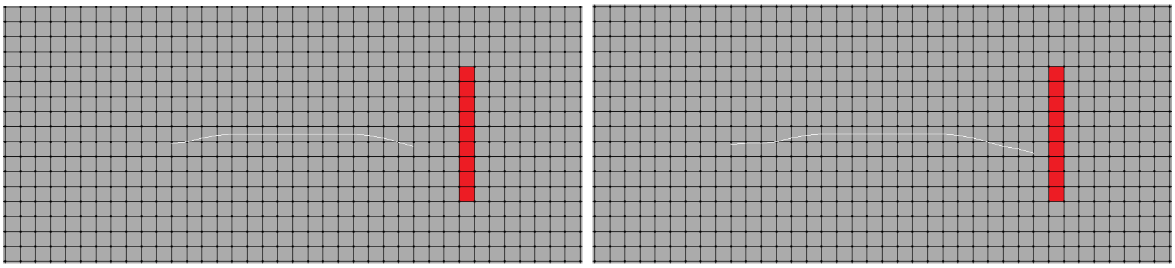

(e) Load step 43 ($p = 8.6 \times 10^{-3}$) (f) Load step 44 ($p = 8.8 \times 10^{-3}$)

Figure 6.8: Interaction with natural fracture: crack propagation

6.3.3 Notched bi-material tensile test

The third and last example of this section studies the notched bi-material tensile test (Molnár and Gravouil, 2017). As illustrated in Fig. 6.9(a), this example, modeled in plane strain, involves two materials: Material 1 with Young's modulus $E = 377$ kN/mm^2 and Poisson's ratio $\nu = 0.3$ and Material 2 ten times weaker presenting Young's modulus $E = 37.7$ kN/mm^2.

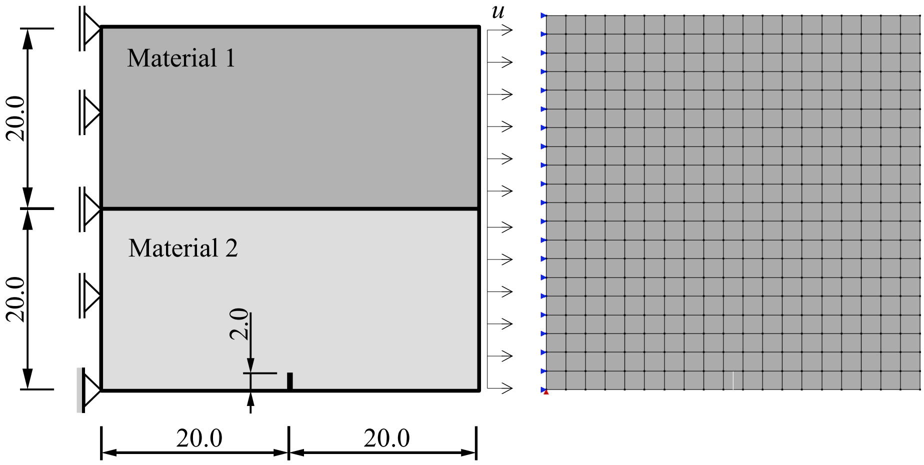

(a) Geometry (b) Mesh

Figure 6.9: Notched bi-material tensile test: geometry (dimensions in mm), boundary conditions, loading, and mesh

The finite element model is composed of 380 quadrilateral elements, each with four nodes, arranged in a grid of 20 elements along the vertical direction and 19 along the horizontal, as depicted in Fig. 6.9(b). Using this mesh configuration, the initial crack can be positioned at the center of the middle element in the bottom edge and extends across its entire length using the XFEM approach.

The test was conducted, initially, considering a traction load applied to the right side of the problem and, subsequently, adding a pressure load in the crack surface with magnitude $p = 10^{-3}$ kN/mm^2. The Mazars-Lemaitre damage model (Eq. (3.65) was employed associated to a linear damage law (Eq. (5.31)) considering $K_0 = 0.00225$ and $K_f = 0.081$ for both materials. For the nonlinear analysis, the displacement control method is adopted with an increment of 2×10^{-4} mm in the horizontal displacement of the loaded face and a tolerance of 10^{-4} for convergence. All nodes in the loaded face are restricted so they present the same horizontal displacement and its is imposed a maximum direction deviation of 30° from a crack propagating in a new element in comparison to the last propagating direction.

The results for the load factor versus the horizontal displacement of the loaded face are presented in Fig. 6.10, where micromorphic and classical models are compared, both using the XFEM approach. Analyzing the micromorphic results (see Fig. 6.10(b)), a decrease in the load factor is observed when the pressure load is applied to the crack surface. This outcome is consistent with the method adopted in the nonlinear analysis, as an increase in the load factor also results in a proportional increase in the applied pressure load. As noted, the localization detection and, consequently, the crack propagation starts earlier in the model considering the pressure load.

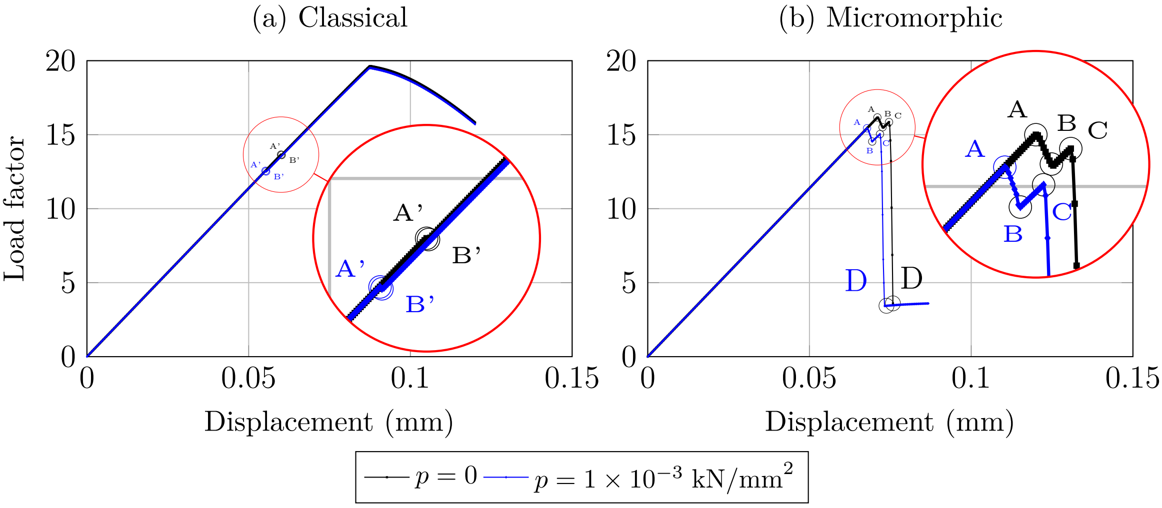
(a) Classical (b) Micromorphic

Figure 6.10: Notched bi-material tensile test: load factor versus horizontal displacement

For the classical model, the same behavior is not observed as the crack does not entirely propagate through the model height, as it is latter be presented. Hence, as most of the load is carried by the harder material (Material 2 in Fig. 6.9(a)), when fracture and damage occurs in Material 1, the overall response does not change significantly. The response does change when Material 2 experiences damage. Furthermore, the difference between the response with and without pressure load is not as significant, because, as the crack does not propagate, the contribution of the pressure load on the crack surface is inferior to that using the micromorphic continuum.

Four points of interest (A, B, C, and D) along the micromorphic equilibrium path were identified and used as reference for analyzing the cracking process which is presented in Fig. 6.11. The same is done for the classical analysis with points A' and B' and its propagation illustrated in Fig. 6.12. Comparing the results with and without pressure load in both media, it can be seen that the crack propagates in a similar manner in the two analysis.

Considering initially the classical model, point A' indicates the step for which localization is detected and B' the step where the crack propagates through Material 1. As observed in Fig. 6.12, discontinuity is only introduced in the first two elements in front of the initial crack tip justifying the closeness of the two points in the equilibrium path. Establishing a reason for this behavior would require more studies and it is not the focus of this work. For the micromorphic medium, on the other hand, the crack initially tends do propagate vertically through the softer material (points A and B) and, as it reaches the second harder material propagates diagonally to the left of the model after some deformation (points C to D).

(i) No pressure load (micromorphic continuum)

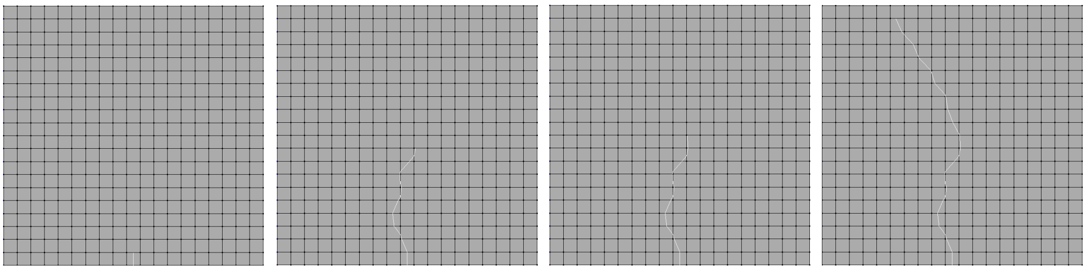

(a) A (b) B (c) C (d) D

(ii) Pressure load (micromorphic continuum)

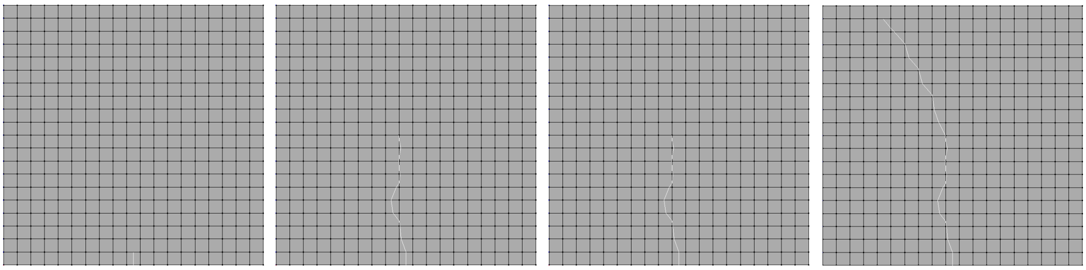

(e) A (f) B (g) C (h) D

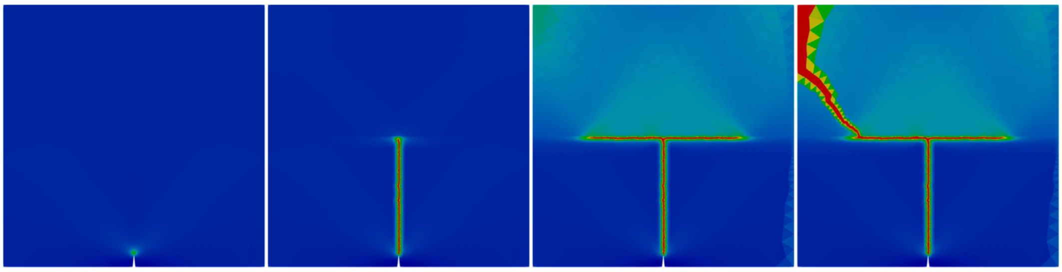

A B C D

(i) Pressure load (Phase-field (Ferreira et al., 2024))

Figure 6.11: Notched bi-material tensile test: crack propagation

At the initial stage of the micromorphic continuum analyses, two nodes are enriched due to the presence of the initial crack. By the final step of the nonlinear analysis, 60 nodes are enriched in the model without pressure, while 59 nodes are enriched in the model with pressure. As each node in a plane micromorphic model possesses six degrees of freedom, and all degrees of freedom are enriched, this results in the addition of 360 and 354 degrees of freedom in the analyses, respectively.

It is worth mentioning that this benchmark problem is designed to demonstrate the capability of the phase-field model in capturing the crack branching phenomenon, as explored by Molnár and Gravouil (2017) and Ferreira et al. (2024). Initially, the fracture propagates vertically until it reaches the harder material. At this point, branching occurs,

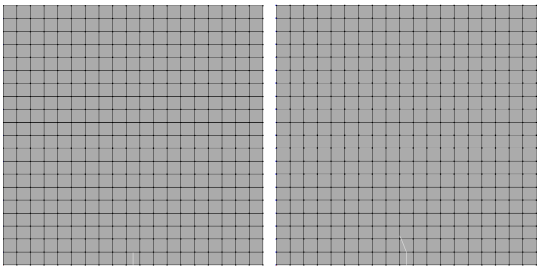

(i) No pressure load

(a) A’ (b) B’

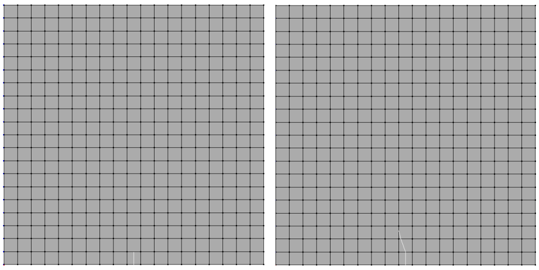

(ii) Pressure load

(c) A’ (d) B’

Figure 6.12: Notched bi-material tensile test: crack propagation for classical continuum

as it requires less energy than continuing propagation into Material 2, causing the crack to extend horizontally along the interface between the two materials. After a larger deformation, the stronger material eventually fractures as well. The results presented in Ferreira et al. (2024) considering pressure load for the crack propagation and the equilibrium path are illustrated in Figs. 6.11(i) and 6.13, respectively. For the phase-field results in Figs. 6.11(i), the phase-field variable is plotted varying from 0 (blue; undamaged material) to 1 (red; completely damaged material).

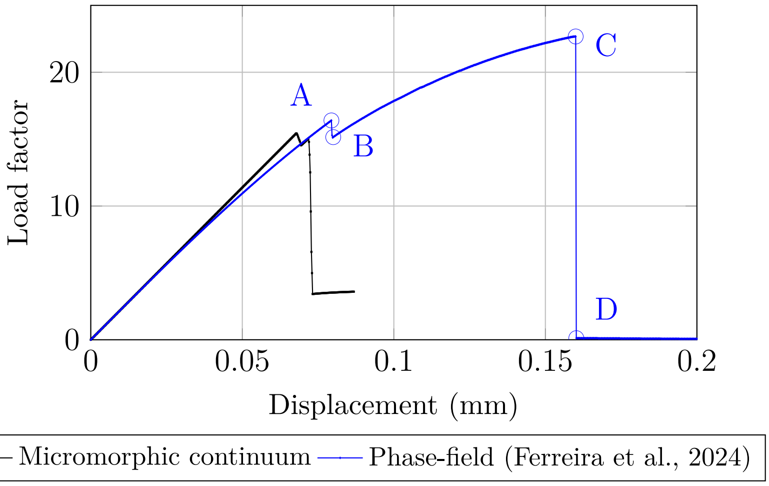

Figure 6.13: Notched bi-material tensile test: load factor versus horizontal displacement - comparison of phase-field and micromorphic models with pressure load

The proposed XFEM micromorphic approach does not capture the branching phenomenon, likely due to its brittle behavior, as traction effects are not considered along the crack surface. Nevertheless, despite the use of a coarse mesh and a brittle fracture assumption, the model effectively captures the overall expected fracture behavior and it is able to describe the propagation through the softer material satisfactorily as can be observed comparing the results for load factor versus displacement for phase-field and micromorphic models presented in Fig. 6.13. Again, as mentioned in the example in Section 6.3.2, the proposed model is not able to fully represent the fracture trajectory when crack propagates in a more complex geometry.

The results presented for the proposed approach in comparison to the phase-field model lead to the conclusion that associating the micromorphic continuum theory to the diffuse fracture representation of phase-field has the potential to provide better results than the node enrichment proposed by the XFEM model based on the Heaviside function.

Chapter 7

Conclusions

7.1 Contributions to knowledge

This work has explored the development of a continuous-discontinuous model for damage and fracture in micromorphic media, with a particular focus on its application to pressurized fractures. The study was motivated by the need for modeling approaches capable of accurately capturing multiscale fracture mechanics. Generalized continua, in contrast to classical theories, provide a framework for incorporating microstructural behavior into macroscopic analysis.

A key aspect of this study was the definition of a reliable criterion for discontinuity initiation in the micromorphic continuum, allowing the transition from continuous damage, represented by elastic-degrading damage models, to a discontinuous phase. The micromorphic continuum, due to its non-local formulation, presents regularization properties when strain localization is present. The formulation of a macroscale acoustic tensor considering only measures related to the macroscale led to a localization criterion based on the singularity of the acoustic tensor that does indicate strain localization. This results further attest the regularization capacity of the micromorphic theory based on the properties of the micromorphic acoustic tensor, approach not yet discussed in the literature.

The necessity of defining an acoustic tensor based on microscale parameters became evident as no prior studies had established a localization criterion for micromorphic media. To address this gap, a microscale micromorphic acoustic tensor was introduced and validated through numerical results, demonstrating its ability to correctly identify strain localization and determine the discontinuity direction in generalized continua. This advancement paves the way for new continuous-discontinuous approaches to damage and fracture in generalized media, as well as a deeper understanding of strain localization and regularization mechanisms.

Subsequently, the discontinuous phase was modeled through a application of the principles of the extended finite element method (XFEM) to micromorphic media. In this novel approach, all additional degrees of freedom of the continuum were enriched in the crack description, allowing the representation of the discontinuity in the classical degrees of freedom as in the additional degrees of freedom of the generalized theory.

The proposed model demonstrated advantages in addressing problems where strain localization induces instabilities and mesh-dependent results in classical continuum analyses. By allowing particles on either side of the crack to undergo distinct deformations, the generalized representation of discontinuities creates new possibilities for studying failure in complex media. In such cases, the additional degrees of freedom in micromorphic media can effectively capture the microstructural response of materials.

Lastly, the proposed framework was further extended to model pressurized fractures under the assumption of constant load pressure on the crack surface. The approach, through the numerical simulations presented, proved to capture the overall expected response of pressurized fractures leading to new approaches in the field of hydraulic fracturing based on generalized continua, a field yet to be fully explored.

Given the inherently multiscale nature of micromorphic continua, this methodology provides a foundation for future studies on hydraulic fracturing in heterogeneous and complex media across different scales.

In conclusion, this work provides a step forward in the development of more accurate and efficient models of structural failure. The insights gained from this study contribute to both the theoretical understanding of generalized continua and their application in computational mechanics, highlighting the potential of micromorphic-based models in addressing complex phenomena.

7.2 Future research topics

Considering the limited time available for the development of this thesis and the broad scope of the topics investigated, some aspects remain unexplored and are presented here as suggestions for future research. Given the limited studies in the field of generalized continua and, specially, micromorphic theory, the author hopes that this topic will be further explored in future research, leading to a deeper understanding and broader application in engineering.

1. Refinement of the continuous-discontinuous transition criteria:

   Given the novelty of the proposed localization criterion and the various existing methods for continuous-discontinuous transition in classical media, the criterion could be enhanced by incorporating the influence of surrounding material properties and boundary conditions. Some degree of mesh dependency was observed in the proposed numerical approach, as the crack propagation process was primarily controlled by the first material point where localization was detected. Addressing this issue would improve the robustness and accuracy of the model.

2. Formulation of new constitutive models for micromorphic continua:

   The proposed scalar-isotropic damage models do not distinguish between tensile and compressive damage, which may lead to inaccuracies in problems where compressive stresses are significant compared to tensile stresses. Since few constitutive models have been specifically formulated for micromorphic theory, developing new models specific to this framework would expand its applicability and enable the modeling of a wider range of problems.

3. Enhancement of the micromorphic-XFEM approach:

   The current model assumes a traction-free crack, which simplifies the physical phenomenon but may not fully capture the mechanical behavior of real fractures. Considering cohesive forces between crack surfaces could improve the accuracy of the model. Additionally, refining the enrichment functions for the crack tip could lead to a more accurate representation of fracture behavior.

4. Integration of micromorphic theory with Phase-Field models:

   Combining the micromorphic framework with phase-field models could enhance crack representation in cases involving complex geometries, such as branching cracks and interactions with natural fractures. This hybrid approach may improve the accuracy of micromorphic-based fracture modeling.

5. Expansion of the micromorphic framework within the INSANE system:

   Extending the implementation of the micromorphic model within the INSANE computational framework by incorporating boundary element methods and meshless techniques could broaden its applicability. This would also facilitate comparisons between different numerical approaches, leading to more robust and computationally efficient models.

6. Application of the proposed model to three-dimensional fracture problems:

   This study focused on two-dimensional problems, but the micromorphic model could be extended to three-dimensional fracture simulations. Such an extension would provide a more realistic representation of hydraulic fracturing, allowing for the analysis of complex geometries and fracture networks.

7. Simulation of hydraulic fracturing in porous media:

   The current model assumes low-permeability media and low-viscosity fluids, which simplifies the analysis but also limits its applicability. Extending the micromorphic-XFEM model to include fluid-solid interactions and permeability effects would enable a more comprehensive study of hydraulic fracturing in porous media.

8. Optimization of computational performance for large-scale simulations:

   The micromorphic theory introduces additional degrees of freedom, which can significantly increase computational costs. Expanding the proposed model to accommodate more realistic conditions, as suggested in the topics above, could lead to performance bottlenecks. Implementing parallel computing techniques and optimization strategies would enhance computational efficiency and enable large-scale simulations.

Bibliography

Adachi, J. I. and Detournay, E. (2008), ‘Plane strain propagation of a hydraulic fracture in a permeable rock’, *Engineering Fracture Mechanics* vol. 75(16), 4666–4694.

Adachi, J., Siebrits, E., Peirce, A. and Desroches, J. (2007), ‘Computer simulation of hydraulic fractures’, *International Journal of Rock Mechanics and Mining Sciences* vol. 44(5), 739–757.

Alves, P. D., Barros, F. B. and Pitangueira, R. L. S. (2013), ‘An object-oriented approach to the Generalized Finite Element Method’, *Advances in Engineering Software* vol. 59, 1–18.

Ambati, M., Gerasimov, T. and Lorenzis, L. D. (2015), ‘A review on phase-field models of brittle fracture and a new fast hybrid formulation’, *Computational Mechanics* vol. 55, 383–405.

Armero, F. and Oller, S. (2000*a*), ‘A general framework for continuum damage models. I. infinitesimal plastic damage models in stress space’, *International Journal of Solids and Structures* vol. 37(48-50), 7409–7436.

Armero, F. and Oller, S. (2000*b*), ‘A general framework for continuum damage models. II. integration algorithms, with applications to numerical simulation of porous metals’, *International Journal of Solids and Structures* vol. 37(48-50), 7437–7464.

Bao, J., Fathi, E. and Ameri, S. (2015), ‘Uniform investigation of hydraulic fracturing propagation regimes in the plane strain model’, *International Journal for Numerical and Analytical Methods in Geomechanics* vol. 39(5), 507–523.

Barenblatt, G. (1962), The mathematical theory of equilibrium cracks in brittle fracture, Vol. 7 of *Advances in Applied Mechanics*, Elsevier, pp. 55–129.

Bažant, Z. P. and Jirásek, M. (2002), ‘Nonlocal integral formulations of plasticity and damage: Survey of progress’, *Journal of Engineering Mechanics* vol. 128(11), 1119–1149.

Bažant, Z. P. and Lin, F. (1988), ‘Nonlocal smeared cracking model for concrete fracture’, *Journal of Structural Engineering* vol. 114(11), 2493–2510.

Bažant, Z. P. and Planas, J. (1998), *Fracture and Size Effect in Concrete and Other Quasibrittle Materials*, CRC Press LLC.

Belytschko, T., Chen, H., Xu, J. and Zi, G. (2003), ‘Dynamic crack propagation based on loss of hyperbolicity and a new discontinuous enrichment’, *International Journal for Numerical Methods in Engineering* vol. 58(12), 1873–1905.

Belytschko, T., Gracie, R. and Ventura, G. (2009), ‘A review of extended/generalized finite element methods for material modeling’, *Modelling and Simulation in Materials Science and Engineering* vol. 17(4), 043001.

Belytschko, T., Krongauz, Y., Organ, D., Fleming, M. and Krysl, P. (1996), ‘Meshless methods: An overview and recent developments’, *Computer Methods in Applied Mechanics and Engineering* vol. 139(1), 3–47.

Biot, M. A. (1941), ‘General Theory of Three-Dimensional Consolidation’, *Journal of Applied Physics* vol. 12(2), 155–164.

Biswas, R. and Poh, L. (2017), ‘A micromorphic computational homogenization framework for heterogeneous materials’, *Journal of the Mechanics and Physics of Solids* vol. 102, 187–208.

Boone, T. J. and Ingraffea, A. R. (1990), ‘A numerical procedure for simulation of hydraulically-driven fracture propagation in poroelastic media’, *International Journal for Numerical and Analytical Methods in Geomechanics* vol. 14(1), 27–47.

Boone, T., Wawrzynek, P. and Ingraffea, A. (1986), ‘Simulation of the fracture process in rock with application to hydrofracturing’, *International Journal of Rock Mechanics and Mining Sciences and Geomechanics Abstracts* vol. 23(3), 255–265.

Bourdin, B., Chukwudozie, C. and Yoshioka, K. (2012), A Variational Approach to the Numerical Simulation of Hydraulic Fracturing, *in* ‘SPE Annual Technical Conference and Exhibition’, SPE, San Antonio, Texas, USA, pp. SPE–159154–MS.

Camborde, F., Mariotti, C. and Donzé, F. (2000), ‘Numerical study of rock and concrete behaviour by discrete element modelling’, *Computers and Geotechnics* vol. 27(4), 225–247.

Carol, I., Rizzi, E. and Willam, K. (1994), ‘A unified theory of elastic degradation and damage based on a loading surface’, *International Journal of Solids and Structures* vol. 31(20), 2835–2865.

Carol, I., Rizzi, E. and Willam, K. (2001*a*), ‘On the formulation of anisotropic elastic degradation. I. theory based on a pseudo-logarithmic damage tensor rate’, *International Journal of Solids and Structures* vol. 38(4), 491–518.

Carol, I., Rizzi, E. and Willam, K. (2001*b*), ‘On the formulation of anisotropic elastic degradation. II. generalized pseudo-rankine model for tensile damage’, *International Journal of Solids and Structures* vol. 38(4), 519–546.

Carrier, B. and Granet, S. (2012), ‘Numerical modeling of hydraulic fracture problem in permeable medium using cohesive zone model’, *Engineering Fracture Mechanics* vol. 79, 312–328.

Cendón, D., Gálvez, J., Elices, M. and Planas, J. (2000), ‘Modelling the fracture of concrete under mixed loading’, *International Journal of Fracture* vol. 103, 293–310.

Chen, B., Barboza, B. R., Sun, Y., Bai, J., Thomas, H. R., Dutko, M., Cottrell, M. and Li, C. (2022), ‘A review of hydraulic fracturing simulation’, *Archives of Computational Methods in Engineering* vol. 29, 1–58.

Cleary, M. P. (1980), Comprehensive design formulae for hydraulic fracturing, SPE Annual Technical Conference and Exhibition, Dallas, Texas.

Clifton, R. and Abou-Sayed, A. (1979), On the computation of the three-dimensional geometry of hydraulic fractures, SPE Rocky Mountain Petroleum Technology Conference / Low Permeability Reservoirs Symposium, Denver, Colorado.

Comi, C., Mariani, S. and Perego, U. (2007), ‘An extended fe strategy for transition from continuum damage to mode i cohesive crack propagation’, *International Journal for Numerical and Analytical Methods in Geomechanics* vol. 31(2), 213–238.

Cosserat, E. and Cosserat, F. (1909), *Théorie des corps déformables*, Librairie Scientifique A. Hermann et Fils, Paris.

Cruz, R. F. P. M. L. (2018), An XFEM Element to Model Intersections Between Hydraulic and Natural Fractures in Porous Rocks, PhD thesis, Pontifícia Universidade Católica do Rio de Janeiro, Rio de Janeiro, RJ, Brasil.

de Borst, R. (1987), ‘Smeared cracking, plasticity, creep, and thermal loading–a unified approach’, *Computer Methods in Applied Mechanics and Engineering* vol. 62, 89–110.

de Borst, R. (1991), ‘Simulation of strain localization: A reappraisal of the Cosserat continuum’, *Engineering Computations* vol. 8(4), 317–332.

de Borst, R. (2022), ‘Fracture and damage in quasi-brittle materials: A comparison of approaches’, *Theoretical and Applied Fracture Mechanics* vol. 122, 103652.

de Borst, R. and Mühlhaus, H.-B. (1992), ‘Gradient-dependent plasticity: Formulation and algorithmic aspects’, *International Journal for Numerical Methods in Engineering* vol. 35(3), 521–539.

de Borst, R., Sluys, L. J., Mühlhaus, H.-B. and Pamin, J. (1993), ‘Fundamental issues in finite element analyses of localization of deformation’, *Engineering Computations* vol. 10(2), 99–121.

Deb, P., Salimzadeh, S., Vogler, D., Düber, S., Clauser, C. and Settgast, R. R. (2021), ‘Verification of coupled hydraulic fracturing simulators using laboratory-scale experiments’, *Rock Mechanics and Rock Engineering* vol. 54, 2881–2902.

Dontsov, E. and Suarez-Rivera, R. (2020), ‘Propagation of multiple hydraulic fractures in different regimes’, *International Journal of Rock Mechanics and Mining Sciences* vol. 128, 104270.

Dugdale, D. (1960), ‘Yielding of steel sheets containing slits’, *Journal of the Mechanics and Physics of Solids* vol. 8(2), 100–104.

Dym, C. L. and Shames, I. H. (2013), *Solid Mechanics: A Variational Approach, Augmented Edition*, SpringerLink: Bücher, Springer New York.

Egger, A., Pillai, U., Agathos, K., Kakouris, E., Chatzi, E., Aschroft, I. A. and Triantafyllou, S. P. (2019), ‘Discrete and phase field methods for linear elastic fracture mechanics: A comparative study and state-of-the-art review’, *Applied Sciences* vol. 9(12).

Einsfeld, R. A. (1997), Simulação Numérica de Fraturamento em Estruturas de Concreto Combinando os Processos Discreto e Distribuído, PhD thesis, Pontifícia Universidade Católica do Rio de Janeiro, Rio de Janeiro, RJ, Brasil.

Eremeyev, V. A. (2005), ‘Acceleration Waves in Micropolar Elastic Media’, *Doklady Physics* vol. 50(4), 204–206.

Eremeyev, V. A., Lebedev, L. P. and Cloud, M. J. (2018), ‘Acceleration waves in the nonlinear micromorphic continuum’, *Mechanics Research Communications* vol. 93, 70–74.

Eringen, A. C. (1966), Mechanics of micromorphic materials, *in* H. Görtler, ed., ‘Applied Mechanics’, Springer Berlin Heidelberg, Berlin, Heidelberg, pp. 131–138.

Eringen, A. C. (1980), *Mechanics of Continua*, 2 edn, Robert E. Krieger Publishing Company, Huntington, New York.

Eringen, A. C. (1999), *Microcontinuum Field Theories: I. Foundations and solids*, Springer, New York.

Eringen, A. C. and Şuhubi, E. S. (1964), ‘Nonlinear theory of simple micro-elastic solids – i’, *International Journal of Engineering Science* vol. 2(2), 189–203.

Ferreira, E. M., Novelli, L., da Silva Pitangueira, R. L. and Gori, L. (2024), 'Smoothed point interpolation methods for phase-field modelling of pressurised fracture', *Engineering Analysis with Boundary Elements* vol. 167, 105869.

Fioresi, L. A. F., Pitangueira, R. L. S. and Penna, S. S. (2020), 'Numerical technique for strain localization analysis considering a Cartesian parameterization', *Journal of the Brazilian Society of Mechanical Sciences and Engineering* vol. 42(3), 145.

Forest, S. (1998), 'Mechanics of generalized continua: construction by homogenization', *Journal de Physique IV* vol. 8, Pr4–39, Pr4–48.

Forest, S. (2009), 'Micromorphic approach for gradient elasticity, viscoplasticity, and damage', *Journal of Engineering Mechanics* vol. 135(3), 117–131.

Forest, S., Ammar, K. and Appolaire, B. (2011), Micromorphic vs. phase-field approaches for gradient viscoplasticity and phase transformations, *in* B. Markert, ed., 'Advances in Extended and Multifield Theories for Continua', Springer Berlin Heidelberg, Berlin, Heidelberg, pp. 69–88.

Forest, S. and Sab, K. (1998), 'Cosserat overall modeling of heterogeneous materials', *Mechanics Research Communications* vol. 25(4), 449–454.

Forest, S. and Sievert, R. (2006), 'Nonlinear microstrain theories', *International Journal of Solids and Structures* vol. 43(24), 7224–7245. Size-dependent Mechanics of Materials.

Fries, T.-P. and Belytschko, T. (2010), 'The extended/generalized finite element method: An overview of the method and its applications', *International Journal for Numerical Methods in Engineering* vol. 84(3), 253–304.

Gálvez, J., Červenka, J., Cendón, D. and Saouma, V. (2002), 'A discrete crack approach to normal/shear cracking of concrete', *Cement and Concrete Research* vol. 32(10), 1567–1585.

García-Álvarez, V. O., Gettu, R. and Carol, I. (2012), 'Analysis of mixed-mode fracture in concrete using interface elements and a cohesive crack model', *Sadhana* vol. 37(1), 187–205.

Gdoutos, E. E. (2005), *Fracture Mechanics: An Introduction*, Springer Netherlands, Dordrecht.

Geertsma, J. and De Klerk, F. (1969), 'A Rapid Method of Predicting Width and Extent of Hydraulically Induced Fractures', *Journal of Petroleum Technology* vol. 21(12), 1571–1581.

Germain, P. (1973*a*), 'La méthode des puissances virtuelles en mécanique des millieux continus premiere partie: théorie du second gradient', *Journal de Mécanique* vol. 12(2), 235–274.

Germain, P. (1973*b*), 'The method of virtual power in continuum mechanics. part 2: Microstructure', *SIAM Journal of Applied Mathematics* vol. 25(3), 556–575.

Giorgio, I., Angelo, M. D., Turco, E. and Misra, A. (2020), 'A Biot–Cosserat two-dimensional elastic nonlinear model for a micromorphic medium', *Continuum Mechanics and Thermodynamics* vol. 32, 1357–1369.

Giovanardi, B., Scotti, A. and Formaggia, L. (2017), 'A hybrid XFEM –Phase field (*Xfield*) method for crack propagation in brittle elastic materials', *Computer Methods in Applied Mechanics and Engineering* vol. 320, 396–420.

Gori, L., Penna, S. S. and da Silva Pitangueira, R. L. (2018), 'Discontinuous failure in micropolar elastic-degrading models', *International Journal of Damage Mechanics* vol. 27(10), 1482–1515.

Gori, L., Penna, S. S. and Pitangueira, R. L. (2017*a*), 'A computational framework for constitutive modelling', *Computers and Structures* vol. 187, 1–23.

Gori, L., Penna, S. S. and Pitangueira, R. L. (2017*b*), 'An enhanced tensorial formulation for elastic degradation in micropolar continua', *Applied Mathematical Modelling* vol. 41, 299–315.

Griffith, A. A. (1921), 'VI. the phenomena of rupture and flow in solids', *Philosophical Transactions of the Royal Society of London. Series A, Containing Papers of a Mathematical or Physical Character* vol. 221(582-593), 163–198.

Gupta, P. and Duarte, C. A. (2014), 'Simulation of non-planar three-dimensional hydraulic fracture propagation', *International Journal for Numerical and Analytical Methods in Geomechanics* vol. 38(13), 1397–1430. _eprint: https://onlinelibrary.wiley.com/doi/pdf/10.1002/nag.2305.

Gupta, P. and Duarte, C. A. (2018), 'Coupled hydromechanical-fracture simulations of nonplanar three-dimensional hydraulic fracture propagation', *International Journal for Numerical and Analytical Methods in Geomechanics* vol. 42(1), 143–180. _eprint: https://onlinelibrary.wiley.com/doi/pdf/10.1002/nag.2719.

Hadamard, J. (1903), *Leçons sur la propagation des ondes et les équations de l'hydrodynamique*, Librairie Scientifique A. Hermann, Paris.

Hashin, Z. (1983), 'Analysis of Composite Materials—A Survey', *Journal of Applied Mechanics* vol. 50(3), 481–505.

Hill, R. (1958), ‘A general theory of uniqueness and stability in elastic-plastic solids’, *Journal of the Mechanics and Physics of Solids* vol. 6(3), 236–249.

Hill, R. (1963), ‘Elastic properties of reinforced solids: Some theoretical principles’, *Journal of the Mechanics and Physics of Solids* vol. 11(5), 357–372.

Hill, R. (1967), ‘The essential structure of constitutive laws for metal composites and polycrystals’, *Journal of the Mechanics and Physics of Solids* vol. 15(2), 79–95.

Hillerborg, A., Modéer, M. and Petersson, P.-E. (1976), ‘Analysis of crack formation and crack growth in concrete by means of fracture mechanics and finite elements’, *Cement and Concrete Research* vol. 6(6), 773–781.

Hirschberger, C. B. (2008), A Treatise on Micromorphic Continua. Theory, Homogenization, Computation, PhD thesis, Technische Universität Kaiserslautern, Kaiserslautern, Germany.

Hütter, G. (2017), ‘Homogenization of a Cauchy continuum towards a micromorphic continuum’, *Journal of the Mechanics and Physics of Solids* vol. 99, 394–408.

Hütter, G. (2023), ‘Interpretation of micromorphic constitutive relations for porous materials at the microscale via harmonic decomposition’, *Journal of the Mechanics and Physics of Solids* vol. 171, 105135.

Hütter, G., Mühlich, U. and Kuna, M. (2015), ‘Micromorphic homogenization of a porous medium: elastic behavior and quasi-brittle damage’, *Continuum Mechanics and Thermodynamics* vol. 27, 1059–1072.

ICOLD (1999), Theme A2: Imminent failure flood for a concrete gravity dam, *in* ‘Fifth International Benchmark Workshop on Numerical Analysis of Dams’, USCOLD, Denver, Colorado.

Irwin, G. R. (1957), ‘Analysis of Stresses and Strains Near the End of a Crack Traversing a Plate’, *Journal of Applied Mechanics* vol. 24(3), 361–364.

Jirásek, M. (2000), ‘Comparative study on finite elements with embedded discontinuities’, *Computer Methods in Applied Mechanics and Engineering* vol. 188(1), 307–330.

Jirásek, M. (2001), Modeling of localized damage and fracture in quasibrittle materials, *in* P. A. Vermeer, H. J. Herrmann, S. Luding, W. Ehlers, S. Diebels and E. Ramm, eds, ‘Continuous and Discontinuous Modelling of Cohesive-Frictional Materials’, Springer Berlin Heidelberg, Berlin, Heidelberg, pp. 17–29.

Jirásek, M. (2007), ‘Mathematical analysis of strain localization’, *Revue Européenne de Génie Civil* vol. 11(7-8), 977–991.

Jirásek, M. and Zimmermann, T. (2001*a*), 'Embedded crack model: I. basic formulation', *International Journal for Numerical Methods in Engineering* vol. 50(6), 1269–1290.

Jirásek, M. and Zimmermann, T. (2001*b*), 'Embedded crack model. Part II: combination with smeared cracks', *International Journal for Numerical Methods in Engineering* vol. 50(6), 1291–1305.

Ju, J. (1989), 'On energy-based coupled elastoplastic damage theories: Constitutive modeling and computational aspects', *Int. J. Solids Struct.* vol. 25(7), 803–833.

Kachanov, L. (1958), 'On time to rupture in creep conditions', *Izvestia Akademii Nauk SSSR, Otdelenie Tekhnicheskikh Nauk* (8), 26–31. in russian.

Khoei, A. R. and Karimi, K. (2008), 'An enriched-FEM model for simulation of localization phenomenon in Cosserat continuum theory', *Computational Materials Science* vol. 44(2), 733–749.

Khristianovic, S. and Zheltov, Y. (1955), Formation of vertical fractures by means of highly viscous liquid, Vol. 2 of *Proceedings of the Fourth World Petroleum Congress*, pp. 579–586.

Krajcinovic, D. (1996), *Damage Mechanics*, Vol. 41 of *North-Holland Series in Applied Mathematics and Mechanics*, Elsevier Science, Amsterdam, The Netherlands.

Krajcinovic, D. and Lemaitre, J., eds (1987), *Continuum damage mechanics - Theory and applications*, number 295 *in* 'CISM courses and lectures - International centre for mechanical sciences', SPRINGER-VERLAG WIEN GMBH.

Kröner, E. (1977), 'Bounds for effective elastic moduli of disordered materials', *Journal of the Mechanics and Physics of Solids* vol. 25(2), 137–155.

Lakes, R. (1986), 'Experimental microelasticity of two porous solids', *International Journal of Solids and Structures* vol. 22(1), 55–63.

Lecampion, B. (2009), 'An extended finite element method for hydraulic fracture problems', *Communications in Numerical Methods in Engineering* vol. 25(2), 121–133. _eprint: https://onlinelibrary.wiley.com/doi/pdf/10.1002/cnm.1111.

Lee, S., Wheeler, M. F. and Wick, T. (2016), 'Pressure and fluid-driven fracture propagation in porous media using an adaptive finite element phase field model', *Computer Methods in Applied Mechanics and Engineering* vol. 305, 111–132.

Lemaitre, J. (1987), *Formulation and Identification of Damage Kinetic Constitutive Equations*, Springer-Verlag Wien, New York, pp. 37–90.

Lemaitre, J. and Desmorat, R. (2005), *Engineering Damage Mechanics: Ductile, Creep, Fatigue and Brittle Failures*, Springer.

Li, L. C., Tang, C. A., Li, G., Wang, S. Y., Liang, Z. Z. and Zhang, Y. B. (2012), 'Numerical simulation of 3d hydraulic fracturing based on an improved flow-stress-damage model and a parallel fem technique', *Rock Mechanics and Rock Engineering* vol. 45, 801–818.

Li, X., Hofmann, H., Yoshioka, K., Luo, Y. and Liang, Y. (2022), 'Phase-Field Modelling of Interactions Between Hydraulic Fractures and Natural Fractures', *Rock Mechanics and Rock Engineering* vol. 55(10), 6227–6247.

Li, X., Liang, Y., Luo, Y. and Ai, C. (2020), 'Predicting hydraulic fracture propagation based on maximum energy release rate theory with consideration of T-stress', *Fuel* vol. 269, 117337.

Lisjak, A., Kaifosh, P., He, L., Tatone, B., Mahabadi, O. and Grasselli, G. (2017), 'A 2d, fully-coupled, hydro-mechanical, fdem formulation for modelling fracturing processes in discontinuous, porous rock masses', *Computers and Geotechnics* vol. 81, 1–18.

Lotfi, H. R. and Shing, P. B. (1994), 'Interface model applied to fracture of masonry structures', *Journal of Structural Engineering* vol. 120(1), 63–80.

Lourenço, P. B. and Rots, J. G. (1997), 'Multisurface Interface Model for Analysis of Masonry Structures', *Journal of Engineering Mechanics* vol. 123(7), 660–668.

Mal, A. K. and Singh, S. J. (1991), *Deformation of elastic solids*, Prentice Hall, Inc., Englewood Cliffs, NJ, USA.

Manzoli, O., Oliver, X. and Cervera, M. (1998), *Localización de Deformaciones: Análisis y Simulación Numérica de discontinuidades en Mecánica de Sólidos*, monografía CIMNE n. 44 edn, CIMNE.

Marigo, J. (1985), 'Modelling of brittle and fatigue damage for elastic material by growth of microvoids', *Engineering Fracture Mechanics* vol. 21(4), 861 – 874.

Martha, L., Wawrzynek, P. and Ingraffea, A. (1993), 'Arbitrary crack representation using solid modeling', *Engineering with Computers* vol. 9, 63–82.

Massart, T. J., Peerlings, R. H. J. and Geers, M. G. D. (2007*a*), 'An enhanced multi-scale approach for masonry wall computations with localization of damage', *International Journal for Numerical Methods in Engineering* vol. 69(5), 1022–1059.

Massart, T., Peerlings, R. and Geers, M. (2007*b*), 'Structural damage analysis of masonry walls using computational homogenization', *International Journal of Damage Mechanics* vol. 16(2), 199–226.

Massing, F., Glane, S., Müller, W. H. and Eremeyev, V. A. (2023), 'Micromorphic theory as a model for blood in the microcirculation: correction and analysis', *Continuum Mechanics and Thermodynamics* .

Maugin, G. A. (2017), *What Is Classical Continuum Mechanics?*, Springer Nature Singapore Pte Ltd.

Mazars, J. and Lemaitre, J. (1985), *Application of Continuous Damage Mechanics to Strain and Fracture Behavior of Concrete*, Springer Netherlands, Dordrecht, pp. 507–520.

Miehe, C. and Mauthe, S. (2016), 'Phase field modeling of fracture in multi-physics problems. Part III. Crack driving forces in hydro-poro-elasticity and hydraulic fracturing of fluid-saturated porous media', *Computer Methods in Applied Mechanics and Engineering* vol. 304, 619–655.

Mindlin, R. (1965), 'Second gradient of strain and surface-tension in linear elasticity', *International Journal of Solids and Structures* vol. 1(4), 417 – 438.

Mindlin, R. D. (1964), 'Micro-structure in linear elasticity', *Archive for Rational Mechanics and Analysis* vol. 16, 51–78. Communicated by R. A. Toupin.

Mohammadnejad, T. and Khoei, A. R. (2013), 'An extended finite element method for hydraulic fracture propagation in deformable porous media with the cohesive crack model', *Finite Elements in Analysis and Design* vol. 73, 77–95.

Molnár, G. and Gravouil, A. (2017), '2D and 3D Abaqus implementation of a robust staggered phase-field solution for modeling brittle fracture', *Finite Elements in Analysis and Design* vol. 130, 27–38.

Mota, A., Chen, Q., Foulk III, J., Ostien, J. and Lai, Z. (2016), 'A Cartesian parametrization for the numerical analysis of material instability', *International Journal for Numerical Methods in Engineering* vol. 108(2), 156–180. _eprint: https://onlinelibrary.wiley.com/doi/pdf/10.1002/nme.5228.

Mukhtar, F. and El-Tohfa, A. (2023), 'A review on fracture propagation in concrete: Models, methods, and benchmark tests', *Engineering Fracture Mechanics* vol. 281, 109100.

Munjiza, A. (2004), *The Combined Finite-Discrete Element Method*, John Wiley and Sons Ltd.

Munjiza, A., Andrews, K. R. F. and White, J. K. (1999), 'Combined single and smeared crack model in combined finite-discrete element analysis', *International Journal for Numerical Methods in Engineering* vol. 44(1), 41–57.

Neilsen, M. K. and Schreyer, H. L. (1993), 'Bifurcations in elastic-plastic materials', *International Journal of Solids and Structures* vol. 30(4), 521–544.

Nemat-Nasser, S. and Hori, M. (1993), *Micromechanics: Overall Properties of Heterogeneous Materials*, Elsevier Science Publishers.

Ngo, D. and Scordelis, A. C. (1967), 'Finite element analysis of reinforced concrete beams', *ACI Journal Proceedings* vol. 64(3), 152–163.

Nguyen, V. P., Rabczuk, T., Bordas, S. and Duflot, M. (2008), 'Meshless methods: A review and computer implementation aspects', *Mathematics and Computers in Simulation* vol. 79(3), 763–813.

Nilson, A. H. (1968), 'Nonlinear analysis of reinforced concrete by the finite element method', *ACI Journal Proceedings* vol. 65(9), 757–766.

Nordgren, R. (1972), 'Propagation of a Vertical Hydraulic Fracture', *Society of Petroleum Engineers Journal* vol. 12(04), 306–314.

Oden, J. T., Duarte, C. A. M. and Zienkiewicz, O. C. (1998), 'A new cloud-based *hp* finite element method', *Computer Methods in Applied Mechanics and Engineering* vol. 153(1), 117–126.

Oliver, J., Huespe, A., Pulido, M. and Chaves, E. (2002), 'From continuum mechanics to fracture mechanics: the strong discontinuity approach', *Engineering Fracture Mechanics* vol. 69(2), 113–136.

Ooi, E. and Yang, Z. (2010), 'A hybrid finite element-scaled boundary finite element method for crack propagation modelling', *Computer Methods in Applied Mechanics and Engineering* vol. 199(17), 1178–1192.

Ottosen, N. S. and Runesson, K. (1991), 'Properties of discontinuous bifurcation solutions in elasto-plasticity', *International Journal of Solids and Structures* vol. 27(4), 401–421.

Patil, R. U., Mishra, B. K. and Singh, I. V. (2018), 'A local moving extended phase field method (LMXPFM) for failure analysis of brittle materials', *Computer Methods in Applied Mechanics and Engineering* vol. 342, 674–709.

Perkins, T. and Kern, L. (1961), 'Widths of Hydraulic Fractures', *Journal of Petroleum Technology* vol. 13(09), 937–949.

Petracca, M., Pelà, L., Rossi, R., Zaghi, S., Camata, G. and Spacone, E. (2017), 'Micro-scale continuous and discrete numerical models for nonlinear analysis of masonry shear walls', *Construction and Building Materials* vol. 149, 296–314.

Pietruszczak, S. and Mróz, Z. (1981), 'Finite element analysis of deformation of strain-softening materials', *International Journal for Numerical Methods in Engineering* vol. 17(3), 327–334.

Rashid, Y. (1968), 'Ultimate strength analysis of prestressed concrete pressure vessels', *Nuclear Engineering and Design* vol. 7(4), 334–344.

Reges, P. D. N. (2021), Damage models for the micromorphic continuum, Master's thesis, Federal University of Minas Gerais, Belo Horizonte, Brazil. In Portuguese.

Reges, P. D., Pitangueira, R. L. and Silva, L. L. (2023), 'Elastic degradation models for the micromorphic continuum', *International Journal of Non-Linear Mechanics* p. 104450.

Reges, P. D., Pitangueira, R. L. and Silva, L. L. (2024), 'Modeling of micromorphic continuum based on a heterogeneous microscale', *International Journal of Non-Linear Mechanics* vol. 167, 104881.

Ren, Q., Dong, Y. and Yu, T. (2009), 'Numerical modeling of concrete hydraulic fracturing with extended finite element method', *Science in China Series E: Technological Sciences* vol. 52(3), 559–565.

Rice, J. R. (1968*a*), 'A Path Independent Integral and the Approximate Analysis of Strain Concentration by Notches and Cracks', *Journal of Applied Mechanics* vol. 35(2), 379–386.

Rice, J. R. (1968*b*), Mathematical analysis in the mechanics of fracture, *in* H. Liebowitz, ed., 'Fracture - An Advanced Treatise', Academic Press, New York, pp. 191–308.

Rizzi, E., Carol, I. and Willam, K. (1995), 'Localization Analysis of Elastic Degradation with Application to Scalar Damage', *Journal of Engineering Mechanics* vol. 121(4), 541–554. Publisher: American Society of Civil Engineers.

Rizzi, E., Maier, G. and Willam, K. (1996), 'On failure indicators in multidissipative materials', *International Journal of Solids and Structures* vol. 33(20), 3187–3214.

Roth, S.-N., Léger, P. and Soulaïmani, A. (2020), 'Strongly coupled XFEM formulation for non-planar three-dimensional simulation of hydraulic fracturing with emphasis on concrete dams', *Computer Methods in Applied Mechanics and Engineering* vol. 363, 112899.

Rudnicki, J. W. and Rice, J. R. (1975), ‘Conditions for the localization of deformation in pressure-sensitive dilatant materials’, *Journal of the Mechanics and Physics of Solids* vol. 23(6), 371–394.

Rueda, J., Mejia, C., Quevedo, R. and Roehl, D. (2020), ‘Impacts of natural fractures on hydraulic fracturing treatment in all asymptotic propagation regimes’, *Computer Methods in Applied Mechanics and Engineering* vol. 371, 113296.

Saleh, A. and Aliabadi, M. (1995), ‘Crack growth analysis in concrete using boundary element method’, *Engineering Fracture Mechanics* vol. 51(4), 533–545.

Saloustros, S., Cervera, M. and Pelà, L. (2019), ‘Challenges, tools and applications of tracking algorithms in the numerical modelling of cracks in concrete and masonry structures’, *International Scholarly Research Notices* (26), 961–1005.

Secchi, S. and Schrefler, B. A. (2012), ‘A method for 3-d hydraulic fracturing simulation’, *International Journal of Fracture* (178), 245–258.

Shephard, M. S., Yehia, N. A., Burd, G. S. and Weidner, T. J. (1985), ‘Automatic crack propagation tracking’, *Computers and Structures* vol. 20(1), 211–223. Special Issue: Advances and Trends in Structures and Dynamics.

Silva, L. L. (2019), Estratégia Multiescala para Descrição Micromórfica do Contínuo a partir do Contínuo Clássico, PhD thesis, Universidade Federal de Minas Gerais, Belo Horizonte, MG, Brasil.

Silva, L. L. d., Pitangueira, R. L. d. S., Penna, S. S. and Barros, F. B. (2016), ‘Um modelo numérico para simulação do processo de fissuração em meios parcialmente frágeis’, *Ciência & Engenharia* vol. 25(2), 67–77. Number: 2.

Silva, L. L., Pitangueira, R. L. d. S. and Penna, S. S. (2022), ‘Multiscale numerical strategy for micromorphic description of quasi-brittle media from classical elastic damage models at the microscale’, *Applied Mathematical Modelling* vol. 109, 52–76.

Simo, J. and Ju, J. (1987), ‘Strain- and stress-based continuum damage models–i. formulation’, *International Journal of Solids and Structures* vol. 23(7), 821 – 840.

Simone, A., Wells, G. N. and Sluys, L. J. (2003), ‘From continuous to discontinuous failure in a gradient-enhanced continuum damage model’, *Computer Methods in Applied Mechanics and Engineering* vol. 192(41), 4581–4607.

Sneddon, I. N. (1946), ‘The distribution of stress in the neighbourhood of a crack in an elastic solid’, *Proceedings of the Royal Society of London. Series A, Mathematical and Physical Sciences* vol. 187(1009), 229–260.

Sneddon, I. N. and Lowengrub, M. (1969), *Crack problems in the classical theory of elasticity*, The SIAM series in applied mathematics, John Wiley & Sons.

Souza, P. L. F. B. d., Penna, S. S., Pitangueira, R. L. d. S. and Peixoto, R. G. (2017), 'Análise do efeito de tamanho em estruturas de concreto via modelos de dano não-local', *Revista Sul-americana de Engenharia Estrutural* vol. 14(1). Number: 1.

Steinmann, P. and Willam, K. (1991), *Localization within the Framework of Micropolar Elasto-Plasticity*, Springer Berlin Heidelberg, Berlin, Heidelberg, pp. 296–313.

Strouboulis, T., Babuška, I. and Copps, K. (2000), 'The design and analysis of the Generalized Finite Element Method', *Computer Methods in Applied Mechanics and Engineering* vol. 181(1), 43–69.

Suhubi, E. S. and Eringen, A. C. (1964), 'Nonlinear theory of simple micro-elastic solids – II', *International Journal of Engineering Science* vol. 2(4), 389–404.

Truesdell, C. and Noll, W. (2004), The Non-Linear Field Theories of Mechanics, *in* C. Truesdell, W. Noll and S. S. Antman, eds, 'The Non-Linear Field Theories of Mechanics', Springer, Berlin, Heidelberg, pp. 1–579.

van den Eijnden, A., Bésuelle, P., Chambon, R. and Collin, F. (2016), 'A FE2 modelling approach to hydromechanical coupling in cracking-induced localization problems', *International Journal of Solids and Structures* vol. 97-98, 475–488.

van den Eijnden, A. P., Bésuelle, P., Collin, F. and Chambon, R. (2017), Microstructural effects on strain localization in a multiscale model for hydro-mechanical coupling, *in* E. Papamichos, P. Papanastasiou, E. Pasternak and A. Dyskin, eds, 'Bifurcation and Degradation of Geomaterials with Engineering Applications', Springer International Publishing, Cham, pp. 219–224.

Van Mier, J. (1995), 'Fracture mechanics of concrete: Will applications start to emerge?', *HERON* vol. 40(2), 147–162.

Vardoulakis, I. and Aifantis, E. C. (1991), 'A gradient flow theory of plasticity for granular materials', *Acta Mechanica* (87), 197–217.

Voigt, W. (1887), 'Theoretische studien über die elasticitätsverhältnisse der krystalle', *Abhandlungen der Königlichen Gesellschaft der Wissenschaften* vol. 34, 3–52.

Wan, K. and Li, X. (2015), 'Multiscale hydro-mechanical analysis of unsaturated granular materials using bridging scale method', *Engineering Computations* vol. 32, 935–955.

Wangen, M. (2013), 'Finite element modeling of hydraulic fracturing in 3d', *Computational Geosciences* vol. 17, 647–659.

Wells, G. N. and Sluys, L. J. (2001), ‘A new method for modelling cohesive cracks using finite elements’, *International Journal for Numerical Methods in Engineering* vol. 50(12), 2667–2682. _eprint: https://onlinelibrary.wiley.com/doi/pdf/10.1002/nme.143.

Willis, J. (1981), Variational and related methods for the overall properties of composites, Vol. 21 of *Advances in Applied Mechanics*, Elsevier, pp. 1–78.

Winkler, B., Hofstetter, G. and Lehar, H. (2004), ‘Application of a constitutive model for concrete to the analysis of a precast segmental tunnel lining’, *International Journal for Numerical and Analytical Methods in Geomechanics* vol. 28(7-8), 797–819.

Wong, H. S., Zobel, M., Buenfeld, N. R. and Zimmerman, R. W. (2009), ‘Influence of the interfacial transition zone and microcracking on the diffusivity, permeability and sorptivity of cement-based materials after drying’, *Magazine of Concrete Research* vol. 61(8), 571–589.

Yang, H., Abali, B. E., Müller, W. H., Barboura, S. and Li, J. (2022), ‘Verification of asymptotic homogenization method developed for periodic architected materials in strain gradient continuum’, *International Journal of Solids and Structures* vol. 238, 111386.

Yang, Y.-B. and Shieh, M.-S. (1990), ‘Solution method for nonlinear problems with multiple critical points’, *AIAA Journal* vol. 28(12), 2110–2116.

Zhi, J., Poh, L. H., Tay, T.-E. and Tan, V. B. C. (2022), ‘Direct fe2 modeling of heterogeneous materials with a micromorphic computational homogenization framework’, *Computer Methods in Applied Mechanics and Engineering* vol. 393, 114837.

Appendix

Appendix A

FEM approach quantities

Here are presented the terms introduced in Section 5 in vector and matrix form for the enriched-FEM approach.

$$\boldsymbol{u} = \begin{bmatrix} u_1 & u_2 & u_3 \end{bmatrix}^T \tag{A.1}$$

$$\boldsymbol{d_u} = \begin{bmatrix} d_{u_1} & d_{u_2} & d_{u_3} \end{bmatrix}^T \tag{A.2}$$

$$\boldsymbol{d'_u} = \begin{bmatrix} d'_{u_1} & d'_{u_2} & d'_{u_3} \end{bmatrix}^T \tag{A.3}$$

$$\boldsymbol{\phi} = \begin{bmatrix} \phi_{11} & \phi_{22} & \phi_{33} & \phi_{23} & \phi_{32} & \phi_{31} & \phi_{13} & \phi_{12} & \phi_{21} \end{bmatrix}^T \tag{A.4}$$

$$\boldsymbol{d_\phi} = \begin{bmatrix} d\phi_{11} & d\phi_{22} & d\phi_{33} & d\phi_{23} & d\phi_{32} & d\phi_{31} & d\phi_{13} & d\phi_{12} & d\phi_{21} \end{bmatrix}^T \tag{A.5}$$

$$\boldsymbol{d'_\phi} = \begin{bmatrix} d'\phi_{11} & d'\phi_{22} & d'\phi_{33} & d'\phi_{23} & d'\phi_{32} & d'\phi_{31} & d'\phi_{13} & d'\phi_{12} & d'\phi_{21} \end{bmatrix}^T \tag{A.6}$$

$$\boldsymbol{\epsilon} = [\epsilon_{11} \quad \epsilon_{22} \quad \epsilon_{33} \quad \epsilon_{23} \quad \epsilon_{32} \quad \epsilon_{31} \quad \epsilon_{13} \quad \epsilon_{12} \quad \epsilon_{21}]^T \tag{A.7}$$

$$\boldsymbol{e} = [e_{11} \quad e_{22} \quad e_{33} \quad e_{23} \quad e_{32} \quad e_{31} \quad e_{13} \quad e_{12} \quad e_{21}]^T \tag{A.8}$$

$$\boldsymbol{\gamma} = \begin{Bmatrix} \boldsymbol{\gamma}_1 \\ \boldsymbol{\gamma}_2 \\ \boldsymbol{\gamma}_3 \\ \boldsymbol{\gamma}_4 \end{Bmatrix}_{(27\times1)} \qquad \begin{aligned} \boldsymbol{\gamma}_1 &= \begin{bmatrix} \gamma_{111} & \gamma_{221} & \gamma_{122} & \gamma_{212} & \gamma_{331} & \gamma_{133} & \gamma_{313} \end{bmatrix}^T \\ \boldsymbol{\gamma}_2 &= \begin{bmatrix} \gamma_{222} & \gamma_{112} & \gamma_{211} & \gamma_{121} & \gamma_{332} & \gamma_{233} & \gamma_{323} \end{bmatrix}^T \\ \boldsymbol{\gamma}_3 &= \begin{bmatrix} \gamma_{333} & \gamma_{113} & \gamma_{311} & \gamma_{131} & \gamma_{223} & \gamma_{322} & \gamma_{232} \end{bmatrix}^T \\ \boldsymbol{\gamma}_4 &= \begin{bmatrix} \gamma_{231} & \gamma_{321} & \gamma_{312} & \gamma_{132} & \gamma_{123} & \gamma_{213} \end{bmatrix}^T \end{aligned} \tag{A.9}$$

$$\boldsymbol{M} = \begin{bmatrix} 1 & 0 & 0 & 0 & 0 & 0 & 0 & 0 & 0 \\ 0 & 1 & 0 & 0 & 0 & 0 & 0 & 0 & 0 \\ 0 & 0 & 1 & 0 & 0 & 0 & 0 & 0 & 0 \\ 0 & 0 & 0 & 0 & 1 & 0 & 0 & 0 & 0 \\ 0 & 0 & 0 & 1 & 0 & 0 & 0 & 0 & 0 \\ 0 & 0 & 0 & 0 & 0 & 0 & 1 & 0 & 0 \\ 0 & 0 & 0 & 0 & 0 & 1 & 0 & 0 & 0 \\ 0 & 0 & 0 & 0 & 0 & 0 & 0 & 0 & 1 \\ 0 & 0 & 0 & 0 & 0 & 0 & 0 & 1 & 0 \end{bmatrix} \tag{A.10}$$

$$\boldsymbol{L_u} = \begin{bmatrix} \partial_1 & 0 & 0 \\ 0 & \partial_2 & 0 \\ 0 & 0 & \partial_3 \\ 0 & \partial_3 & 0 \\ 0 & 0 & \partial_2 \\ 0 & 0 & \partial_1 \\ \partial_3 & 0 & 0 \\ \partial_2 & 0 & 0 \\ 0 & \partial_1 & 0 \end{bmatrix} \tag{A.11}$$

$$\boldsymbol{L_\phi} = \begin{bmatrix} \boldsymbol{L}_{\phi;1} \\ \boldsymbol{L}_{\phi;2} \\ \boldsymbol{L}_{\phi;3} \\ \boldsymbol{L}_{\phi;4} \end{bmatrix} \tag{A.12}$$

where

$$\boldsymbol{L}_{\phi;1} = \begin{bmatrix} \partial_1 & 0 & 0 & 0 & 0 & 0 & 0 & 0 & 0 \\ 0 & \partial_1 & 0 & 0 & 0 & 0 & 0 & 0 & 0 \\ 0 & 0 & 0 & 0 & 0 & 0 & 0 & \partial_2 & 0 \\ 0 & 0 & 0 & 0 & 0 & 0 & 0 & 0 & \partial_2 \\ 0 & 0 & \partial_1 & 0 & 0 & 0 & 0 & 0 & 0 \\ 0 & 0 & 0 & 0 & 0 & 0 & \partial_3 & 0 & 0 \\ 0 & 0 & 0 & 0 & 0 & \partial_3 & 0 & 0 & 0 \end{bmatrix} \tag{A.13}$$

$$\boldsymbol{L}_{\phi;2} = \begin{bmatrix} 0 & \partial_2 & 0 & 0 & 0 & 0 & 0 & 0 & 0 \\ \partial_2 & 0 & 0 & 0 & 0 & 0 & 0 & 0 & 0 \\ 0 & 0 & 0 & 0 & 0 & 0 & 0 & 0 & \partial_1 \\ 0 & 0 & 0 & 0 & 0 & 0 & 0 & \partial_1 & 0 \\ 0 & 0 & \partial_2 & 0 & 0 & 0 & 0 & 0 & 0 \\ 0 & 0 & 0 & \partial_3 & 0 & 0 & 0 & 0 & 0 \\ 0 & 0 & 0 & 0 & \partial_3 & 0 & 0 & 0 & 0 \end{bmatrix} \tag{A.14}$$

$$\boldsymbol{L}_{\phi;3} = \begin{bmatrix} 0 & 0 & \partial_3 & 0 & 0 & 0 & 0 & 0 & 0 \\ \partial_3 & 0 & 0 & 0 & 0 & 0 & 0 & 0 & 0 \\ 0 & 0 & 0 & 0 & 0 & \partial_1 & 0 & 0 & 0 \\ 0 & 0 & 0 & 0 & 0 & 0 & \partial_1 & 0 & 0 \\ 0 & \partial_3 & 0 & 0 & 0 & 0 & 0 & 0 & 0 \\ 0 & 0 & 0 & 0 & \partial_2 & 0 & 0 & 0 & 0 \\ 0 & 0 & 0 & \partial_2 & 0 & 0 & 0 & 0 & 0 \end{bmatrix} \tag{A.15}$$

$$\boldsymbol{L}_{\phi;4} = \begin{bmatrix} 0 & 0 & 0 & \partial_1 & 0 & 0 & 0 & 0 & 0 \\ 0 & 0 & 0 & 0 & \partial_1 & 0 & 0 & 0 & 0 \\ 0 & 0 & 0 & 0 & 0 & \partial_2 & 0 & 0 & 0 \\ 0 & 0 & 0 & 0 & 0 & 0 & \partial_2 & 0 & 0 \\ 0 & 0 & 0 & 0 & 0 & 0 & 0 & \partial_3 & 0 \\ 0 & 0 & 0 & 0 & 0 & 0 & 0 & 0 & \partial_3 \end{bmatrix} \tag{A.16}$$

$$\boldsymbol{t} = \begin{bmatrix} t_{11} & t_{22} & t_{33} & t_{23} & t_{32} & t_{31} & t_{13} & t_{12} & t_{21} \end{bmatrix}^T \tag{A.17}$$

$$\boldsymbol{s} = \begin{bmatrix} s_{11} & s_{22} & s_{33} & s_{23} & s_{32} & s_{31} & s_{13} & s_{12} & s_{21} \end{bmatrix}^T \tag{A.18}$$

$$\boldsymbol{m} = \left\{ \begin{array}{c} \boldsymbol{m}_1 \\ \boldsymbol{m}_2 \\ \boldsymbol{m}_3 \\ \boldsymbol{m}_4 \end{array} \right\}_{(27\times1)} \qquad \begin{array}{lcl} \boldsymbol{m}_1 & = & [m_{111} \quad m_{122} \quad m_{212} \quad m_{221} \quad m_{133} \quad m_{313} \quad m_{331}]^T \\ \boldsymbol{m}_2 & = & [m_{222} \quad m_{211} \quad m_{121} \quad m_{112} \quad m_{233} \quad m_{323} \quad m_{332}]^T \\ \boldsymbol{m}_3 & = & [m_{333} \quad m_{311} \quad m_{131} \quad m_{113} \quad m_{322} \quad m_{232} \quad m_{223}]^T \\ \boldsymbol{m}_4 & = & [m_{123} \quad m_{132} \quad m_{231} \quad m_{213} \quad m_{312} \quad m_{321}]^T \end{array} \tag{A.19}$$

$$\rho\boldsymbol{f} = [\rho f_1 \quad \rho f_2 \quad \rho f_3]^T \tag{A.20}$$

$$\hat{\boldsymbol{t}}_{(\boldsymbol{n})} = \left[\hat{t}_{(\boldsymbol{n})1} \quad \hat{t}_{(\boldsymbol{n})2} \quad \hat{t}_{(\boldsymbol{n})3}\right]^T \tag{A.21}$$

$$\rho\boldsymbol{l} = [\rho l_{11} \quad \rho l_{22} \quad \rho l_{33} \quad \rho l_{23} \quad \rho l_{32} \quad \rho l_{31} \quad \rho l_{13} \quad \rho l_{12} \quad \rho l_{21}]^T \tag{A.22}$$

$$\hat{\boldsymbol{m}}_{(\boldsymbol{n})} = \left[\hat{m}_{(\boldsymbol{n})11}\ \hat{m}_{(\boldsymbol{n})22}\ \hat{m}_{(\boldsymbol{n})33}\ \hat{m}_{(\boldsymbol{n})23}\ \hat{m}_{(\boldsymbol{n})32}\ \hat{m}_{(\boldsymbol{n})31}\ \hat{m}_{(\boldsymbol{n})13}\ \hat{m}_{(\boldsymbol{n})12}\ \hat{m}_{(\boldsymbol{n})21}\right]^T \tag{A.23}$$